

1 Contents

| | | |
|-----------|--|-----------|
| 2 | 1 A search for highly ionising, short tracks at the CMS detector | 1 |
| 3 | 1.1 Motivation | 3 |
| 4 | 1.2 General search strategy | 5 |
| 5 | 1.2.1 Comparison to earlier searches | 11 |
| 6 | 1.3 Improved dE/dx measurement for short tracks | 12 |
| 7 | 1.3.1 Estimation of the ionisation loss of charged particles | 13 |
| 8 | 1.3.2 Energy calibration of the silicon pixel tracker | 15 |
| 9 | 1.3.3 Discrimination of highly-ionising particles | 20 |
| 10 | 1.3.4 Discrimination improvements | 21 |
| 11 | 1.4 Simulated samples | 26 |
| 12 | 1.4.1 Standard Model background samples | 26 |
| 13 | 1.4.2 Signal samples | 27 |
| 14 | 1.5 Event selection | 29 |
| 15 | 1.5.1 Datasets and triggers | 29 |
| 16 | 1.5.2 Selection of signal candidate events | 30 |
| 17 | 1.5.2.1 Event-based selection | 31 |
| 18 | 1.5.2.2 Candidate track selection | 33 |
| 19 | 1.6 Characterisation and estimation of the Standard Model backgrounds | 43 |
| 20 | 1.6.1 Fake background | 44 |
| 21 | 1.6.1.1 Inclusive fake background estimation | 45 |
| 22 | 1.6.1.2 dE/dx shape of fake background | 50 |
| 23 | 1.6.2 Leptonic background | 52 |
| 24 | 1.6.2.1 Inclusive leptonic background estimation | 57 |
| 25 | 1.6.2.2 dE/dx shape of leptonic background | 58 |
| 26 | 1.6.3 Background estimation validation | 60 |
| 27 | 1.6.4 Systematic uncertainties | 63 |
| 28 | 1.6.4.1 Uncertainty on the fake rate | 63 |

| | | | |
|----|-------------|--|-----------|
| 29 | 1.6.4.2 | Uncertainty on the dE/dx shape of fake tracks | 64 |
| 30 | 1.6.4.3 | Uncertainty on the leptonic scale factor | 64 |
| 31 | 1.6.4.4 | Uncertainty on the leptonic dE/dx shape | 65 |
| 32 | 1.7 | Optimisation of the search sensitivity | 66 |
| 33 | 1.8 | Results | 71 |
| 34 | 1.9 | Interpretation | 73 |
| 35 | 1.9.1 | Systematic uncertainties of simulated signal samples | 73 |
| 36 | 1.9.2 | Statistical Methods/ Limit setting | 79 |
| 37 | 1.9.3 | Exclusion limits | 81 |
| 38 | 1.9.4 | Comparison to the search for disappearing tracks | 84 |
| 39 | 1.10 | Conclusion and outlook | 86 |
| 40 | A | Measurement of the jet transverse-momentum resolution | 89 |
| 41 | A.1 | Pileup reweighting | 89 |
| 42 | A.2 | Summary of all selection requirements | 90 |
| 43 | A.3 | Generator-level jet flavor definition | 90 |
| 44 | A.4 | Extrapolation plots | 91 |
| 45 | B | A search for highly ionising, short tracks | 91 |
| 46 | B.1 | Lifetime reweighting | 94 |
| 47 | B.2 | Event yields for simulated samples and data | 95 |
| 48 | B.3 | Signal contamination in validation regions | 99 |
| 49 | B.4 | Validation tests of the background estimation methods | 101 |
| 50 | B.5 | Selection requirements of the “tag-and-probe” samples | 103 |
| 51 | B.6 | Optimisation results with the number of missing outer hits | 106 |
| 52 | B.7 | Underlying distributions for the qualitative search sensitivity optimisation | 107 |
| 53 | B.8 | Trigger emulation | 108 |
| 54 | B.9 | Exclusion limits for all simulated lifetimes | 108 |

55

Part 1

56

A search for highly ionising, short tracks at the CMS detector

57

58 1.1 Motivation

59 Supersymmetry is able to offer solutions to many unexplained phenomena in astrophysics
60 and can solve many of the shortcomings of the Standard Model of particle physics (see
61 Section ??). While SUSY has been studied at previous particle colliders including Tevatron
62 and LEP [1,2], the LHC with its high centre-of-mass energy offers a unique opportunity to
63 investigate SUSY models with high sparticle masses that were not accessible in previous
64 experiments.

65 Therefore, a variety of searches were hunting for SUSY during Run I of the LHC from
66 2010 to 2012. Proton-proton collision data from the CMS and ATLAS experiments were
67 analysed with a strong focus on the search for SUSY in production channels via the strong
68 interaction (e.g. [3–5]). As a consequence, wide, previously unexplored regions of SUSY
69 parameter space are already excluded. However, due to the unknown mechanism of super-
70 symmetry breaking, the most general parametrisation of the Minimal Supersymmetric
71 Standard Model (MSSM) introduces over 100 new parameters and thus opens up an in-
72 credibly large phenomenological space. Therefore, SUSY models can lead to a plethora of
73 possible signatures at particle colliders, many of which could not - or not fully - be explored.

74

75 A very interesting signature occurs when sparticles live long enough to travel through a
76 part or the whole detector before decaying. This is possible for SUSY models with com-
77 pressed spectra, in which a sparticle can be long-lived because of phase-space suppression.
78 In Supersymmetry, such a mass-degeneracy naturally occurs if the wino mass parameter
79 (M_2) is smaller than the bino (M_1) and higgsino (μ) mass parameters. In this case, the
80 lightest chargino ($\tilde{\chi}_1^\pm$) and the lightest neutralino ($\tilde{\chi}_1^0$) are both wino-like and their mass
81 gap is fully determined by higher loop corrections (see Section ??). FIXME: is this really
82 correct! Therefore, they are almost mass-degenerate and the chargino is long-lived.

83 Such scenarios can be very interesting from a cosmological perspective as the wino-like
84 lightest supersymmetric particle, $\tilde{\chi}_1^0$, can serve as a plausible Dark Matter candidate [6,7].
85 While it is not possible to explain the full relic density with thermally produced wino-
86 like neutralinos for $m_{\tilde{\chi}_1^0} \lesssim 3$ TeV, neutralinos can still be the dominant part if they are
87 non-thermally produced via the decay of an almost decoupled particle [8,9]. Addition-
88 ally, these scenarios are well motivated by Supersymmetric models with anomaly-mediated
89 SUSY breaking (AMSB) [10,11], where the LSP is almost always the wino-like lightest
90 neutralino and the mass gap between the neutralino and chargino is typically between
91 140 MeV and 200 MeV [12]. FIXME - coult also cite pMMSM paper

92

SUSY scenarios with nearly mass-degenerate particles have two distinctive phenomenological properties that require a very different search strategy compared to general SUSY searches. First, because of the mass-degeneracy, the remaining decay product (e.g. a pion) is very soft in p_T , making it hard to detect. Since the other decay product, the neutralino, is only weakly interacting, it is very difficult to identify charginos via their decay products. Second, as the chargino is long-lived, it may traverse several detector layers before decaying. Thus, there is the possibility of reconstructing the chargino itself, e.g. as a reconstructed track in the tracker system.

101

Despite the exotic signatures of supersymmetric models with nearly mass-degenerate $\tilde{\chi}_1^\pm$ and $\tilde{\chi}_1^0$, current CMS searches are already sensitive to a very broad range of lifetimes. The exclusion power of existing SUSY searches can be assessed by interpreting their results in terms of the fraction of excluded parameter points in the phenomenological MSSM (see Section ?? for an introduction to the pMSSM). The results of such a study which has been performed in [13] are shown in Figure 1.1.1. It can be seen that general SUSY searches (blue area) are sensitive to shorter chargino lifetimes ($c\tau \lesssim 10$ cm).¹ Two existing searches, the search for long-lived charged particles [14] and the search for disappearing tracks [13] focus on long and intermediate chargino lifetimes, respectively. These two searches (purple and red areas) are sensitive to chargino lifetimes of $c\tau \gtrsim 35$ cm. Taken together, the existing searches exclude a large fraction of pMSSM points at different chargino lifetimes. However, there is a gap between the general SUSY searches and the search for disappearing tracks that is not accessible by any of the existing searches.

115

The here presented analysis aims at targeting this gap by optimising the search strategy for charginos with intermediate lifetimes of $10 \text{ cm} \lesssim c\tau \lesssim 40 \text{ cm}$. The targeted optimisation strategy is a combination of the strategies used in the search for long-lived charged particles [14] and the search for disappearing tracks [13]. While in [14], the high ionisation losses of hypothetical new massive particles is exploited, it does not take into account whether its reconstructed track is disappearing. In [13], the disappearance of the track is utilised but it does not incorporate the large ionisation losses into the search. Additionally, neither of the search does take into account the possibly very short tracks of early decaying charginos.

125

Thus, the here presented search is the first analysis at CMS combining the two signature properties that are highly distinctive for charginos with intermediate lifetimes: first, the

¹Since the pMSSM interpretation relied on the use of fast simulation techniques which are not capable of simulating charginos with lifetimes $c\tau > 1$ cm, the general SUSY searches were never interpreted in the context of SUSY models with longer chargino lifetimes.

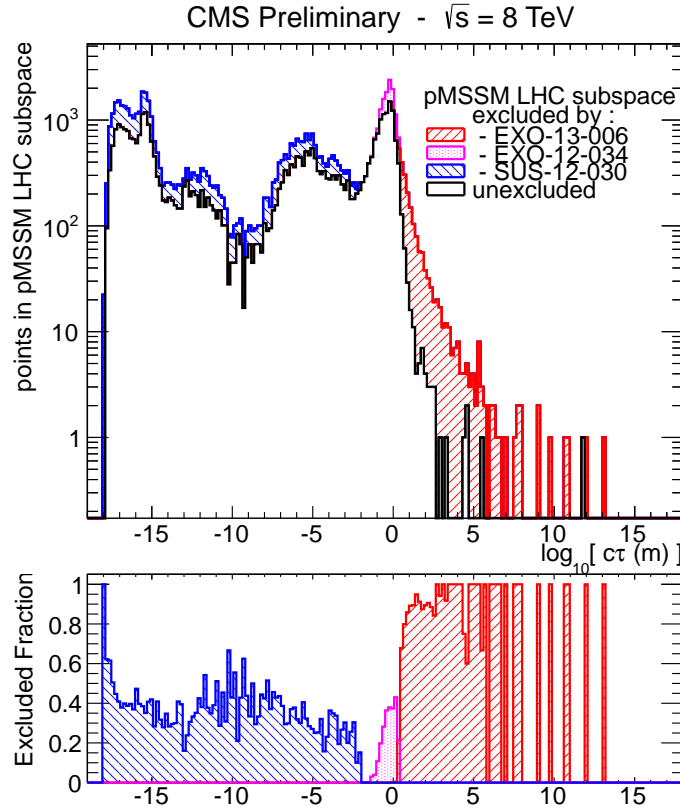


Figure 1.1.1: The number of excluded pMSSM points at 95% C.L. (upper part) and the fraction of excluded pMSSM points (bottom part) vs. the chargino lifetime for different CMS searches. Red area: the search for long-lived charged particles [14], Purple area: the search for disappearing tracks [13], Blue area: a collection of various general SUSY searches [15]. The black line indicates the unexcluded pMSSM parameter points. The sampling of the parameter space points was done according to a prior probability density function which takes pre-LHC data and results from indirect SUSY searches into account (see [16] for further details). Taken from: [17].

¹²⁸ characteristically high ionisation losses of heavy charginos; second, short reconstructed
¹²⁹ tracks due to chargino decays early in the detector.

¹³⁰ The associated challenges and the general search strategy of this analysis will be pre-
¹³¹ sented in the next section.

¹³² 1.2 General search strategy

¹³³ At the LHC, there are several possible chargino production channels. Chargino pairs can
¹³⁴ be produced through a photon or a Z -boson exchange. The chargino then decays via a
¹³⁵ virtual W -boson to the lightest neutralino and a fermion pair (e.g. a pion). This process is
¹³⁶ illustrated in the Feynman diagram in Fig. 1.2.1. Other possible chargino pair production
¹³⁷ channels include the exchange of a supersymmetric Higgs boson or a t-channel squark
¹³⁸ exchange (Fig. 1.2.2).

¹³⁹ Apart from pair production, charginos can be generated (produced) FIXME via the
¹⁴⁰ chargino-neutralino production channel. On tree-level, there exist two production mech-
¹⁴¹ anisms: the s-channel W -boson exchange and the t-channel squark exchange (Fig. 1.2.3).

¹⁴²

¹⁴³ Alternatively, charginos can be produced via strong production modes, i.e. in cascade
¹⁴⁴ decays of new heavy particles, such as gluinos or squarks. In the here presented search,
¹⁴⁵ the focus is, however, put on the electroweak production channels: chargino-pair and
¹⁴⁶ chargino-neutralino production.

¹⁴⁷

¹⁴⁸ When searching for supersymmetric models with long-lived $\tilde{\chi}_1^\pm$, the strategy is of course

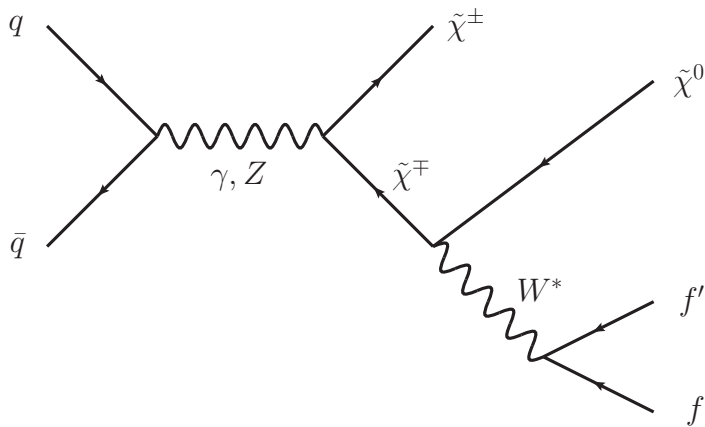


Figure 1.2.1: Feynman diagram of chargino pair production via gamma or Z -boson ex-
change and the subsequent decay via a virtual W -boson.

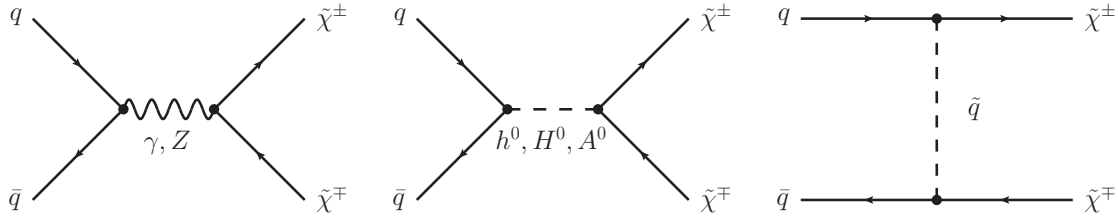


Figure 1.2.2: Main tree-level diagrams for chargino pair production.

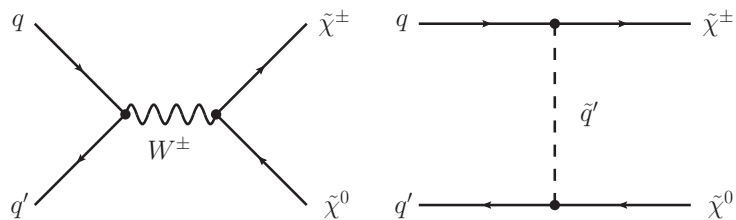


Figure 1.2.3: Main tree-level diagrams for chargino neutralino production.

¹⁴⁹ highly dependent on the actual lifetime of the chargino. For long lifetimes, the chargino
¹⁵⁰ can reach the muon chambers and can be reconstructed as a muon even despite a longer
¹⁵¹ time-of-flight [18]. For lower lifetimes, the chargino can already decay inside the detector
¹⁵² (e.g. the tracker), and hence can not be reconstructed as a muon but leads to an isolated,
¹⁵³ potentially disappearing track in the tracker. The detector signatures of these two scenar-
¹⁵⁴ ios are visualised in Fig. 1.2.4, where simulated chargino-chargino events are shown in a
¹⁵⁵ cross-sectional view of the CMS detector. In the left picture of Fig. 1.2.4, both charginos
¹⁵⁶ are reconstructed as muons, which can be seen by the energy deposition in the muon cham-
¹⁵⁷ bers. In the middle and right pictures both charginos have a lower lifetime of $c\tau = 0.5$ m
¹⁵⁸ and thus are only visible as tracks in the tracker, where both trajectories end inside the
¹⁵⁹ silicon strip tracker (coincidentally the tracks are equally long). Since this analysis tar-
¹⁶⁰ gets a search for Supersymmetry with charginos of lifetimes between $c\tau \approx 10$ cm – 40 cm,
¹⁶¹ the charginos decay rather early in the detector, possibly even in the inner layers of the
¹⁶² tracker. Thus, the signature of chargino events consists of isolated, short tracks and the
¹⁶³ signatures of the decay products, i.e. of a neutralino and a fermion pair.

¹⁶⁴ In case of R-parity conservation, one of the chargino decay products, the neutralino,
¹⁶⁵ is stable and weakly interacting, thus traversing the detector without leaving any further
¹⁶⁶ signature.

¹⁶⁷ The signature of the other decay product, the fermion pair, can in principle be used to
¹⁶⁸ select chargino events. However, for mass-degenerate charginos, it can be very hard or even

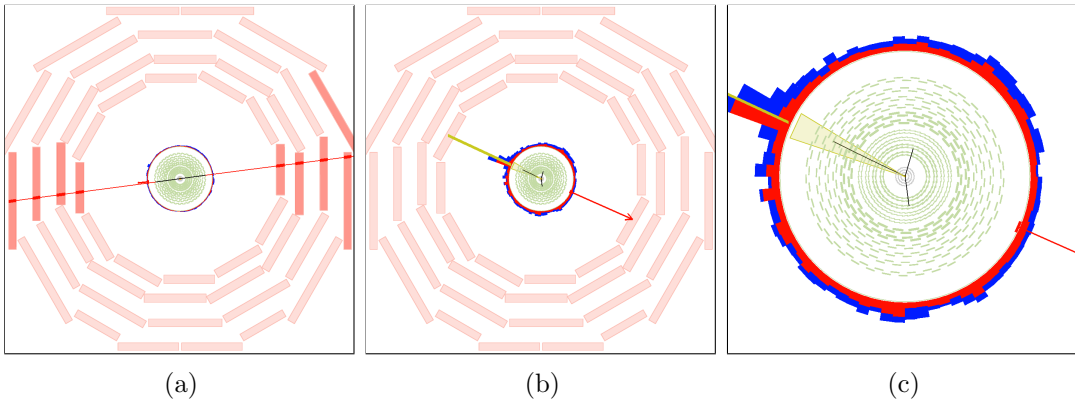


Figure 1.2.4: Visualisation of possible signatures of a chargino pair produced with a lifetime of $c\tau = 10\text{ m}$ (a) and a lifetime of $c\tau = 0.5\text{ m}$ (b and c). The muon chambers are the outer layers of the detector and are depicted as red boxes. The black lines represent the reconstructed chargino tracks. The right picture is a zoom of the picture in the middle. Here, only the cross-section of the tracker (green wavy lines for the strip and grey lines for the pixel) is displayed. The red arrow shows the missing transverse energy in the event. The red (blue) towers correspond to the energy deposition in the ECAL (HCAL). The ISR jet in the middle and right picture is indicated as yellow line.

impossible to detect these fermions as will be explained in detail in the next paragraph.

First of all, the fermionic decay product (e.g. a pion) can usually not be reconstructed because it does not originate from the primary vertex. Secondly, it is very low in momentum because of the mass-degeneracy between $\tilde{\chi}_1^\pm$ and $\tilde{\chi}_1^0$. The typical momentum of a pion originating from a chargino to neutralino decay in the $\tilde{\chi}_1^\pm$ rest frame is of the order

$$p_\pi \sim \sqrt{\left(m_{\tilde{\chi}_1^\pm} - m_{\tilde{\chi}_1^0}\right)^2 - m_\pi^2}. \quad (1.2.1)$$

For a mass gap between $\tilde{\chi}_1^\pm$ and $\tilde{\chi}_1^0$ of $\Delta m = 150\text{ MeV}$, the p_T distribution of the resulting pion peaks at $\sim 100\text{ MeV}$ and ends at $p_T \sim 400\text{ MeV}$ in the laboratory frame (Fig. 1.2.5).

176

If the transverse momentum of a particle is very low, the particle trajectory is much more bended compared to a particle with higher p_T (see Fig. 1.2.6 for illustration). Due to this bending, the track reconstruction efficiency of particles with a transverse momentum below 1 GeV decreases rapidly, reaching around 40% for isolated pions with a p_T of 100 MeV [19]. Furthermore, for pions that are not produced in the primary vertex, this reconstruction efficiency will be even smaller. It is therefore impossible to rely on a reconstruction of the fermionic chargino decay products in this analysis.

In summary, since an early decaying chargino is not reconstructed as a PF particle,

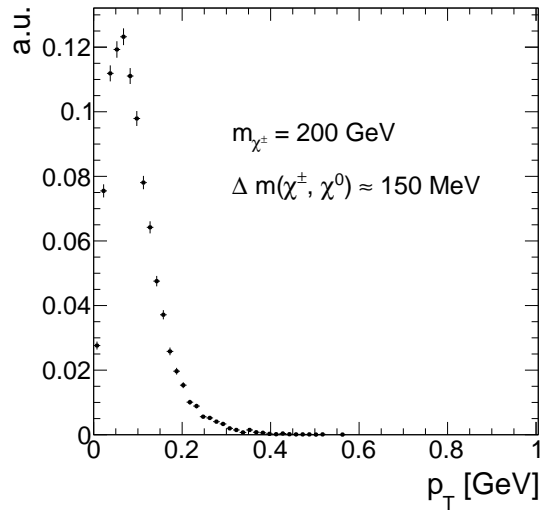


Figure 1.2.5: Transverse momentum distribution of pions coming from chargino decay into a neutralino with a mass gap of 150 MeV.

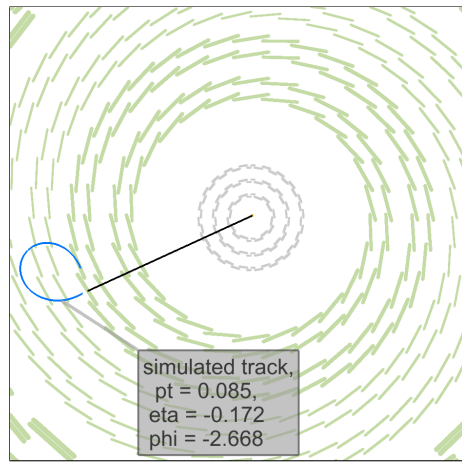


Figure 1.2.6: Cross-sectional view of the tracker (silicon strip (silicon pixel) tracker layers are illustrated with green (grey) lines) and a simulated chargino track (black line) decaying to a pion (bended blue line) with a p_T of $\sim 85 \text{ MeV}$ and a neutralino (not visible).

185 the event signature of a chargino-pair or a chargino-neutralino event consists only of one
 186 (or two) - potentially - disappearing track. Such a signature is very difficult to detect,
 187 especially since CMS doesn't offer a dedicated track trigger so that triggering on the
 188 chargino track is impossible.

189 In order to search for such signatures, one therefore needs to trigger on other, less obvious
 190 properties of chargino events. This analysis takes advantage of higher order contributions
 191 to the Feynman diagrams shown in Figs. 1.2.2 and 1.2.3, resulting in initial state radiation
 192 (ISR). If the initial quarks radiate a high p_T gluon, the resulting jet can be detected and
 193 can offer a possibility to search for events with apart from the ISR jet, nothing more than
 194 isolated tracks. Furthermore, the non-detection of the chargino's decay products plus a
 195 high p_T ISR jet leads to missing transverse energy (MET) in the event. Exploiting these
 196 two circumstances, it is possible to detect chargino-pair or chargino-neutralino events with
 197 the help of Jet+MET triggers.

198 Since Jet+MET triggers are not very specific for chargino events, it is important to
 199 identify further track properties that can be used to select chargino candidates. One
 200 distinctive property of charginos compared to SM particles is their high mass. Since at
 201 pp -colliders the transverse-momentum distribution depends FIXME Therefore, charginos
 202 can be identified by selecting high p_T tracks. Furthermore, the energy loss per path length
 203 (dE/dx) depends quadratically on the particle's mass for low velocities ($0.2 < \beta\gamma < 0.9$):

$$\langle \frac{dE}{dx} \rangle = K \frac{m^2}{p^2} + C \quad (1.2.2)$$

204 Therefore, dE/dx constitutes a very nice discriminating variable for massive particles like
 205 charginos against SM particles. The selection of chargino events in this analysis thus relies
 206 on the selection of isolated high p_T tracks with high dE/dx values.

207 If the chargino decays before it has crossed the full pixel and strip detector, the as-
 208 sociated track is disappearing. For low lifetimes, the tracks can be very short and can
 209 have only a few hits in the detector. In order to reconstruct a particle's trajectory, a
 210 minimum of three hits are required since defining a helical path requires five parameters
 211 (see [19]). A specific challenge for this analysis is hence the combination of searching for
 212 short tracks and utilising the measurement of the energy deposition of the chargino. For
 213 very short tracks, eventually only passing the first couple of layers of the whole tracker
 214 system, the pixel tracker information becomes very important. Therefore, an accurate
 215 energy measurement in the pixel system is of great importance to this analysis. However,
 216 no other CMS analysis has used the energy information of the pixel tracker so far. This
 217 analysis thus requires a thorough study of the quality of the pixel energy calibration and,
 218 potentially, a recalibration in case the pixel energy calibration is not sufficient.

219 1.2.1 Comparison to earlier searches

220 As already mentioned before, there are two analyses at CMS at $\sqrt{s} = 8$ TeV with 20 fb^{-1}
 221 data that search for intermediate lifetime charginos, the search for long-lived charged
 222 particles [14] and the search for disappearing tracks [13]. The here presented analysis
 223 aims at achieving an increase in sensitivity towards shorter lifetimes compared to the ear-
 224 lier analyses in a twofold way. First, the selection is optimised for the inclusion of very
 225 short tracks. Second, the inclusion of the variable dE/dx is used to increase the search
 226 sensitivity compared to [13].

227

228 In [14], a minimum number of eight hits were required for every track, whereas [13]
 229 required a minimum of seven hits. This can be very inefficient for shorter lifetimes, where
 230 most of the charginos already decay shortly after the pixel tracker. In Fig. 1.2.7 (left),
 231 the normalised distribution of the number of measurements (N_{hits}) of chargino tracks is
 232 shown. It can be seen, that N_{hits} peaks at the minimal possible value needed for track
 233 reconstruction of $N_{\text{hits}} = 3$ for lower lifetimes. For a lifetime of $c\tau = 100\text{ cm}$, a second
 234 peak at ~ 17 hits appears corresponding to the number of measurements when crossing
 235 all pixel barrel (3) and strip inner and outer barrel (6 from stereo and 8 from normal)
 236 layers. However, a notable fraction of $\sim 40\%$ of chargino tracks still has a number of
 237 measurements of $N_{\text{hits}} < 8$.

238 It should be also mentioned, that the track reconstruction efficiency is sufficient for
 239 short chargino tracks, such that a loosening of the N_{hits} requirement is expected to be
 240 really improving the signal acceptance. The track reconstruction efficiency for different
 241 chargino decay points is depicted in Fig. 1.2.7 (right). For very short tracks ($N_{\text{hits}} = 3$)
 242 the efficiency is still around 20%.

243

244 Additionally, the search for disappearing tracks which targets models with charginos
 245 decaying inside the tracker did not make use of the high energy deposition of heavy parti-
 246 cles. Although this variable was indeed used in the search for long-lived charged particles,
 247 this search was not optimised for intermediate lifetimes (e.g. no explicit muon veto on the
 248 selected tracks was required). Thus, it shows less sensitivity compared to the disappearing
 249 track search in the lifetime region between $35\text{ cm} \lesssim c\tau \lesssim 100\text{ cm}$ (see Fig. 1.1.1).

250

251 To conclude, the general search strategy of the here presented analysis is to unite the
 252 strategies of [14] and [13] and to lower the strong selection on the number of hits in these
 253 analyses in order to get an optimised selection for lifetimes around $10\text{ cm} \lesssim c\tau \lesssim 40\text{ cm}$.

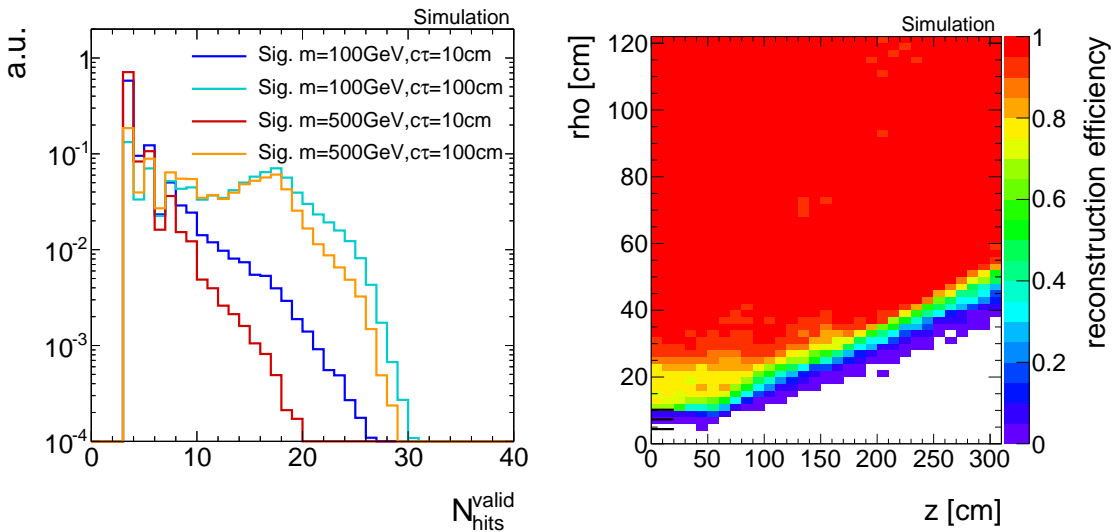


Figure 1.2.7: Left: Number of measurements in the tracker system N_{hits} for four different signal lifetimes. Right: Probability to reconstruct a track (z) in dependency of the chargino's decay point (x and y). More information on the generation of the simulated signal samples can be found in Section 1.4.2.

254 1.3 Improved dE/dx measurement for short tracks

255 As already pointed out in the previous chapter, the inclusion of the pixel energy mea-
 256 surements can increase the sensitivity when searching for short and highly ionising tracks.
 257 While the energy measurements in the silicon strip detector have already been calibrated
 258 as part of the search for long-lived charged particles [14], no complete calibration has been
 259 done for the pixel silicon tracker so far. To increase the discrimination power of dE/dx for
 260 short tracks, such a calibration procedure has therefore been performed within this PhD
 261 thesis.

262

263 The CMS tracker system provides a measurement of the particle's energy loss for each
 264 hit in the tracker. This is done by the detection of the number of electrons produced by
 265 the ionisation of the silicon. A detailed introduction to the CMS tracker system and the
 266 energy measurement can be found in Section ??.

267 How to combine the single energy measurements for each tracker hit into one track
 268 dE/dx estimator that can be used for analysis purposes will be explained in the following

269 Section 1.3.1. The pixel energy calibration is then described in Section 1.3.2. How to
 270 discriminate SM particles and beyond SM particles with the help of a dE/dx measurement
 271 is discussed in Section 1.3.3, followed by an exploration of how the inclusion of the pixel
 272 energy measurements in the dE/dx estimates leads to a better discrimination between
 273 Standard Model particles and long-lived charginos (Section 1.3.4).

274 1.3.1 Estimation of the ionisation loss of charged particles

275 Energy losses for moderately relativistic charged particles travelling through matter are
 276 mostly caused by ionisation effects. The mean energy loss per path length can be described
 277 with the Bethe formula [20]:

$$\langle \frac{dE}{dx} \rangle = K z^2 \frac{Z}{A} \frac{1}{\beta^2} \left[\frac{1}{2} \ln \frac{2m_e c^2 \beta^2 \gamma^2 T_{\max}}{I^2} - \beta^2 - \frac{\delta(\beta\gamma)}{2} \right]. \quad (1.3.1)$$

278 It is a function of the atomic number (Z), the atomic mass (A) of the absorber, and the
 279 mean excitation energy (I) which is 173 eV for silicon [21]. T_{\max} represents the maximum
 280 energy transfer in a single collision. The relevant particle's properties are the velocity (β),
 281 the Lorentz factor (γ) and the charge (z) of the incident particle. The density correction
 282 $\delta(\beta\gamma)$ reduces the mean energy loss at high energies because of polarisation effects of the
 283 material. The factor K is constant and is 0.307 in units of MeV mol⁻¹ cm². The Bethe
 284 formula is valid if the main energy loss originates from ionisation effects, i. e. in a region
 285 between $0.1 \lesssim \beta\gamma \lesssim 1000$.

286 Even if widely used, the mean energy loss is a quantity which is “ill-defined experimen-
 287 tally and is not useful for describing energy loss by single particles” [22]. The problem is
 288 caused by the underlying probability distribution of one single dE/dx measurement (this
 289 will be named $\Delta E/\Delta x$ throughout the following sections), which can be parametrised by
 290 a Landau distribution [23]

$$p(x) = \frac{1}{\pi} \int_0^\infty e^{-t \log t - xt} \sin(\pi t) dt. \quad (1.3.2)$$

291 The Landau distribution has no free parameters. Its most probable value is around 0.222.
 292 However, it is possible to introduce artificially a different most probable value and a width
 293 (at half maximum) with $x \rightarrow \frac{x - \text{MPV}}{\sigma} - 0.222$. The Landau distribution is a highly asym-
 294 metric distribution with a long tail towards large x values (see Fig. 1.3.1). Theoretically it
 295 extends to infinite energies, however in nature the maximal deposited energy is of course
 296 limited by the particle's full energy.

297 Because of its strong asymmetry, measurements of the mean energy loss per path length
 298 $\langle dE/dx \rangle$ with only a few single measurements are easily fluctuating towards high values.
 299 This makes the use of the mean energy loss described by the Bethe formula for the discrim-

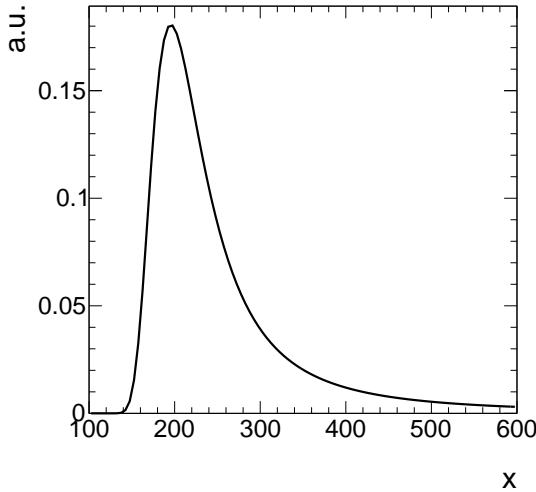


Figure 1.3.1: Illustration of the shape of a Landau distribution. Parameters were chosen as $\mu = 200$ and $\sigma = 20$.

ination of new heavy particles problematic, because fluctuations to high values reduce the discrimination power against massive particles which release in general higher amounts of energy in matter.

A much better observable is the most probable value (MPV) of the Landau distribution. The MPV is much more stable compared to the mean and is not subject (FIXME) to high dE/dx fluctuations. The most probable energy loss of a charged particle, Δ_p , can be described by the Landau-Vavilov-Bichsel equation [24]:

$$\Delta_p = \xi \left[\ln \frac{2m_e c^2 \beta^2 \gamma^2}{I} + \ln \frac{\xi}{I} + j - \beta^2 - \delta(\beta\gamma) \right], \quad (1.3.3)$$

with $\xi = (K/Z)(Z/A)(x/\beta^2)$. The thickness of the absorber x appears explicitly in the Landau-Vavilov-Bichsel equation making the most probable energy loss per path length Δ_p/dx logarithmically dependent on x . A comparison between the Bethe mean energy loss $\langle dE/dx \rangle$ and the most probable energy loss Δ_p/dx for muons is shown in Fig. 1.3.2.

Particles such as muons are minimally ionising in silicon for $\beta\gamma \sim 3 - 4$. For higher momenta the deposited energies increase again reaching a plateau at around $\beta\gamma \sim 100$. However, new heavy charged particles would mainly be unrelativistic because of their high mass and would therefore deposit much higher energies in the detector. This makes dE/dx a very well discriminating variable. Thus, the energy loss per path length can be used to discriminate between SM particles and new heavy charged particles due to the different velocity distributions.

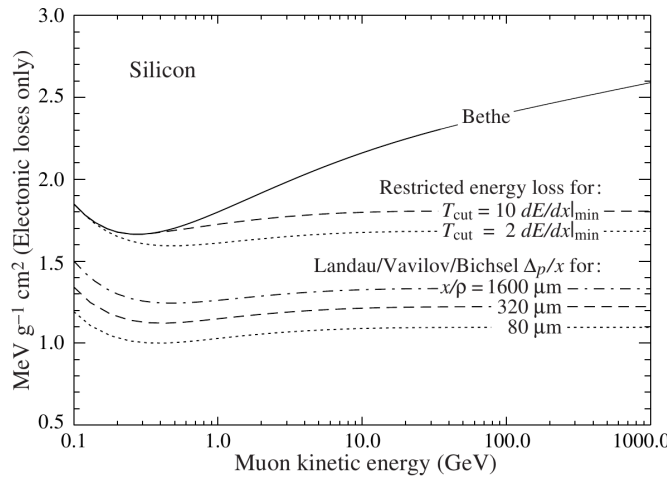


Figure 1.3.2: Comparison between the Bethe mean energy loss, restricted energy loss and the most probable energy loss described by the Landau-Vavilov-Bichsel function for muons for different values of absorber thickness of silicon. Taken from [22].

319

As said before, the most probable energy loss is much more stable compared to the Bethe mean energy loss. Still, combining only a few measurements of $\Delta E/\Delta x$ can also lead for $\Delta p/x$ to large fluctuations towards high dE/dx values. In order to estimate experimentally the most probable dE/dx value from only a few energy measurements, several “estimators” can be used that suppress a potential bias towards the high end without introducing a bias towards lower values [25]. One of the estimators for determining a track’s dE/dx is the harmonic-2 estimator

$$I_{\text{H2}} = \left(\frac{1}{N} \sum_{i=1}^N (\Delta E_i / \Delta x_i)^{-2} \right)^{-1/2}, \quad (1.3.4)$$

where $\Delta E_i / \Delta x_i$ corresponds to the ΔE and Δx measurement in the i th hit of the track. This estimator is known to be robust and is not easily biased by large fluctuations in $\Delta E/\Delta x$ because of the suppression by the power of minus two [25].

A further estimator of dE/dx used for the discrimination of highly ionising particles will be introduced in Section 1.3.3.

332 1.3.2 Energy calibration of the silicon pixel tracker

During Run I in 2012, the pixel silicon detector was continuously subjected to an energy calibration, a so-called gain calibration. Every pixel was calibrated to the same response,

so that the whole pixel tracker should have been well inter-calibrated [26]. Unfortunately, due to various reasons, such as the imperfect constancy of the reference signal, or radiation and temperature induced changes, the energy calibration could not ensure a fully calibrated pixel tracker.

This imperfection of the gain calibration can be seen in Fig. 1.3.3, where the mean of the harmonic-2 estimator for all tracks $\langle I_{h2} \rangle$ over the full data-taking period in 2012 is shown. Four different steps can be spotted. The first and the third steps correspond to changes in the settings of the tracker due to irradiation. The second and fourth step are induced by associated adjustments in the online gain calibration. Unfortunately, although the gain calibration was adjusted (even with some delay), it was not able to ensure a constant energy response of the pixel tracker over time. The variations of the dE/dx measurement over time of around 15% are too large to use dE/dx without a further calibration.

The following sections explain the method of the gain calibration of the pixel silicon tracker which is performed for this analysis. It is splitted into two sections. The first section is dedicated to the gain inter-calibration of the pixel tracker which ensures a homogeneous energy response of all tracker modules. In the second section, the absolute gain calibration is discussed. This calibration step is needed to ensure that the measurement of the energy release of a particle is actually translated to the correct physical value.

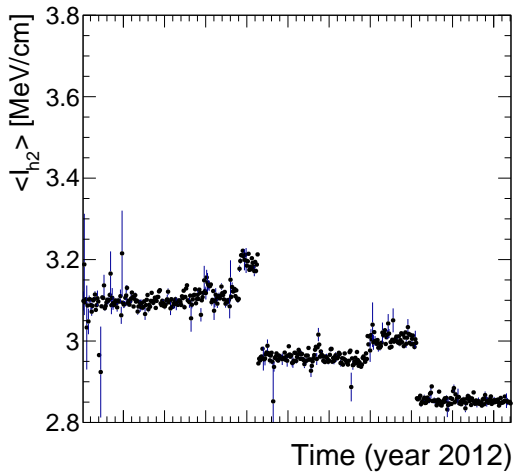


Figure 1.3.3: Mean of all track’s dE/dx (harmonic-2 estimator) over the full year 2012. Only pixel hits are taken into account. Every data point corresponds to one run.

353 Inter-calibration of gain

354 The main goal of the gain calibration is to get a uniform response in the ionisation energy
 355 loss dE/dx over the full data taking period in 2012. To also ensure a uniform response
 356 over all modules within one time step, an additional inter-calibration on module level is
 357 carried out. The inter-calibration can in principle be done on various levels: the highest
 358 granularity would be a calibration on pixel level, followed by a calibration on read-out-chip
 359 (ROC) level and then on module-level. Lower granularities in descending order are rings
 360 (modules with same z-position) and finally layers (3 layers in the barrel and 4 disks in the
 361 endcap). It is verified that all pixels [26] and all ROCs (on one module) are sufficiently
 362 inter-calibrated, such that the inter-calibration is finally done module-wise. For the pixel
 363 inter-calibration it is relied on [26], whereas the spread of derived calibration factors of
 364 all ROCs within one module was analysed to be around 5% for most of the pixel modules
 365 (see Fig. ?? in AppendixFIXME). FIXME:talk to Markus

366 The gain calibration of the pixel silicon tracker is carried out with the help of minimally
 367 ionising particles (MIPs). MIPs in this context are not defined as particles at the minimum
 368 of the Bethe formula, but more generally as particles located at or near the plateau of
 369 the dE/dx distribution vs. momentum (see Fig. 1.3.2). This approach ensures that all
 370 particles deposit similar amounts of energy so that the variation due to different momenta
 371 is minimised.

372 MIPs are selected by a momentum selection of $p > 2$ GeV. Additionally, only tracks
 373 with at least eight hits and a $\chi^2/\text{n.d.o.f.} < 3$ are used to ensure a high-quality track
 374 reconstruction. A sample containing around 50 million “minimum bias” events is used for
 375 calibration. The “minimum bias” sample was specifically recorded for tracker calibration
 376 purposes.

377 For every module in the pixel tracker (there are 1440 modules in total), a distribution
 378 of the energy loss per path length $\Delta E/\Delta x$ is built. The measurement of $\Delta E/\Delta x$ is
 379 done in ADC counts per mm. ADC counts are a measure for the deposited charge after
 380 digitisation. Figure 1.3.4 shows an example distribution for one module. The underlying
 381 Landau distribution can be seen. To extract the MPV for every module a fit to the core
 382 distribution is performed. The fit is not only done with a Landau but a Landau convoluted
 383 with a Gaussian function to be closer to the experimentally observed energy spectrum.
 384 This also increases the fit performance and the stability of the fit. The path length Δx is
 385 calculated with

$$\Delta x = d_{\text{module}_i} \cdot \cos(\phi_{\text{track}}), \quad (1.3.5)$$

386 where d_{module_i} is the thickness of module i and ϕ_{track} is the relative angle of the particle’s
 387 trajectory to the normal axis of the module. With the measured MPV extracted from the

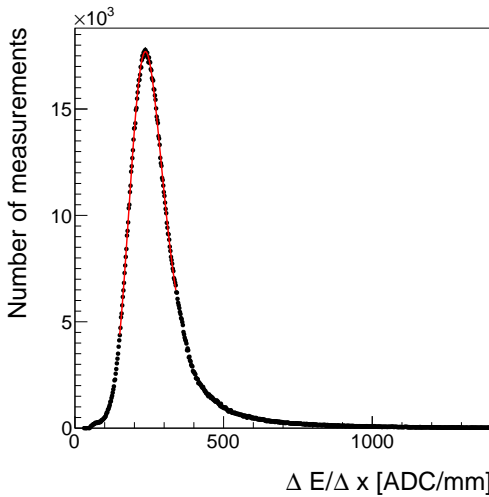


Figure 1.3.4: An example of the $\Delta E/\Delta x$ distribution measured in ADC count per mm for one module of the CMS pixel tracker. A Landau convoluted with a Gaussian is fitted to the core of the distribution in an iterative procedure.

388 fit, an inter-calibration factor is calculated for every module

$$c_{\text{inter}} = \frac{\text{MPV}_{\text{target}} [\text{ADC/mm}]}{\text{MPV} [\text{ADC/mm}]} = \frac{300 \cdot 265 \text{ ADC/mm}}{\text{MPV} [\text{ADC/mm}]} . \quad (1.3.6)$$

389 The factor $300 \cdot 265 \text{ ADC/mm}$ is in principal an arbitrary number since the final response
 390 is adjusted by the absolute gain calibration described in the next section. However, it is
 391 chosen such that the measured calibration factors are close to one. The calibration factor
 392 can then be used to scale every single measurement in a module to a calibrated $\Delta E/\Delta x$
 393 measurement

$$\left(\frac{\Delta E}{\Delta x} \right)_{\text{calibrated}} = c_{\text{inter}} \cdot \left(\frac{\Delta E}{\Delta x} \right)_{\text{uncalibrated}} \quad (1.3.7)$$

394 The determination of the calibration factor is done for every of the five time steps, shown
 395 in Fig. 1.3.3 independently, in order to get rid of the time dependency. The outcome of
 396 the application of the calibration factors to the single energy measurements in the pixel
 397 tracker can be seen in Fig. 1.3.5. The variation over time is indeed eliminated, resulting
 398 in a maximal time variation of less than $\sim 1\%$.

399 Additionally, the same procedure is carried out for a corresponding simulated data
 400 sample to ensure the inter-calibration of the pixel modules on all simulated samples.

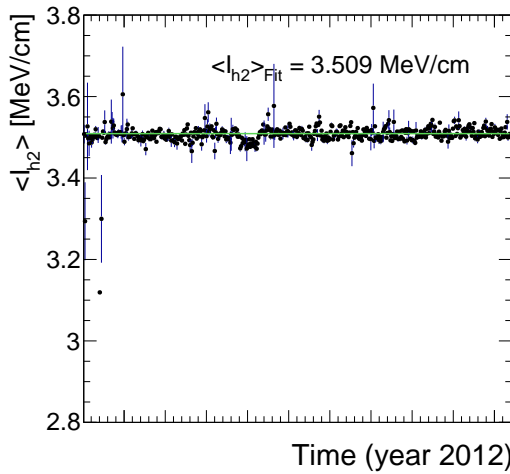


Figure 1.3.5: Mean of all track's dE/dx (harmonic-2 estimator) over the full year 2012 after applying the calibration factors, resulting in an average dE/dx of 3.51 MeV/cm. Only pixel hits are taken into account. Every data point corresponds to one run.

401 **Absolute calibration of gain**

402 As a final step, the targeted MPV being $\text{MPV}_{\text{target}} = 300 \cdot 265 \text{ ADC/mm}$ needs to be
 403 translated to a meaningful physical quantity given in physical units (e.g. MeV/cm). That
 404 means, that the charge measurement in ADC counts needs to be converted to the real
 405 energy release from a particle. The relation between ΔE in ADC counts and the energy
 406 loss in eV is given by

$$\Delta E [\text{eV}] = c_{\text{inter}} \cdot \Delta E [\text{ADC}] \cdot \frac{N_e}{\text{ADC}} \cdot 3.61 \text{ eV}, \quad (1.3.8)$$

407 where N_e/ADC is the number of electrons which correspond to one calibrated ADC count
 408 and 3.61 eV is the mean energy needed to create one electron-hole pair in silicon at -10°C .
 409 Such an absolute gain calibration can be done with the help of several methods (all ex-
 410 plained in [25]). The absolute calibration of the silicon pixel tracker can rely on the already
 411 performed/accomplishedFIXME absolute calibration of the silicon strip detector. In [25],
 412 the absolute gain calibration was done with the help of the most probable energy release
 413 per path length of muons, theoretically described by the Landau-Vavilov-Bichsel formula
 414 in Eq. (1.3.3). To calibrate the pixel tracker to the correct energy loss per path length it
 415 is therefore sufficient to determine one calibration factor to relate the average dE/dx of
 416 all tracks in the pixel tracker as shown in Fig. 1.3.5 to the average measured dE/dx in the

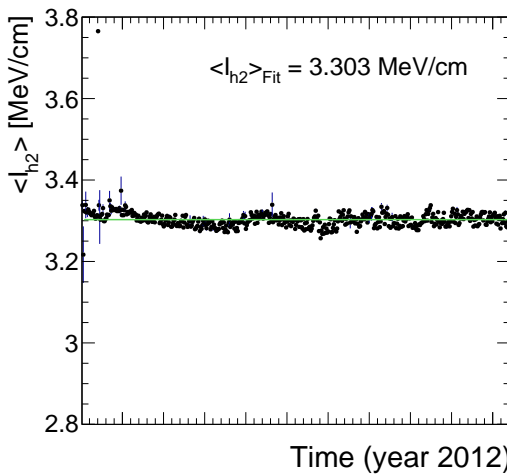


Figure 1.3.6: Mean of all track’s dE/dx (harmonic-2 estimator) measured in the silicon strip detector over the full year 2012. The average most probable dE/dx is $I_{h2} = 3.303 \text{ MeV/cm}$. Every data point corresponds to one run.

⁴¹⁷ strip tracker, shown in Fig. 1.3.6 by

$$c_{\text{absolute}} = \frac{\langle dE/dx_{\text{strip}} \rangle}{\langle dE/dx_{\text{pixel}} \rangle} = \frac{3.303}{3.509} = 0.941. \quad (1.3.9)$$

⁴¹⁸ This factor is then applied on top of c_{inter} for all pixel modules.

⁴¹⁹ Finally, an absolute calibration factor needs to be determined for the simulated samples,
⁴²⁰ where the simulated pixel tracker is calibrated to the average dE/dx of the silicon strip
⁴²¹ measured in data.

⁴²² 1.3.3 Discrimination of highly-ionising particles

⁴²³ As mentioned before, it is difficult to find a robust estimator for the most probable energy
⁴²⁴ loss of a particle, if only a few measurements of $\Delta E/\Delta x$ along the particle’s trajectory
⁴²⁵ are available. The harmonic-2 estimator I_{h2} was already introduced in Section 1.3.1 in
⁴²⁶ Eq. (1.3.4). It is known to be a robust estimator not easily affected by large fluctuations in
⁴²⁷ $\Delta E/\Delta x$. However, it was shown in [25] that a better discrimination between SM particles
⁴²⁸ and possible new heavy particles can be achieved when using likelihood techniques, i. e.
⁴²⁹ determining the probability that the set of all $\Delta E/\Delta x$ belonging to one track is actually
⁴³⁰ compatible with the hypothetical probability distribution of a MIP.

⁴³¹ That a measured sample has been drawn from a specific distribution can be tested with
⁴³² the co-called Smirnov-Cramér-von Mises test [27, 28]. It is deduced from the integral of

433 the squared difference of a measured distribution to a hypothesis distribution, and leads
 434 to a test statistics of [25]

$$I_s = \frac{3}{N} \cdot \left(\frac{1}{12N} + \sum_{i=1}^N \left[P_i - \frac{2i-1}{2N} \right]^2 \right), \quad (1.3.10)$$

435 where N is the total number of energy measurements and P_i is the cumulative probability
 436 that a MIP would release a $\Delta E/\Delta x$ equal or smaller than the measured $\Delta E/\Delta x$ with all
 437 P_i arranged in increasing order.

438 However, this test statistics is not sensitive to the sign of the difference between the
 439 measured and the theoretical distribution. It can therefore not distinguish between in-
 440 compatibilities due to variations towards higher or lower energy deposits compared to the
 441 hypothesis distribution. Thus it is not optimal for the discrimination between MIPs and
 442 heavy new particles by dE/dx . A so-called Asymmetric Smirnov-Cramér-von Mises dis-
 443 criminator was developed in [25] which is only sensitive to incompatibilities to the MIP
 444 hypothesis towards higher energy depositions

$$I_{as} = \frac{3}{N} \cdot \left(\frac{1}{12N} + \sum_{i=1}^N \left[P_i \cdot \left(P_i - \frac{2i-1}{2N} \right)^2 \right] \right). \quad (1.3.11)$$

445 A value of I_{as} close to zero indicates good compatibility with the MIP hypothesis, whereas
 446 a value close to one indicates bad compatibility because of unexpectedly high energy losses.

447 The underlying probability P_i of the energy release for a given path length in the pixel
 448 tracker is extracted from the same “minimum bias” sample used for the pixel energy
 449 calibration. In total 28 different templates each for a different given path length are
 450 created. In Fig. 1.3.7 the probability distribution template for the pixel tracker in data
 451 and simulation is shown. The corresponding templates for the energy release in the silicon
 452 strip detector were already built by [25].

453 A comparison between the energy release by MIPs (I_{as}) in data and simulation for
 454 high-quality tracks with $p > 5$ GeV and $|\eta| < 2.1$ can be found in Fig. 1.3.8.

455 dE/dx shows good agreement in data and simulation for $I_{as} < 0.1$. For larger values, I_{as}
 456 shows a larger decrease in simulation than in measured data. For this reason a data-based
 457 approach for analyses exploiting dE/dx information is needed.

458

459 1.3.4 Discrimination improvements

460 The goal of including the pixel energy information is to increase the discrimination power
 461 of I_{as} between background and signal tracks, especially for shorter lifetimes. In Fig. 1.3.9
 462 (left), a comparison of the shapes of the energy release by MIPs and by signal tracks in

⁴⁶³ simulation is shown (details about the simulated samples can be found in the next section
⁴⁶⁴ Section 1.4.2). It can be seen, that the I_{as} distributions of the signal models show a larger
⁴⁶⁵ tail towards $I_{\text{as}} = 1$, whereas the I_{as} of the background is rapidly falling.

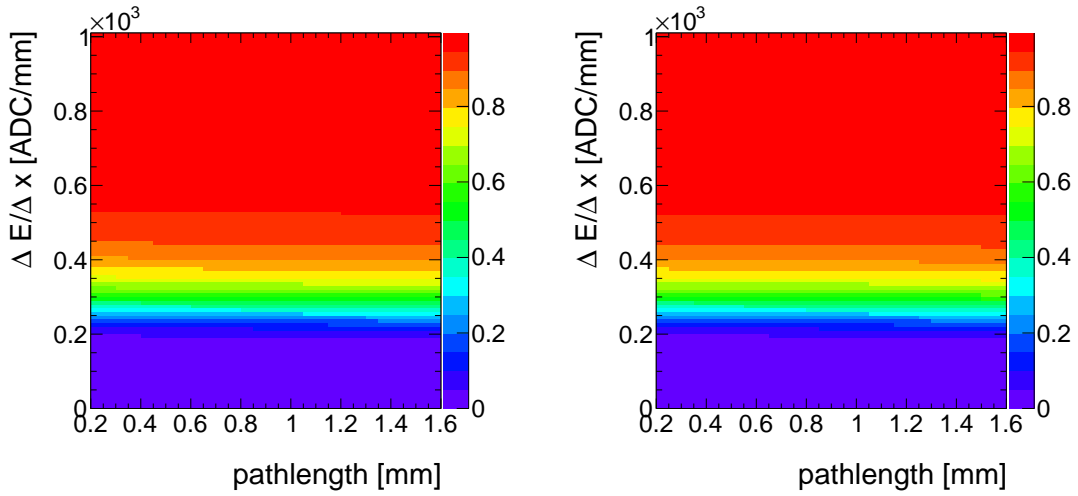


Figure 1.3.7: Cumulative probability for a MIP to release a $\Delta E/\Delta x$ (y-axis) vs. the path length (x-axis) in data (left) and simulation (right) for the pixel tracker based on the “minimum bias” sample.

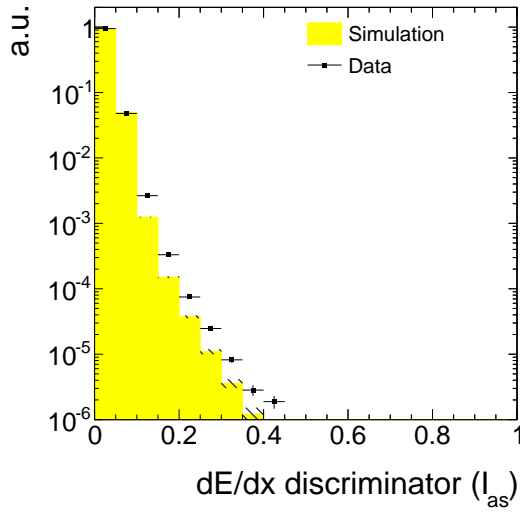


Figure 1.3.8: Normalised I_{as} distribution for MIPs from the minimum bias sample in data and simulation for high-quality (high purity as defined in [29], a minimum number of eight hits and no missing inner and middle hits) tracks with $p > 5 \text{ GeV}$ and $|\eta| < 2.1$.

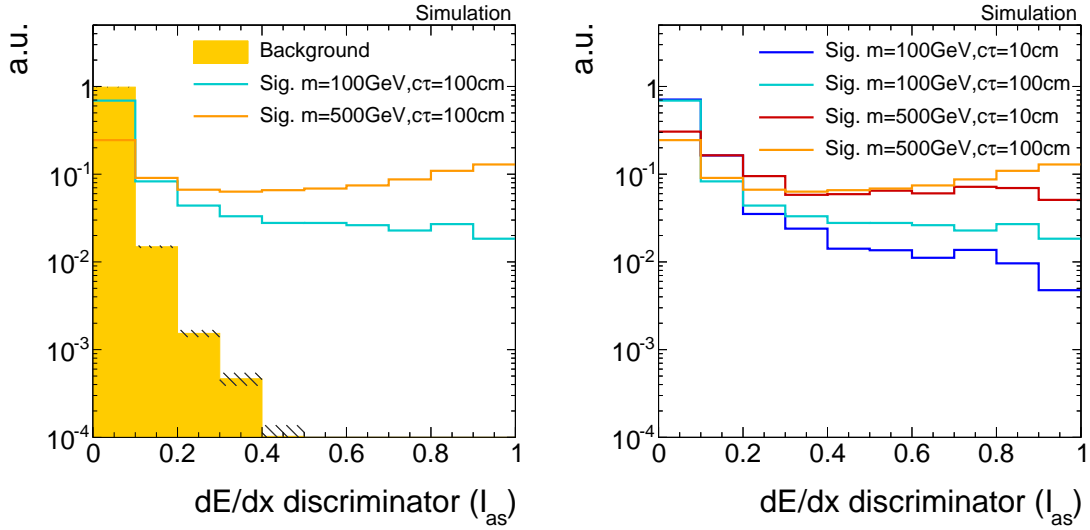


Figure 1.3.9: Normalised I_{as} distribution for simulated background and signal tracks (left) and for four different signal models (right) for high-purity tracks (as defined in [29]) with $p_T > 10 \text{ GeV}$ and $|\eta| < 2.1$. For the illustration of the background tracks' spectrum simulated $t\bar{t} + \text{jets}$ events are used (more information about this sample is given in Chapter 1.4).

466 In the right part of Fig. 1.3.9, a comparison of the I_{as} distributions of four different
 467 signal models is shown. Charginos with longer lifetimes have a more pronounced tail
 468 toward $I_{as} = 1$. This can be understood with the help of Eq. (1.3.3), where the influence
 469 of the velocity (β) on the ionisation loss can be seen. The velocity distribution of the
 470 charginos is mostly affected by the mass of the chargino. However, also for charginos
 471 with same mass, the velocity is higher in average for shorter lifetimes. This is caused
 472 by the fact, that for shorter lifetimes (e.g. $c\tau = 10 \text{ cm}$), already a sizable fraction of
 473 the charginos decay before reaching the tracker system. The probability of reaching the
 474 detector increases for higher velocities because of the boost, which can be clearly seen at
 475 the survival probability

$$P(t) = e^{-\frac{t}{\gamma\tau}}. \quad (1.3.12)$$

476 This means that the track reconstruction/selection lead to a biased average β for shorter
 477 lifetimes which in turn lead to lower values of I_{as} .

478 The I_{as} distribution is not only influenced by the velocity of a particle but also by the
 479 number of hits of a track. The number of measurements in the tracker system defines the
 480 influence of single fluctuations in $\Delta E/\Delta x$ on the I_{as} discriminator, because of the long
 481 right tail of the Landau distribution. A low number of hits, therefore, leads to higher I_{as}
 482 values. This effect is also visible in Fig. 1.3.9 (right). The small surplus for lower lifetimes
 483 between 0.1 and 0.2 is caused by the smaller number of measurements for earlier decaying

484 charginos.

485 Finally, the impact of the additional $\Delta E/\Delta x$ information from the pixel tracker on the
486 selection efficiency of signal and background tracks is quantified. Figure 1.3.10 shows the
487 signal selection efficiency against the background selection efficiency for different selection
488 cuts in I_{as} , once including the pixel information and once without it. The background
489 selection efficiency is estimated with simulated $W+\text{jets}$ events but was additionally checked
490 on simulated $t\bar{t}+\text{jets}$ and QCD-multijet events (further information about the simulated
491 samples can be found in the next Chapter 1.4). No significant difference between these
492 processes in the background selection efficiency was observed.

493 The signal selection efficiency and the background suppression depend on the mass and
494 the lifetime of the charginos. The improvement of the discriminating power is much more
495 pronounced for higher chargino masses.

496 It can be seen that the inclusion of the pixel information increases the background
497 suppression for a given signal efficiency throughout the investigated signal models. This
498 background suppression improvement is most pronounced for very tight cuts on I_{as} up
499 to a factor of 20 and even more and still considerable for looser selections with signal
500 efficiencies of around 40% (factor of 10).

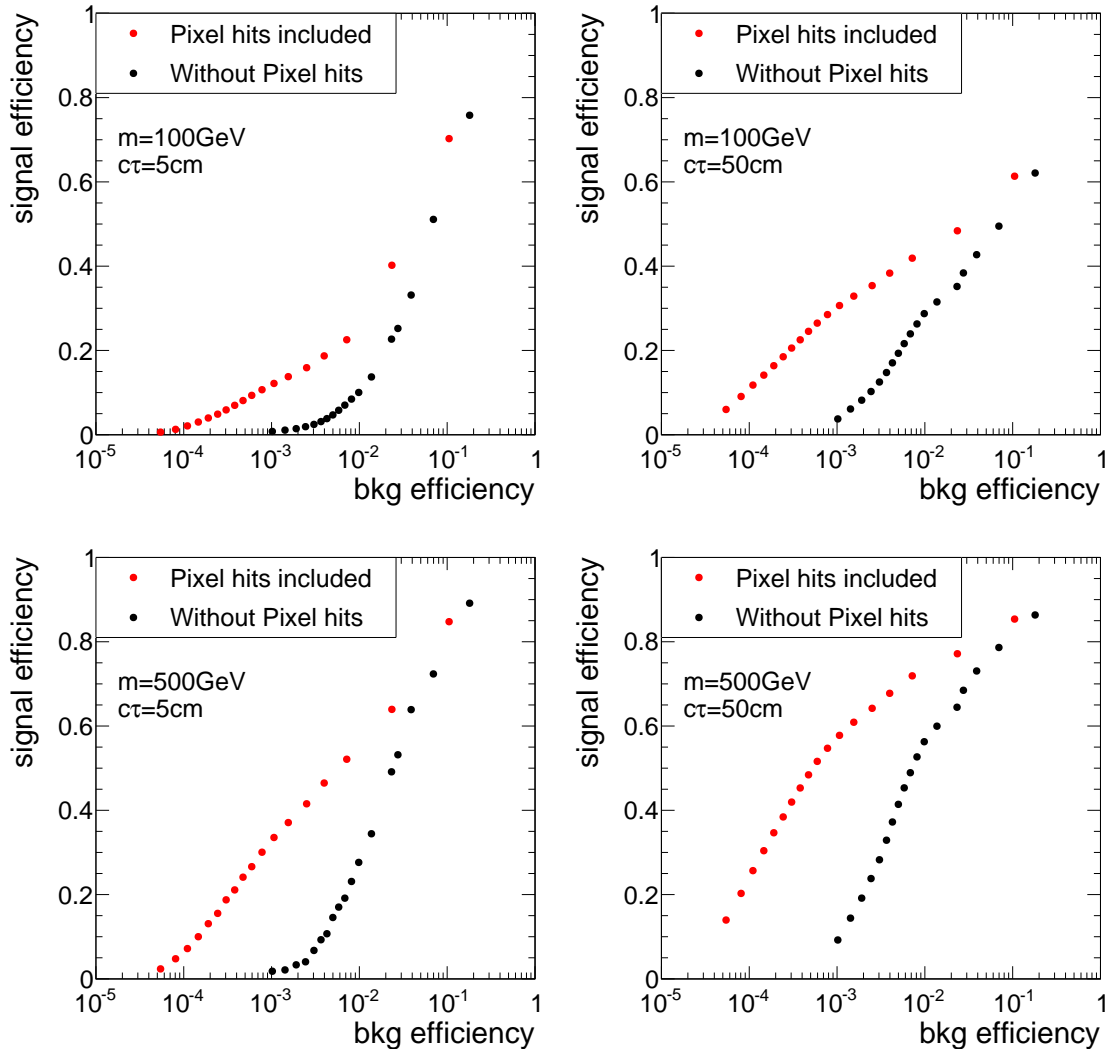


Figure 1.3.10: Signal selection efficiency vs. background selection efficiency with (red) and without (black) pixel information. Each point correspond to one selection cut in I_{as} . The figure is based on a simulated $W + \text{jets}$ sample and a simulated signal sample with chargino-chargino production, both subject to a selection of high-quality tracks (without a selection on N_{hits}) with $p_T > 10 \text{ GeV}$.

501 1.4 Simulated samples

502 In order to design the search and to study background and signal characteristics, this
 503 analysis relies on simulated SM and SUSY datasets. An extensive introduction to the
 504 techniques and tools required for the simulation of SM and beyond SM processes can be
 505 found in Section ??.

506 The following two sections present an overview of the SM (Section 1.4.1) and SUSY
 507 samples (Section 1.4.2) used in this search. All samples are reweighted to match the
 508 measured distribution of primary vertices per event in data. Additionally, event weights
 509 are applied to ensure the same ISR spectrum in simulation as in data.

510 1.4.1 Standard Model background samples

511 To investigate the sources of background, various simulated SM samples are used. Since
 512 this analysis aims at making use of dE/dx , a data format is required that includes tracker
 513 hit information, the so-called RECO format [30]. Unfortunately, not all SM processes are
 514 available in this format making it impossible to compare the total number of events in
 515 simulation and real data. This, however, does not constitute a serious problem since this
 516 analysis will finally use data-based background estimation methods. The simulated SM
 517 datasets can still be used to compare the shapes of important distributions in simulation
 518 and data.¹ Still, the most important SM background sample including $W + \text{jets}$ events is
 519 available. Due to the intrinsic missing energy in $W + \text{jets}$ events it constitutes the major
 520 background to the presented search (see Section 1.6 for further details on the backgrounds).

521

522 In Table 1.4.1 all available SM samples used in this analysis are listed. The matrix-
 523 elements of the $W + \text{jets}$, $t\bar{t} + \text{jets}$ and $Z \rightarrow \ell\bar{\ell} + \text{jets}$ samples are generated using
 524 MADGRAPH 5 [31]. For the QCD sample PYTHIA6 [32] is used for generation. All samples
 525 are then passed to PYTHIA 6 to simulate the hadronisation and the showering. The interac-
 526 tions between the particles and the detector material is simulated using GEANT4 [33,34].

527 Due to the size of the samples (between 5 and 70 TB per sample) a reduction is required
 528 in order to limit the storage space requirements. This is achieved by selecting only events

¹For example, the simulated $Z \rightarrow \nu\bar{\nu} + \text{jets}$ sample that can contribute to the background of this search via fake tracks is not available in RECO format. However, as the shape of important observables of fake tracks is independent of the underlying process, this background can be studied with a simulated $W + \text{jets}$ sample.

529 which contain at least one jet with a minimum transverse momentum of $p_T > 60 \text{ GeV}$.

530 In addition, further simulated samples not containing dE/dx information are used (so-
531 called AOD samples). Because of their much smaller size, these samples are available in
532 full size. They are needed to study the background inclusively in the variable dE/dx .

Table 1.4.1: Available Standard Model background samples containing $\Delta E/\Delta x$ information that are used for background estimation studies.

| Process | Generator | Cross section [pb] | $\mathcal{O}_{\text{cross section calculation}}$ |
|--|------------|----------------------|--|
| $W + \text{jets}$ | MADGRAPH 5 | 36703.2 | NNLO [35] |
| $t\bar{t} + \text{jets}$ | MADGRAPH 5 | 245.8 | NNLO [36] |
| $Z \rightarrow \ell\bar{\ell} + \text{jets}$ ($\ell = e, \mu, \tau$) | MADGRAPH 5 | 3531.9 | NNLO [35] |
| QCD ($50 \text{ GeV} < \hat{p}_T < 1400 \text{ GeV}$) | PYTHIA 6 | 9374794.2 | LO |

533 1.4.2 Signal samples

534 For the investigation of a possible SUSY signal, events containing either chargino pair
535 production $q\bar{q} \rightarrow \tilde{\chi}_1^\pm \tilde{\chi}_1^\mp$ or chargino neutralino production $q\bar{q} \rightarrow \tilde{\chi}_1^\pm \tilde{\chi}_1^0$ are simulated
536 within this thesis. The simulation of the samples is done as described in Section 1.4.1 for
537 the $W + \text{jets}$ sample. However, a special treatment for long-lived particles is required for
538 this analysis. In order to get a correct detector simulation of the energy loss of long-lived
539 particles that decay after the beam pipe, the decay of the chargino cannot be simulated
540 within MADGRAPH or PYTHIA but needs to be simulated within GEANT4. The decay
541 mode of the chargino is also specified within GEANT4 to a neutralino plus pion decay,
542 $\tilde{\chi}_1^\pm \rightarrow \tilde{\chi}_1^0 \pi^\pm$.

543 To reduce the required computing sources, the simulation is only done for a few lifetimes
544 ($c\tau = 1 \text{ cm}, 5 \text{ cm}, 10 \text{ cm}, 50 \text{ cm}, 100 \text{ cm}, 1000 \text{ cm}$ and 10000 cm). The lifetime is hereby
545 not controlled by changing the mass gap between the chargino and the neutralino but is
546 independently specified within GEANT4. In order to scan in a high resolution over the
547 lifetime space, other lifetimes are generated using lifetime reweighting. The weight for
548 each event depends on the individual proper lifetime of the chargino and is given by

$$w = \prod_{i=1}^n \frac{\tau^{\text{gen}}}{\tau^{\text{target}}} \cdot \exp \left[t_i \cdot \left(\frac{1}{\tau^{\text{gen}}} - \frac{1}{\tau^{\text{target}}} \right) \right], \quad (1.4.1)$$

where n is the number of charginos in the event, τ^{gen} is the generated mean lifetime in the particle's rest frame and t_i is the individual proper lifetime of the chargino. The targeted mean lifetime is given by τ^{target} . A derivation of this formula can be found in Appendix B.1. Using this reweighting procedure a good coverage of the lifetime space can be achieved with lifetimes of $1 \text{ cm} \leq c\tau \leq 10^4 \text{ cm}$. Figure 1.4.1 shows the exponential distribution of the individual proper lifetime of the charginos after the reweighting of a simulated sample with $c\tau^{\text{gen}} = 50 \text{ cm}$ to a lifetime of $c\tau^{\text{target}} = 10 \text{ cm}$. It can be seen that the reweighting procedure does indeed reproduce the targeted lifetime of 10 cm.

All samples are generated for different masses of the chargino, but always almost mass-degenerate to the lightest neutralino. The mass gap between chargino and neutralino is set to 150 MeV and, as said before, is hereby disentangled to the chargino lifetime for the simulation of the signal samples. However, since this analysis does not make use of the decay products of the chargino and the mass gap is for all simulated lifetimes of a similar small size, the choice of the mass gap does not affect the signal prediction. Six different masses from 100 GeV to 600 GeV are simulated. This leads to a total number of 42 signal samples. In Table 1.4.2, the cross sections at $\sqrt{s} = 8 \text{ TeV}$ for $\tilde{\chi}_1^\pm \tilde{\chi}_1^\mp$ and $\tilde{\chi}_1^\pm \tilde{\chi}_1^0$ production for wino-like charginos and neutralinos are listed [37, 38]. The cross section does not depend on the lifetime of the chargino.

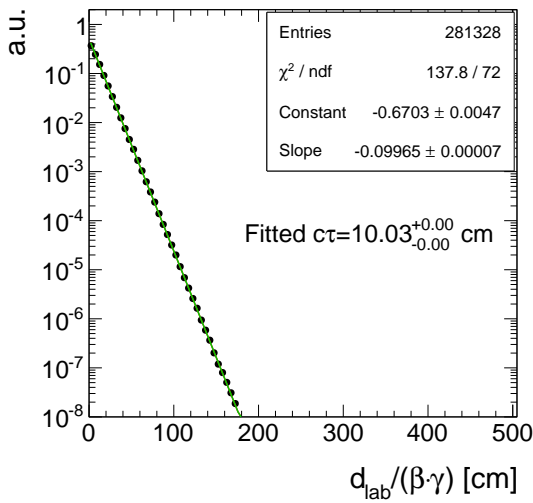


Figure 1.4.1: Normalised distribution of the proper individual lifetime $d_{\text{lab}}/(\beta\gamma)$ of all charginos contained in a signal sample with a generated lifetime of $c\tau^{\text{gen}} = 50 \text{ cm}$ reweighted to a lifetime of $c\tau^{\text{target}} = 10 \text{ cm}$. Fitting an exponential curve $a \cdot \exp\left[\frac{1}{c\tau}ct_i\right]$ yields $c\tau = \text{slope}^{-1} = 10 \text{ cm}$.

Table 1.4.2: Simulated signal mass points with corresponding cross sections at NLO-NLL (NLO: next-to-leading order, NLL: next-to-leading logarithmic) accuracy for wino-like charginos [37, 38].

| $m_{\tilde{\chi}_1^\pm}$ [GeV] | $\sigma_{\tilde{\chi}_1^\pm \tilde{\chi}_1^\mp}$ [pb] | $\sigma_{\tilde{\chi}_1^0 \tilde{\chi}_1^\mp}$ [pb] |
|--------------------------------|---|---|
| 100 | 5.8234 | 11.5132 |
| 200 | 0.37924 | 0.77661 |
| 300 | 0.06751 | 0.14176 |
| 400 | 0.01751 | 0.03758 |
| 500 | 0.00553 | 0.01205 |
| 600 | 0.00196 | 0.00431 |

567 1.5 Event selection

568 1.5.1 Datasets and triggers

569 The analysis is performed on pp -collision data recorded in the year 2012 by the CMS
 570 experiment at a centre-of-mass energy of $\sqrt{s} = 8$ TeV. In total an integrated luminosity
 571 of 19.7 fb^{-1} was recorded in 2012.

572 As outlined in Section 1.2, the detection of chargino tracks is a challenging task already
 573 on trigger level. Direct triggering of events containing chargino-like tracks is not possible
 574 because in 2012 there was no dedicated track trigger available. Furthermore, there is no
 575 intrinsic missing transverse energy in the event if the chargino is not reconstructed as a
 576 PF particle, e.g. when it decays inside the tracker. Therefore, this analysis uses initial
 577 state radiation for the detection of chargino events. If ISR occurs, it is possible to trigger
 578 on a high- p_T jet ($p_T^{1\text{st jet}}$) and missing transverse momentum (\cancel{E}_T).

579 For this purpose, several triggers are utilised in this analysis. An event is selected, if at
 580 least one of the three triggers in Table 1.5.1 fired. The HLTMonocentralPFJet80_PFMET
 581 noMu95_NHEF0p95 and HLTMonocentralPFJet80_PFMETnoMu105_NHEF0p95 trig-
 582 gers both rely on the L1 ETM40 trigger which requires the missing energy to be larger

than 40 GeV. On HLT level, they further require at least one particle-flow jet within the pseudorapidity range of $|\eta| < 2.6$ with $p_T > 80$ GeV and the PF missing transverse momentum (not taking into account the p_T of muons) to be larger than 95 GeV or 105 GeV, respectively. Finally, no more than 95% of the jet energy must be carried by neutral hadrons. The HLTMonoCentralPFJet80_PFMETnoMu95_NHEF0p95 trigger was active during Run A and Run B in 2012 data taking, whereas HLTMonoCentralPF-Jet80_PFMETnoMu105_NHEF0p95 was in place during Run C and Run D in 2012.

The HLT_MET120_HBHENoiseCleaned trigger is based on the L1 trigger ETM36. On HLT level, the trigger requires that the missing energy measured from calorimeter energy deposits is larger than 120 GeV. The HBHENoise-filter reduces background from electronic noise in the HCAL. This trigger was active during the full data taking period in 2012.

The events that were selected by the described triggers are available in the MET datasets listed in Table 1.5.2. Again, because of the size of the datasets (~ 150 TB in total), a reduction of the size is achieved by selecting only events where one of the used triggers fires and that contains at least one jet with a minimum p_T of 50 GeV. The reduction of almost 80% was necessary to make this analysis technically feasible. (FIXME)

1.5.2 Selection of signal candidate events

In order to suppress events originating from Standard Model processes such as QCD-multiparticle events, $W + \text{jets}$, etc., a selection favouring signal-like tracks is applied. The signal candidate selection closely follows the selection required in the disappearing track search [39, 40]. It relies on event-based and track-based variables as described in the following two sections.

Table 1.5.1: \cancel{E}_T and $\cancel{E}_T + \text{jet}$ triggers used in this analysis together with the corresponding recorded integrated luminosity during the time when they were in place.

| Trigger | Integrated luminosity [fb^{-1}] |
|---|--|
| HLTMONOCENTRALPFJET80_PFMETNOMU95_NHEF0P95 | 5.3 |
| HLTMONOCENTRALPFJET80_PFMETNOMU105_NHEF0P95 | 14.4 |
| HLTMET120_HBHENoiseCleaned | 19.7 |

Table 1.5.2: MET data samples used in the search with the contained integrated luminosity.

| Dataset | Integrated luminosity [fb ⁻¹] |
|---------------------------------------|---|
| /MET/Run2012A-22Jan2013-v1/RECO | 0.876 |
| /MET/Run2012B-22Jan2013-v1/RECO | 4.412 |
| /MET/Run2012C-22Jan2013-v1/RECO | 7.055 |
| /METParked/Run2012D-22Jan2013-v1/RECO | 7.354 |

1.5.2.1 Event-based selection

First, a selection on the quality of the primary vertex is applied in order to suppress cosmic events and noise from the beam halo. This selection includes requirements on the position of the vertex with respect to the beam axes and the number of degrees of freedom of the vertex which is strongly correlated to the number of tracks originating from the vertex (see [41] for further details):

- ❖ The vertex must have at least four degrees of freedom: vtx with ≥ 4 d.o.f.
- ❖ The position of the vertex along the beam line must be within 24 cm with respect to the nominal interaction point: $|dz| \leq 24$ cm.
- ❖ The position in the transverse direction must be within 2 cm with respect to the nominal interaction point: $|d\theta| \leq 2$ cm.

616

To maximise the signal acceptance, the trigger related selection cuts are chosen close to the trigger thresholds (see Section 1.5.1). In Fig. 1.5.1, the distributions of E_T and the transverse momentum of the leading jet, $p_T^{1^{\text{st}}\text{jet}}$, are shown for different signal models. The leading jet has to be centrally produced, $|\eta_{1^{\text{st}}\text{jet}}| < 2.4$, and to fulfil the following criteria:

- Charged hadron energy fraction ($\text{CHF}_{1^{\text{st}}\text{jet}}$) > 0.2
- Charged electromagnetic energy fraction ($\text{CEF}_{1^{\text{st}}\text{jet}}$) < 0.5
- Neutral hadron energy fraction ($\text{NHF}_{1^{\text{st}}\text{jet}}$) < 0.7
- Neutral electromagnetic energy fraction ($\text{NEF}_{1^{\text{st}}\text{jet}}$) < 0.7 .

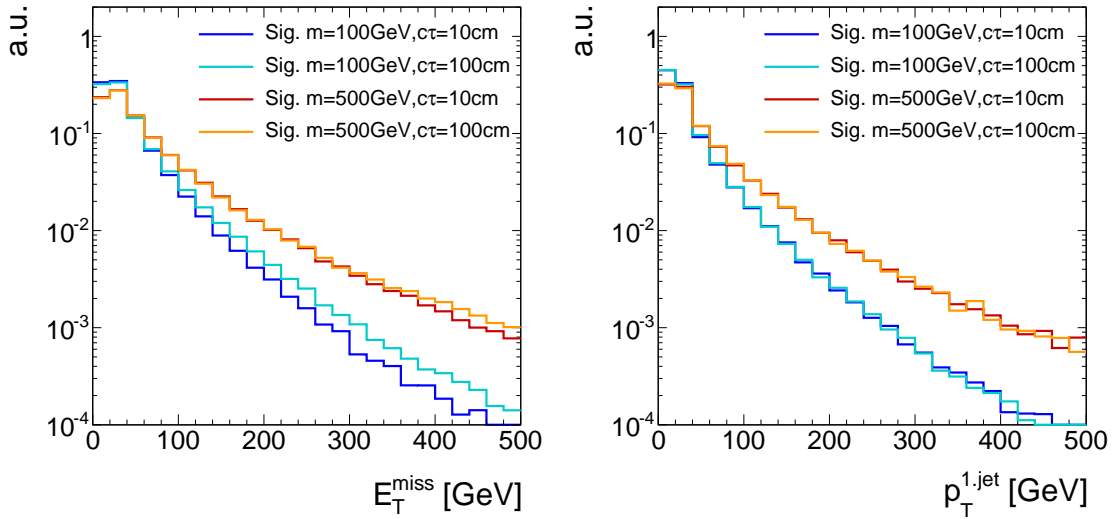


Figure 1.5.1: Normalised distributions of the missing transverse momentum (left) and the transverse momentum of the leading jet (right) for four different signal models.

These additional jet quality criteria ensure that noise from cosmic and beam halo muons and high- p_T photons and electrons is suppressed [42].

The trigger efficiency as a function of \cancel{E}_T and $p_T^{1\text{-jet}}$ was determined within [43] with a single-muon reference sample. The trigger paths become fully efficient for $p_T^{1\text{-jet}} \gtrsim 110\text{ GeV}$ and $\cancel{E}_T \gtrsim 220\text{ GeV}$ [42]. However, it can be seen in Fig. 1.5.1 that for a selection of $\cancel{E}_T > 220\text{ GeV}$ more than 99% of the signal events are rejected.

In order to achieve a reasonable signal acceptance, this search imposes, therefore, a trigger selection closer to the intrinsic trigger thresholds. The trigger selection is as follows:

- ◆ There is at least one jet within $|\eta| < 2.4$ with transverse momentum larger than 110 GeV which fulfils the above mentioned jet noise cleaning criteria: $p_T^{1\text{-jet}} > 110\text{ GeV}$.
- ◆ The missing transverse momentum must be larger than 100 GeV : $\cancel{E}_T > 100\text{ GeV}$

These requirements result in an efficiency of 100% for the trigger requirements on the jet p_T and an efficiency of $\sim 5 - 20\%$ for the trigger requirement on \cancel{E}_T , at the \cancel{E}_T thresholds [42]. Throughout the following sections, these trigger related requirements will be referred to as “trigger selection”.

Because of the huge cross section, QCD-multijet events are frequently produced at the LHC. Due to jet energy mismeasurements, they can also contribute to data samples recorded with MET triggers. Therefore, special requirements are enforced in order to suppress events emerging from QCD-multijet processes. QCD-multijet events can be

characterised by topologies where two jets are almost back-to back. Additionally, in QCD-multijet events the missing energy is usually aligned with one of the leading jets in the event. Figure 1.5.2 shows the maximum $\Delta\phi$ of any of two jets ($p_T > 20 \text{ GeV}$, $|\eta| < 4.5$) and the minimum $\Delta\phi$ between the \cancel{E}_T vector and any of the two leading jets for the SM background and two different signal datasets.

The following two requirements are sufficient to suppress QCD-multijet events efficiently:

- ◆ $\Delta\phi$ between any of two jets (with $p_T > 20 \text{ GeV}$ and $|\eta| < 4.5$) in the event must be smaller than 2.5.
- ◆ $\Delta\phi$ between any of the two leading jets (with $p_T > 20 \text{ GeV}$ and $|\eta| < 4.5$) and the \cancel{E}_T must be larger than 0.5.

1.5.2.2 Candidate track selection

After the reduction of background processes with event-based variables, a track-based selection is carried out. To get an optimised selection for possible chargino tracks several signal candidate track characteristics are exploited.

First, a selection of high-quality tracks is enforced:

- ◆ The track must be classified as “high purity” as defined in [29].

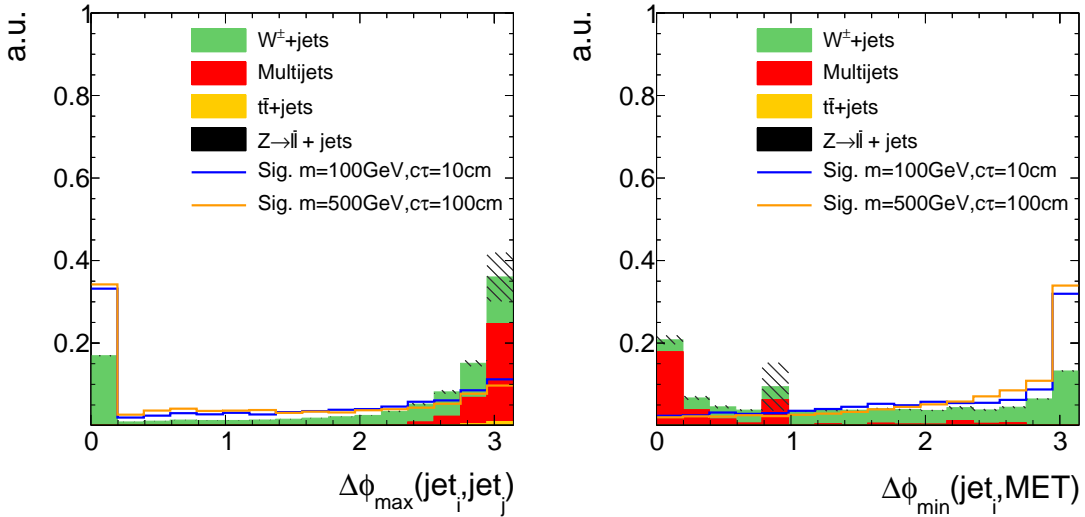


Figure 1.5.2: Maximum $\Delta\phi$ between any of two jets (left) and the minimum $\Delta\phi$ between the \cancel{E}_T vector and any of the two leading jets (right) normalised to unit area after trigger selection. Only jets with $p_T > 20 \text{ GeV}$ and $|\eta| < 4.5$ are considered.

- 662 ❖ The track is required to have no missing middle or inner hits: $N_{\text{miss}}^{\text{middle/inner}} = 0$
 663 ❖ The radial and longitudinal distance of the track to the primary vertex must be
 664 small: $|d0| < 0.02 \text{ cm}$, $|dz| < 0.5 \text{ cm}$.

665 In Figs. 1.5.3 and 1.5.4, the power of the latter two quality selection cuts is shown.

666

667 Furthermore, a first kinematic preselection is applied:

- 668 ❖ Only tracks in the central region are considered : $|\eta| < 2.1$.
 669 ❖ Only tracks with a minimum transverse momentum of 20 GeV are considered:
 670 $p_T > 20 \text{ GeV}$.

671

672 In order to suppress background tracks emerging from SM processes, an electron, muon
 673 and tau veto is applied. This rejects tracks that are close to a reconstructed electron,
 674 muon or tau. Additionally, the candidate track must not be close to a jet ($p_T > 20 \text{ GeV}$
 675 and $|\eta| < 4.5$):

- 676 ❖ The track must not be within a cone of $\Delta R < 0.15$ to a reconstructed standalone,
 677 tracker or global muon with a transverse momentum larger than 10 GeV (see Sec-
 678 tion ?? for details on the different muon definitions).

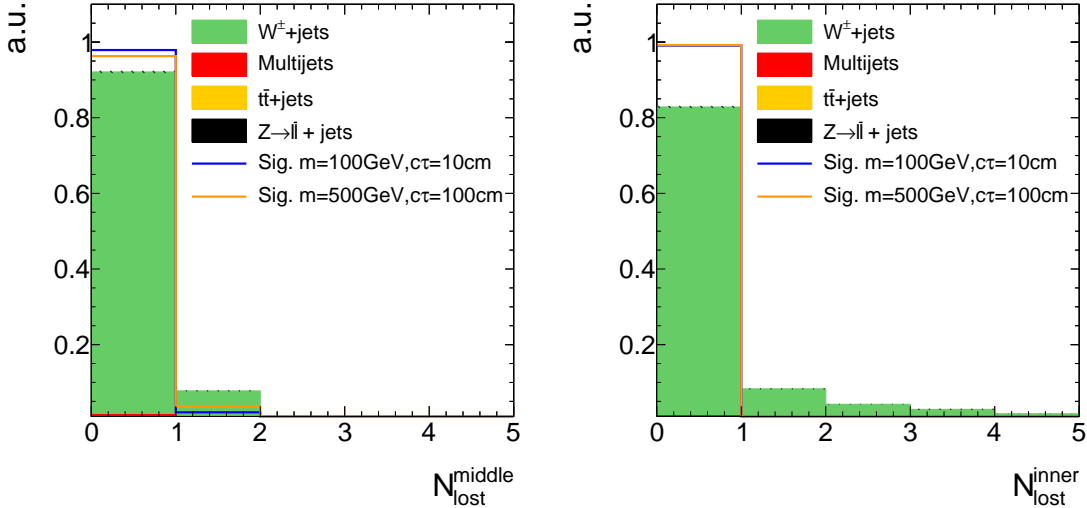


Figure 1.5.3: Normalised number of missing middle (left) and inner (right) hits of background and signal tracks after trigger selection and QCD suppression cuts.

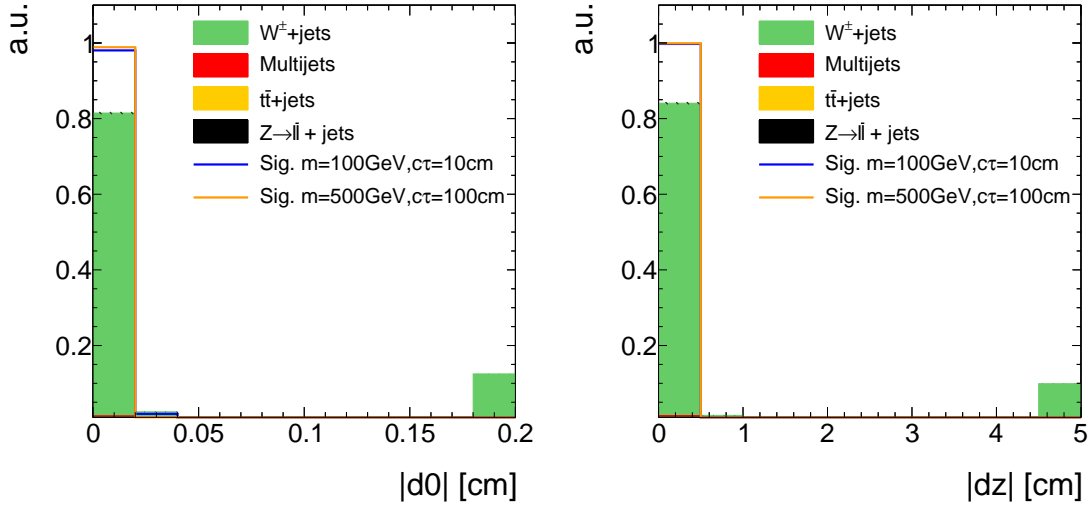


Figure 1.5.4: Absolute value of the radial (left) and longitudinal (right) distance between the track and the primary vertex after trigger selection and QCD-multijet suppression cuts. All events with a candidate track with a radial (longitudinal) distance larger than 0.2 cm (5 cm) are contained in the last bin.

- 679 ❖ The track must not be within a cone of $\Delta R < 0.15$ to a reconstructed electron with a
680 transverse momentum larger than 10 GeV (see Section ?? for details on the electron
681 reconstruction).
- 682 ❖ The track must not be within a cone of $\Delta R < 0.15$ to a reconstructed tau with
683 $p_T > 20$ GeV and $|\eta| < 2.3$ (see Section ?? for details on the tau reconstruction).
684 Some loose isolation requirements are enforced to protect the tau reconstruction
685 from jet contamination.
- 686 ❖ The track must not be within a cone of $\Delta R < 0.5$ to a reconstructed jet ($p_T > 20$ GeV
687 and $|\eta| < 4.5$).

688
689 These lepton and jet veto selection requirements are highly suppressing the background
690 emerging from real lepton/jet production like in $W + \text{jets}$ events. The discrimination power
691 of the lepton and jet vetos is shown in Fig. 1.5.5 where the minimum ΔR between the
692 candidate track and a reconstructed electron, muon, tau or jet is shown.

693
694 Unfortunately, the lepton veto selection cuts are less effective in some of the detector
695 directions. For example, the reconstruction of an electron easily fails in the direction of
696 a dead ECAL cell. This reduces the discrimination power of the electron veto. For this
697 reason, tracks that point towards dead or noisy ECAL cells are rejected. A general list of

dead and noisy ECAL cells is provided centrally by the CMS collaboration. Further dead cells were identified within a study in [39, 40] resulting in a total number of 1234 dead or noisy ECAL channels (which is about 1.6% of all ECAL crystals). These are illustrated in Fig. 1.5.6 showing a map of all ECAL channels not considered in the search.

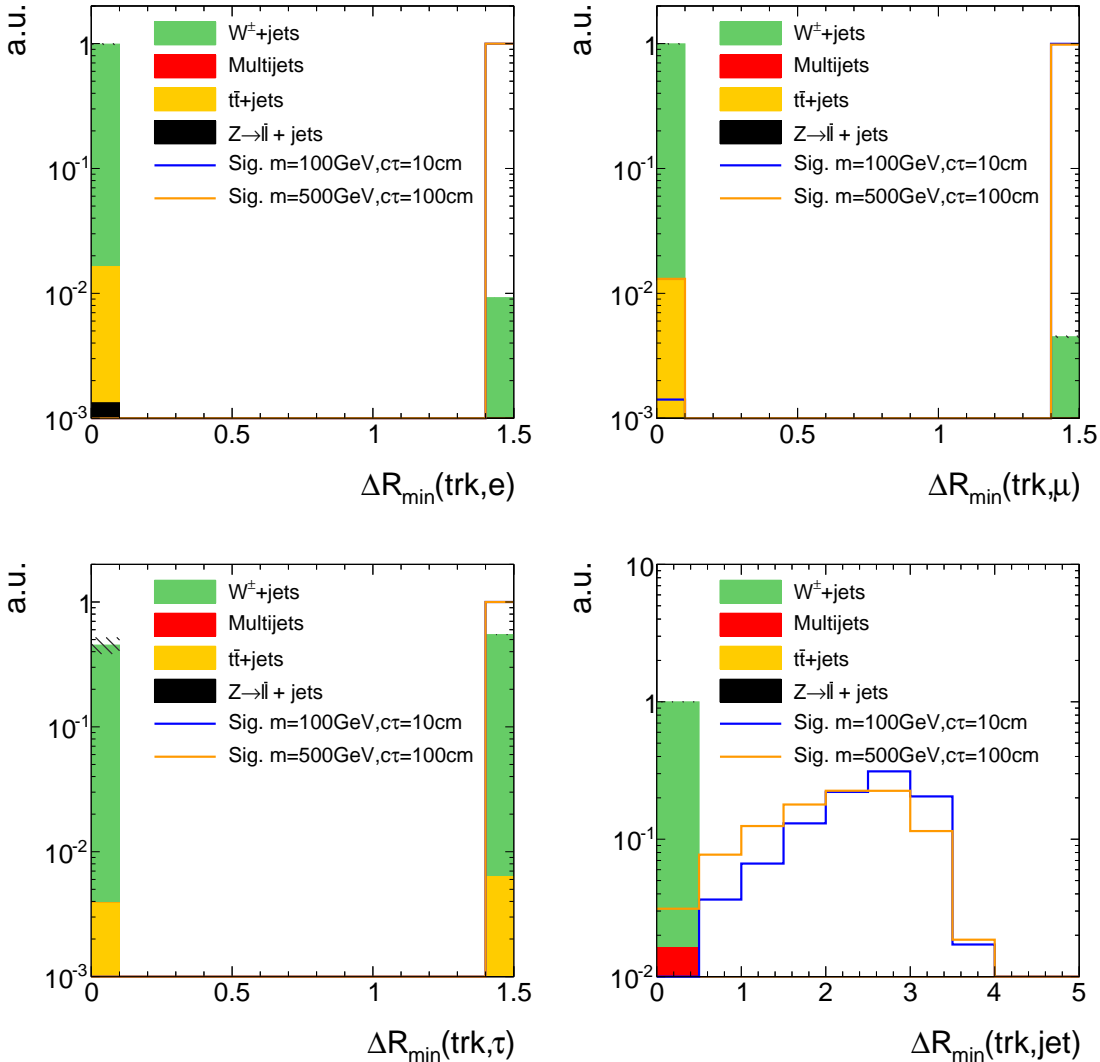


Figure 1.5.5: The minimum ΔR between the candidate track and a reconstructed electron (top left), muon (top right), tau (bottom left) or jet (bottom right) after the event-based selection and the high-quality, kinematic and lepton/jet veto selection of the candidate track selection but without the one shown in the corresponding plot (“N-1 plot”). The last bin contains all events where the candidate track has a ΔR_{\min} larger than 1.5 or 5.0 to the next lepton or jet respectively. Events with no respective lepton or jet are also contained in the last bin.

702 Additionally, tracks that point towards intermodule gaps of ECAL cells or to the ECAL
 703 barrel endcap gap at $1.42 < |\eta| < 1.65$ are rejected. A list of the ECAL intermodule gaps,
 704 which is supplied centrally by CMS, is given in Table 1.5.3.

705 The muon reconstruction is less efficient for muons in detector regions with bad cathode
 706 strip chambers (CSC). These bad chambers are also identified centrally by the CMS col-
 707 laboration and their η and ϕ values are visualised in Fig. 1.5.7. Thus, also tracks pointing
 708 towards these regions within a distance of $\Delta R < 0.25$ are rejected.

709 To summarise, tracks pointing towards detector regions, that are not working properly
 710 or where the lepton reconstruction efficiencies are reduced, are vetoed as follows:

- 711 ❖ Veto tracks within a cone of $\Delta R < 0.05$ to a dead or noisy ECAL cell (visualised in
 712 Fig. 1.5.6).
- 713 ❖ Veto tracks that point towards the direction of the ECAL intermodule gap listed in
 714 Table 1.5.3.
- 715 ❖ Veto tracks that point towards a bad CSC within $\Delta R < 0.25$ (visualised in Fig. 1.5.7).
- 716 ❖ Veto tracks that point towards the region between ECAL barrel and endcap at
 717 $1.42 < |\eta| < 1.65$

718 Finally, two further characteristics of chargino tracks are exploited. As the chargino
 719 is produced in a very clean environment (no further particles around the chargino is
 720 expected), the isolation of the track can discriminate signal against background events.

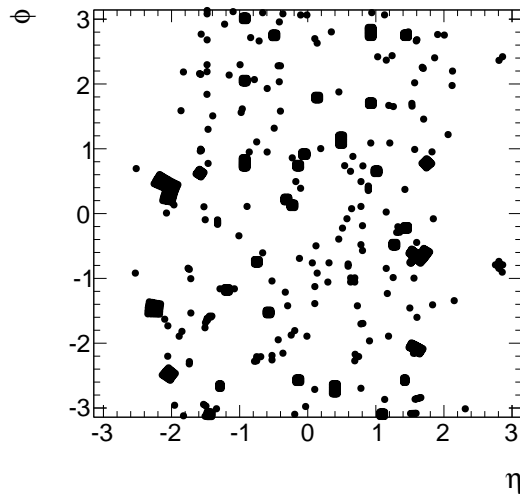


Figure 1.5.6: Visualisation of dead and noisy ECAL cells in the detector's $\phi - \eta$ plane according to [39, 40]. The radius of the dots correspond to $\Delta R = 0.05$.

Furthermore, for charginos decaying inside the tracker there is no associated energy deposition in the calorimeters in the direction of the track. This is a very pronounced characteristics of signal tracks.

The resulting selection cuts are as follows

- ❖ No further substantial track activity is allowed in a cone of $\Delta R < 0.3$ around the

Table 1.5.3: Intermodule ECAL gaps.

| η -ranges |
|-----------------------------------|
| $-1.14018 < \eta < -1.1439$ |
| $-0.791884 < \eta < -0.796051$ |
| $-0.44356 < \eta < -0.447911$ |
| $0.00238527 < \eta < -0.00330793$ |
| $0.446183 < \eta < 0.441949$ |
| $0.793955 < \eta < 0.789963$ |
| $1.14164 < \eta < 1.13812$ |

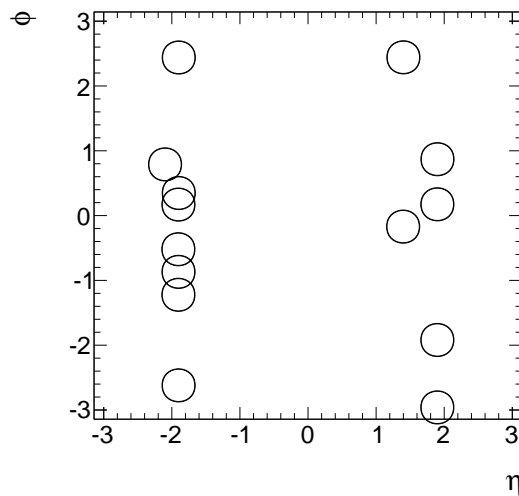


Figure 1.5.7: Visualisation of the excluded region by the bad cathode strip chamber veto in the detector's $\phi - \eta$.

726 candidate track: $\sum_{\Delta R < 0.3} p_T^{\text{trk}} / p_T^{\text{cand}} - 1 < 0.1$ (the subtraction by 1 corresponds to the
 727 contribution of the candidate track itself)

- 728 ♦ No large calorimeter energy deposits (ECAL+HCAL) in a cone of $\Delta R < 0.5$ around
 729 the track: $E_{\text{calo}}^{\Delta R < 0.5} < 5 \text{ GeV}$.

730 The discrimination power of these two variables is shown in Fig. 1.5.8.

731
 732 As emphasised before, this analysis aims at being sensitive especially on shorter lifetimes.
 733 Still, in order to allow for charginos decaying at any position in the tracker, no explicit
 734 selection cut on the number of missing outer hits is required.

735 Events are selected if they at least contain one track fulfilling all candidate track selection
 736 requirements. An overview over the full analysis preselection is given in Table 1.5.4. The
 737 event yields after the selections of each of the categories from Table 1.5.4 are listed in
 738 Table 1.5.5 for the available simulated background samples, some exemplary simulated
 739 signal models and for observed data. The discrepancies between data and simulation after
 740 the full preselection is stemming from two effects. First, not all background samples were
 741 available (e.g. $Z \rightarrow \nu\bar{\nu} + \text{jets}$ sample), leading to a lower prediction in simulation. Second,
 742 due to the specific selection region (lepton+jet veto), a data-simulation discrepancy is
 743 expected. Furthermore, it should be noted, that the resulting 31.9 events in the simulated
 744 $W + \text{jets}$ sample are stemming from only two simulated events due to high event weights.

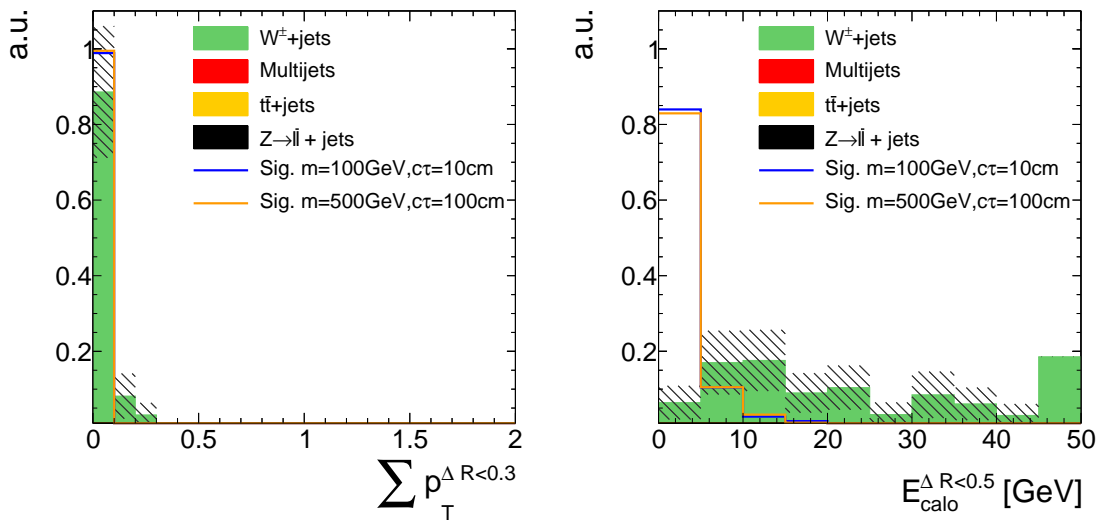


Figure 1.5.8: Track isolation (left) and calorimeter energy deposits (right) of the candidate track after the full previous selection. All events with a track isolation or a calorimeter energy deposit larger than the range shown in the figures are contained in the last bin.

Table 1.5.4: Summary and categorisation of the analysis selection.

| | | |
|---------------------------|---|---|
| Trigger | HLTMonocentralPFJet80_PFMETnoMu95_NHEF0p95 | |
| | HLTMonocentralPFJet80_PFMETnoMu105_NHEF0p95 | |
| | HLT_MET120_HBHENoiseCleaned | |
| Event-based selection | Trigger selection | $p_T^{1\text{st jet}} > 110 \text{ GeV}$ with $ \eta_{1\text{st jet}} < 2.4$, $\text{CHF}_{1\text{st jet}} > 0.2$, $\text{CEF}_{1\text{st jet}} < 0.5$, $\text{NHF}_{1\text{st jet}} < 0.7$, $\text{NEF}_{1\text{st jet}} < 0.7$ $\cancel{E}_T > 100 \text{ GeV}$ |
| | QCD suppression | $\Delta\phi_{\max}(\text{jet}_i, \text{jet}_j) < 2.7$ for all jets with $p_T > 20 \text{ GeV}, \eta < 4.5$ $\Delta\phi_{\max}(\text{jet}_i, \cancel{E}_T) > 0.5$ for two leading jets |
| Candidate track selection | ≥ 1 track that fulfils the following criteria: | |
| | Good quality selection | high-purity as defined in [29] $N_{\text{miss}}^{\text{middle/inner}} = 0$ $ d0 < 0.02 \text{ cm}$ $ dz < 0.5 \text{ cm}$ |
| | Kinematic selection | $ \eta < 2.1$ $p_T > 20 \text{ GeV}$ |
| | Lepton/jet veto | No muon within $\Delta R < 0.15$ No electron within $\Delta R < 0.15$ No tau within $\Delta R < 0.15$ No jet within $\Delta R < 0.5$ No dead/noisy ECAL cell within $\Delta R < 0.05$ Not within an ECAL intermodule gap Not within $1.42 < \eta < 1.65$ Not within $\Delta R < 0.25$ to a bad CSC |
| | Isolation selection | $\sum_{\Delta R < 0.3} p_T^{\text{trk}} / p_T^{\text{cand}} - 1 < 0.1$ $E_{\text{calo}}^{\Delta R < 0.5} < 5 \text{ GeV}$ |

This emphasizes once more the need for data-driven background estimation methods.
 FIXME. Detailed event yield tables can be found in Appendix B.2.

Given the presented signal candidate selection, two variables remain that are highly discriminating: The transverse momentum p_T and the energy release per path length dE/dx of the candidate track. In this analysis, the Asymmetric Smirnov discriminator I_{as} is used to enhance the discriminating power of dE/dx . See Section 1.3.3 for the definition and a detailed explanation of I_{as} .

In Fig. 1.5.9, the distribution of the remaining two variables are shown after the selection of signal candidate events. These variables are used to optimise the sensitivity of the

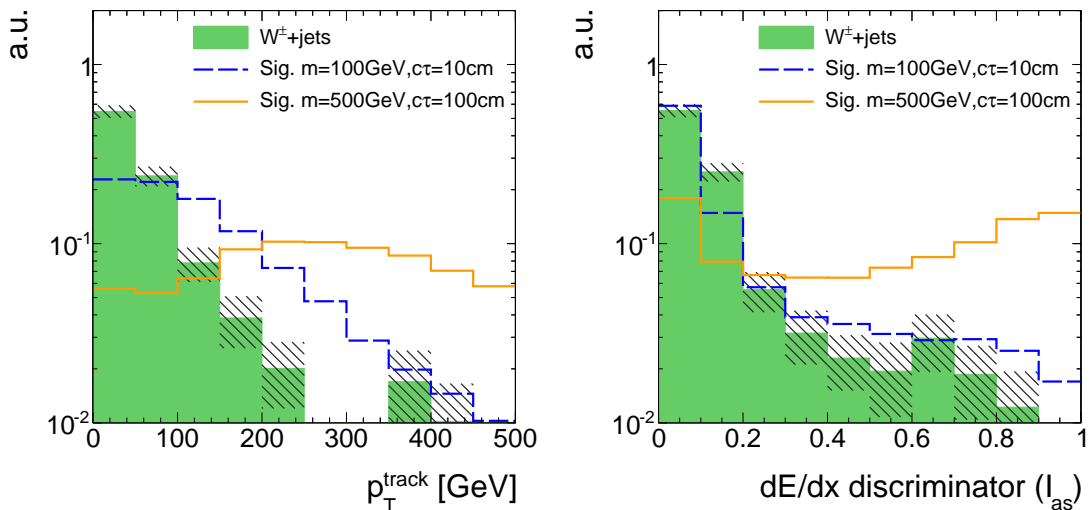


Figure 1.5.9: Candidate track p_T (left) and I_{as} (right) after the full signal candidate selection for signal and $W + \text{jets}$ events. Because of the low statistical precision of the $W + \text{jets}$ sample, the trigger selection is not applied.

search. The optimisation process will be explained in Section 1.7. However, before the optimisation can be accomplished, a characterisation and estimation of the background is needed. This topic will be discussed in the following chapter.

Table 1.5.5: Event yields in simulation and data after the selections of each of the categories from Table 1.5.4

| Selection | Simulated background samples | | | Simulated signal samples | | | Data | | |
|------------------------|------------------------------|--------------------------|--------------------------------|--------------------------|----------------------------------|-----------------------------------|----------------------------------|-----------------------------------|-------------------|
| | $W + \text{jets}$ | $t\bar{t} + \text{jets}$ | $Z \rightarrow \ell\bar{\ell}$ | Multijet | m=100GeV $c\tau=10\text{ cm}$ | m=100GeV $c\tau=100\text{ cm}$ | m=500GeV $c\tau=10\text{ cm}$ | m=500GeV $c\tau=100\text{ cm}$ | MET data |
| After skim | $9.16 \cdot 10^7$ | $1.04 \cdot 10^6$ | $2.21 \cdot 10^7$ | $1.38 \cdot 10^{11}$ | $3.41 \cdot 10^5$ | $3.41 \cdot 10^5$ | $3.46 \cdot 10^2$ | $3.46 \cdot 10^2$ | $1.07 \cdot 10^7$ |
| Event-based selection: | | | | | | | | | |
| Trigger | $4.31 \cdot 10^6$ | $1.15 \cdot 10^5$ | $4.23 \cdot 10^3$ | $4.32 \cdot 10^6$ | $1.55 \cdot 10^4$ | $1.49 \cdot 10^4$ | 46.2 | 46.2 | $1.07 \cdot 10^7$ |
| Trigger selection | $1.89 \cdot 10^6$ | $5.31 \cdot 10^4$ | $6.26 \cdot 10^2$ | $9.63 \cdot 10^5$ | $1.09 \cdot 10^4$ | $9.83 \cdot 10^3$ | 36.3 | 35.7 | $3.94 \cdot 10^6$ |
| QCD suppression | $1.11 \cdot 10^6$ | $6.76 \cdot 10^3$ | $1.32 \cdot 10^2$ | $9.55 \cdot 10^3$ | $7.90 \cdot 10^3$ | $6.98 \cdot 10^3$ | 27.6 | 27.1 | $1.38 \cdot 10^6$ |
| Track-based selection: | | | | | | | | | |
| Good quality selection | $1.07 \cdot 10^6$ | $6.63 \cdot 10^3$ | $1.32 \cdot 10^2$ | $9.55 \cdot 10^3$ | $2.80 \cdot 10^3$ | $5.38 \cdot 10^3$ | 5.07 | 20.0 | $1.30 \cdot 10^6$ |
| Kinematic selection | $8.14 \cdot 10^5$ | $5.63 \cdot 10^3$ | $1.32 \cdot 10^2$ | $5.48 \cdot 10^3$ | $2.54 \cdot 10^3$ | $4.93 \cdot 10^3$ | 4.73 | 18.9 | $9.51 \cdot 10^5$ |
| Lepton/jet veto | $5.02 \cdot 10^2$ | 5.88 | 0 | 0 | $1.99 \cdot 10^3$ | $3.67 \cdot 10^3$ | 3.83 | 15.0 | 616 |
| Isolation selection | 31.9 | 0.67 | 0 | 0 | $1.67 \cdot 10^3$ | $3.04 \cdot 10^3$ | 3.39 | 12.6 | 119 |

758 1.6 Characterisation and estimation of the Standard 759 Model backgrounds

760 After the application of the signal candidate selection, explained in the previous chapter,
761 the background arising from Standard Model processes is dramatically reduced. Only
762 two events in the simulated $W + \text{jets}$ sample remain. One of these originates from an
763 unreconstructed muon, the other one from an unreconstructed electron, both passing the
764 lepton vetoes. This implies, that the electron, muon, and tau vetos cannot reject all leptons
765 because some are not properly reconstructed. Due to the limited size of the simulated
766 $W + \text{jets}$ dataset (15 times smaller than the number of events expected from $W + \text{jets}$
767 processes during 2012 data taking), it is not possible to rely on a full simulation-based
768 estimation of the leptonic background. The underlying mechanism that a lepton can pass
769 the lepton veto and the corresponding methods to estimate the leptonic background will
770 be explained in detail in Section 1.6.2.

771 Furthermore, there is the possibility that a track is reconstructed out of a set of hits
772 that do not originate from only one single particle. Such tracks are called “fake tracks”.
773 Background tracks arising from a combination of unrelated hits will be explained in the fol-
774 lowing Section 1.6.1. It should be noted that the fake background is contributing through
775 all SM processes, not only via $W + \text{jets}$. Still, as the characteristics of fake tracks are
776 independent of the underlying process, this background can also be studied on simulation
777 using $W + \text{jets}$ events only.

778 There is no contribution of jets to the background, because jets are efficiently suppressed
779 by the jet veto and the track isolation requirement of the signal candidate selection (see
780 Table 1.5.4).

781 The reader will recognise, that the importance of the two contributions to the back-
782 ground, the fake and leptonic background, is very different to this search. It will be seen,
783 that the leptonic background is of negligible size.

784 However, both background are estimated in a similar approach. First, an inclusive
785 background estimation (without the use of dE/dx information) is estimated. Afterwards,
786 the efficiency of a dE/dx selection for the fake and leptonic background is determined.

787 Finally, the final signal regions are determined within an optimisation procedure. This
788 optimisation is carried out in the track variables p_T and dE/dx (see Chapter 1.7) to ensure
789 an ideal selection for the search for short and highly ionising tracks.

790 1.6.1 Fake background

791 Fake tracks are reconstructed out of the tracker hits of more than one particle. The rate at
 792 which this false reconstruction occurs is highly restrained by the quality cuts on χ^2 and the
 793 vertex compatibility of the track reconstruction algorithm. Details on the reconstruction
 794 algorithm of tracks at CMS can be found in Section ??.

795 Reconstructed tracks that are fake tracks consist in general only out of a few hits. This
 796 can be seen in Fig. 1.6.1, where the normalised distribution of the number of hits from
 797 fake tracks in simulated $W + \text{jets}$ events is depicted. There are almost no fakes with more
 798 than seven hits. In simulation, fake tracks are defined as tracks that cannot be matched
 799 to a generator-level particle within a distance of $\Delta R < 0.01$.

800 Fakes are efficiently suppressed by the requirements of no missing middle or inner hits
 801 and the compatibility with the primary vertex. Unfortunately, wrongly reconstructed
 802 tracks which pass these criteria, do also easily pass the $E_{\text{calo}}^{\Delta R < 0.5} < 5 \text{ GeV}$ requirement with
 803 high efficiency, as fake tracks cannot be correlated to energy deposits in the calorimeters.

804 Fake tracks are mainly caused by the wrong combination of pileup tracks and electronic
 805 noise. This leads to the fact, that the occurrence of fake tracks across various background
 806 processes is stable, as will be seen later.

807 In this analysis, the estimation of the fake background is split into two parts. First, the
 808 background is determined inclusively in dE/dx . Second, the dE/dx (I_{as}) distribution is
 809 estimated with the help of a fake enriched control region. This second step is needed to

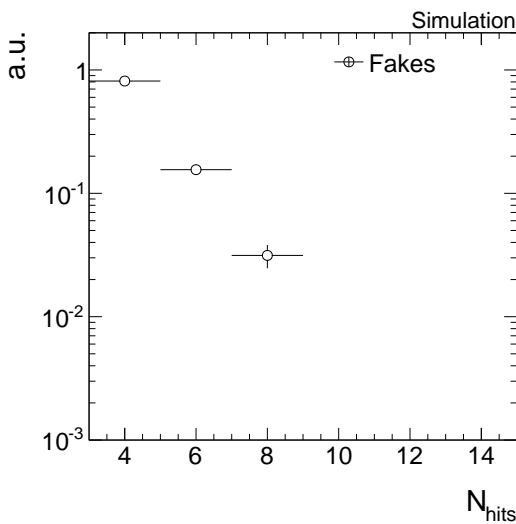


Figure 1.6.1: Normalised distribution of the number of hits for fake tracks in the simulated $W + \text{jets}$ sample. To increase the statistical precision, only the candidate track selection from Table 1.5.4 is applied.

enable an optimisation in dE/dx (see Section 1.7).

1.6.1.1 Inclusive fake background estimation

The inclusive background estimation closely follows the background estimation method done in [39, 40]. It aims at determining the probability of having a fake track in an event that passes the full signal candidate selection (Table 1.5.4) plus a potential additional p_T selection cut that is determined in an optimisation procedure (Section 1.7). This probability will be called the fake rate ρ_{fake} . Within [39, 40], it was checked that the fake rate is constant for different processes. Thus, it is possible to determine ρ_{fake} with the help of one SM process and then generalise it to all SM background processes.

The inclusive fake background is estimated with the help of $Z \rightarrow \mu\bar{\mu}$ and $Z \rightarrow e\bar{e}$ events from data. $Z \rightarrow \ell\bar{\ell}$ events can be selected with high purity by requiring two well reconstructed muons or electrons that are opposite in charge and for which the invariant mass is around the Z -boson mass of ~ 90 GeV. As these events do not contain further leptons from the hard interaction (processes with a further lepton are negligible), any additional track is either a constituent of an ISR jet, a soft particle from pileup events or is a fake. Since the candidate track selection requires a track with a $p_T > 20$ GeV that is no lepton or jet, it suppresses ISR jets and soft tracks from the underlying event. Thus, applying the track-based signal candidate selection on $Z \rightarrow \ell\bar{\ell}$ events selects fake tracks with high purity.

The selection of two well reconstructed muons and electrons is done with the single-muon and single-electron datasets listed in Table 1.6.1. These datasets contain at least one muon or one electron in every event. For the $Z \rightarrow \mu\bar{\mu}$ selection, an event is required to have two muons with $p_T > 25$ GeV and $|\eta| < 2.4$. To suppress background from cosmic muons, the distance from the primary vertex must be less than $|d0| < 0.2$ cm in radial and $|dz| < 0.5$ cm in longitudinal direction. In order to suppress background arising from jets that fake muons, various quality criteria are applied: it is required that there is at least one hit in the muon detector that is considered in the global muon fit, and that at least two measurements are from different muon detector stations. Concerning the track of the muon in the silicon tracker system, at least six hits in the full tracker system of which at least one pixel hit is required. An isolation criterion is applied that requires the sum of transverse momenta of all particle-flow particles in a cone of $\Delta R < 0.4$ around the muon to be less than 12% of the muon p_T . Finally, the muons are required to be opposite in charge and to have an invariant mass between 80 to 100 GeV. The $Z \rightarrow \mu\bar{\mu} +$ fake track selection is summarised in Table 1.6.2.

In order to select $Z \rightarrow e\bar{e}$ events in data, the two electrons are required to have $p_T > 25$ GeV, $|\eta| < 2.5$ and no missing hits in the inner layers of the tracker. Furthermore, the electrons need to pass a conversion veto as described in [44] in order to reduce back-

Table 1.6.1: Datasets used for the determination of the fake rate.

| Dataset | Integrated luminosity [fb ⁻¹] |
|---|---|
| /SingleMu/Run2012A-22Jan2013-v1/AOD | 0.876 |
| /SingleMu/Run2012B-22Jan2013-v1/AOD | 4.405 |
| /SingleMu/Run2012C-22Jan2013-v1/AOD | 7.040 |
| /SingleMu/Run2012D-22Jan2013-v1/AOD | 7.369 |
| <hr/> | |
| /SingleElectron/Run2012A-22Jan2013-v1/AOD | 0.876 |
| /SingleElectron/Run2012B-22Jan2013-v1/AOD | 4.412 |
| /SingleElectron/Run2012C-22Jan2013-v1/AOD | 7.050 |
| /SingleElectron/Run2012D-22Jan2013-v1/AOD | 7.368 |

847 ground arising from photon conversions. An isolation requirement similar to the muon
 848 isolation criterion is applied with an increased threshold of 15%. The electron identifi-
 849 cation is further based on a multivariate technique developed within [45] that exploits
 850 electron characteristics concerning the track quality, the ECAL cluster shapes, and the
 851 combination of the measurements in the tracker and in the ECAL. Again, the two elec-
 852 trons must be opposite in charge and their invariant mass must be between 80 – 100 GeV.
 853 A summary of the $Z \rightarrow e\bar{e}$ + fake track event selection can be found in Table 1.6.3.
 854 In Fig. 1.6.2, the invariant mass distribution M_{inv} is shown for $Z \rightarrow \mu\bar{\mu}$ and $Z \rightarrow e\bar{e}$
 855 events in simulation and data after the event-based selections described above (Tables 1.6.3
 856 and 1.6.2).

857 When applying a $Z \rightarrow \ell\bar{\ell}$ selection plus the candidate track selection, the selected tracks
 858 are mostly fakes. Whether this is indeed the case can be tested on simulated $Z \rightarrow \ell\bar{\ell}$ events.
 859 As can be seen in Fig. 1.6.3, a reasonable purity in fake tracks can be achieved by applying
 860 the candidate track selection on top of the $Z \rightarrow \ell\bar{\ell}$ selection. In simulated $Z \rightarrow \mu\bar{\mu}$ events,
 861 a purity of 88% is achieved, whereas in simulated $Z \rightarrow e\bar{e}$ events a purity of 92% of fake
 862 tracks is achieved.

863 As already mentioned, the fake rate is defined as the probability that an event contains
 864 a fake track that fulfils the candidate track selection. Thus, for the $Z \rightarrow \ell\bar{\ell}$ datasets
 865 it is defined as the number of events passing the full selection described in Table 1.6.2
 866 (Table 1.6.3) divided by the number of events that pass only the event-based selection in

Table 1.6.2: Event selection cuts for the $Z \rightarrow \mu\bar{\mu} + \text{fake}$ control sample to estimate the inclusive fake background.

| | |
|---------------------------|--|
| Event-based selection | Two global muons with $p_T > 25 \text{ GeV}$ $ \eta < 2.4$ $\sum_{\Delta R < 0.4} p_T^{\text{PF particle}} / p_T(\mu) < 0.12$ $\left. \frac{\chi^2}{ndof} \right _{\text{global track}} < 10$ $ d0 < 0.2 \text{ cm}$ $ dz < 0.5 \text{ cm}$ $\geq 1 \text{ hit in the muon detector considered in global fit}$ $\geq 2 \text{ hits in different muon stations}$ $\geq 1 \text{ hit in the pixel detector}$ $\geq 6 \text{ hits in the tracker system}$ |
| | Muons opposite in charge $80 \text{ GeV} < M_{\text{inv}}(\mu_1, \mu_2) < 100 \text{ GeV}$ |
| Candidate track selection | Good quality selection Kinematic selection Lepton/jet veto Isolation selection |

867 Table 1.6.2 (Table 1.6.3)

$$\rho_{\text{fake}} = \frac{N_{Z \rightarrow ll}^{\text{cand trk selection}}}{N_{Z \rightarrow ll}}$$

868 Fake rates are determined independently for the $Z \rightarrow \mu\bar{\mu} + \text{fake}$ and $Z \rightarrow e\bar{e} + \text{fake}$ event
869 selection and then averaged to obtain the final fake rate. In Table 1.6.4 the results of
870 $N_{Z \rightarrow ll}^{\text{cand trk selection}}$, $N_{Z \rightarrow ll}$ and the resulting fake rate for the candidate track selection given
871 in Table 1.5.4 are presented. The averaged fake rate is thus $(6.86 \pm 0.25) \cdot 10^{-5}$. This is
872 not the final result as the optimisation in p_T will add an additional p_T selection cut to the
873 candidate track selection.

874 As mentioned before, it was checked within [39, 40] that the fake rate is constant for
875 different Standard Model processes. This is shown in Fig. 1.6.4 where the fake rate is

Table 1.6.3: Event selection cuts for the $Z \rightarrow e\bar{e}$ + fake control sample to estimate the inclusive fake background.

| | | |
|---------------------------|------------------------------|--|
| Event-based selection | Two Electrons with | $p_T > 25 \text{ GeV}$ |
| | | $ \eta < 2.5$ |
| | | $\sum_{\Delta R < 0.4} p_T^{\text{PF particle}} / p_T(e) < 0.15$ |
| | | pass conversion veto [44] |
| | | no missing inner tracker hits |
| | | good MVA electron as defined in [45] |
| | Electrons opposite in charge | |
| | | $80 \text{ GeV} < M_{\text{inv}}(e_1, e_2) < 100 \text{ GeV}$ |
| Candidate track selection | Good quality selection | |
| | Kinematic selection | |
| | Lepton/jet veto | |
| | Isolation selection | |

Table 1.6.4: Results of $N_{Z \rightarrow ll}^{\text{cand trk selection}}$, $N_{Z \rightarrow ll}$ and ρ_{fake} for the candidate track selection given in Table 1.5.4.

| Channel | $N_{Z \rightarrow ll}^{\text{cand trk selection}}$ | $N_{Z \rightarrow ll}$ | ρ_{fake} |
|------------------------------|--|------------------------|---------------------------------|
| $Z \rightarrow \mu\bar{\mu}$ | 403 | $6.17 \cdot 10^6$ | $(6.53 \pm 0.33) \cdot 10^{-5}$ |
| $Z \rightarrow e\bar{e}$ | 369 | $5.08 \cdot 10^6$ | $(7.26 \pm 0.38) \cdot 10^{-5}$ |

depicted for the most important SM processes. Since the fake rate is constant for different SM processes, the fake rate determined on the $Z \rightarrow \ell\bar{\ell}$ dataset can be generalised for all SM background possibly contributing to this search. Thus, the inclusive fake background can be estimated by multiplying the fake rate with the number of events selected from the MET dataset (Table 1.5.2) by applying the event-based signal candidate requirements

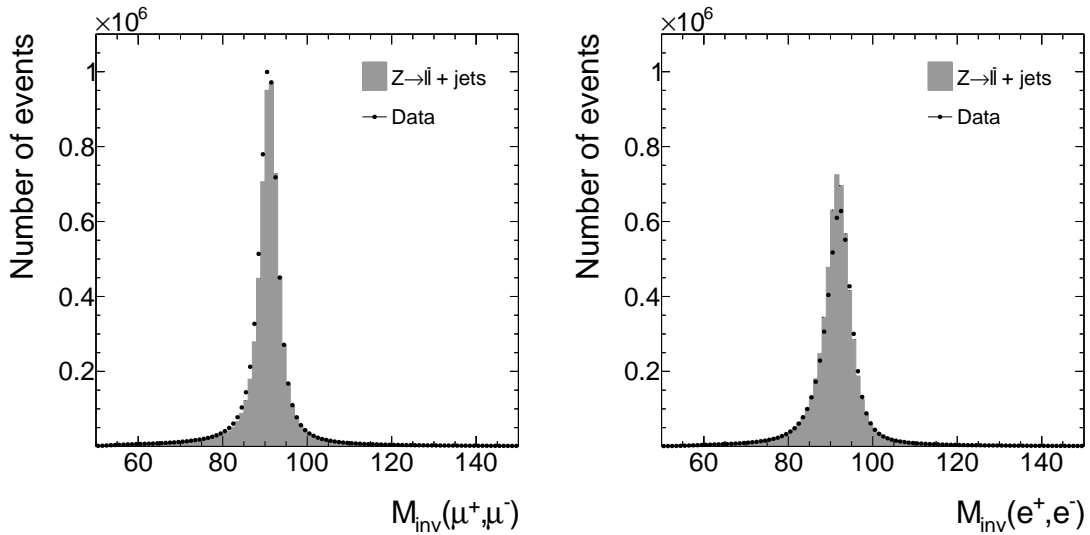


Figure 1.6.2: The invariant mass of the two selected muons (left) and the two selected electrons (right) after the event-based selection from Tables 1.6.3 and 1.6.2, respectively.

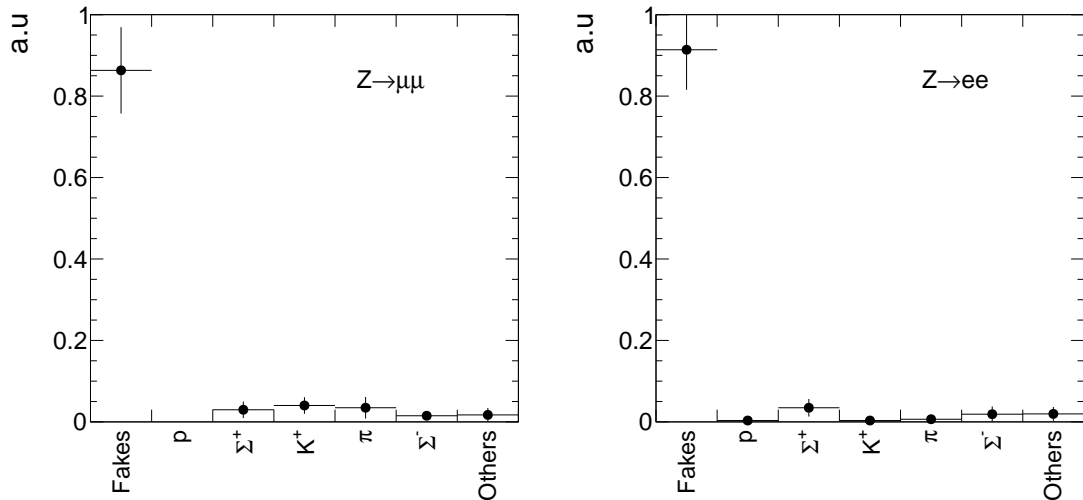


Figure 1.6.3: Corresponding generator-level particles of all tracks within $Z \rightarrow \ell\bar{\ell} + \text{fake}$ that were selected according to the candidate track selection. The full selection for tracks in $Z \rightarrow \mu\bar{\mu}$ events (left) is given in Table 1.6.2. The full selection for tracks in $Z \rightarrow e\bar{e}$ events (right) is given in Table 1.6.3. “Fake” means that no corresponding generator-level particle is found.

⁸⁸¹ from Table 1.5.4

$$N_{\text{bkg}}^{\text{fake, inclusive in } I_{\text{as}}} = \rho_{\text{fake}} \cdot N_{\text{event-based selection}}^{\text{MET}}$$

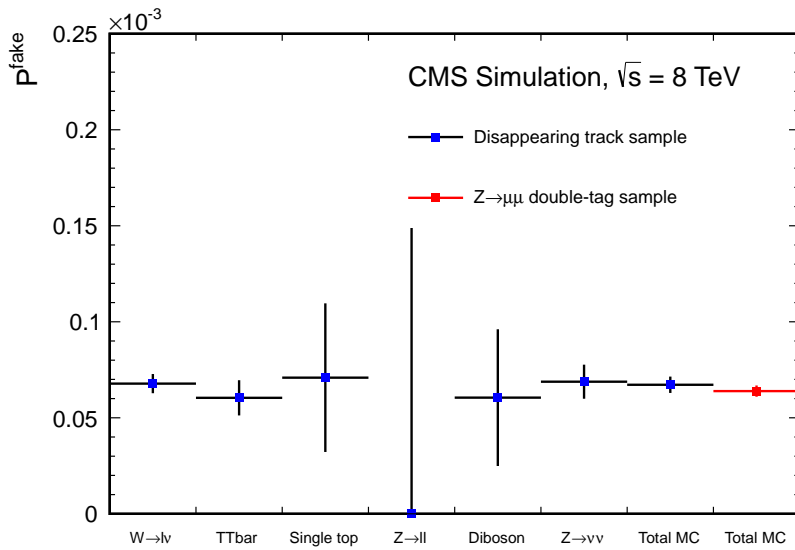


Figure 1.6.4: Fake track rate estimated in [39, 40] for tracks with four hits. Taken from [40]

Given the number of events after the event-based selection of $N_{\text{event-based selection}}^{\text{MET}} = 1.38 \cdot 10^6$ and the fake rate cited above, the inclusive fake background can be estimated to 94.7 ± 3.4 for the candidate track selection.

It should be noted again that the inclusive fake background estimation will be only inclusive in I_{as} not in p_T . That means that after the definition of the signal region, $N_{\text{bkg}}^{\text{fake, inclusive in } I_{\text{as}}}$ is determined with the additional optimal p_T selection.

Possible differences between the fake rate in $Z \rightarrow \ell\bar{\ell}$ events and other SM processes are estimated on simulated events and taken into account as a systematic uncertainty (see Section 1.6.4.1).

1.6.1.2 dE/dx shape of fake background

The information about the energy release per path length for fake tracks should not be taken from simulated samples as the simulation of dE/dx is not reliable (cf. Fig. 1.3.8). Within this analysis the Asymmetric Smirnov discriminator I_{as} is used to discriminate signal against background with respect to dE/dx (see Section 1.3.3). In order to estimate the I_{as} shape of fake tracks, a control region $\text{CR}_{I_{\text{as}}}^{\text{fake}}$ is defined that is enriched with fakes and shows the same I_{as} distribution as fake tracks in the signal region.

To enrich fake tracks, it is possible to invert the selection cuts on the number of missing middle and inner hits, i.e. requiring at least one missing inner or middle hit ($N_{\text{miss}}^{\text{inner}} + N_{\text{miss}}^{\text{middle}} > 0$). Figure 1.6.5 shows the distribution of the number of missing inner plus missing middle hits for fake and leptonic tracks in simulated $W + \text{jets}$ events. It

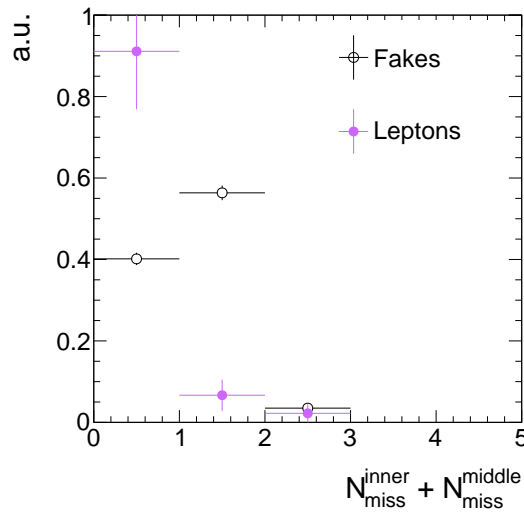


Figure 1.6.5: Normalised number of missing inner plus missing middle hits for fake and leptonic tracks for the full candidate track selection with the selection requirements on $N_{\text{miss}}^{\text{inner}}$ and $N_{\text{miss}}^{\text{middle}}$ removed. Trigger selection and QCD suppression cuts were removed to enhance the statistical precision.

902 can be seen that this selection is enriched by fakes. The resulting purity of fakes in $\text{CR}_{I_{\text{as}}}^{\text{fake}}$
 903 is about 98% (see Fig. 1.6.6).

904 Additionally, it must be checked whether the I_{as} shape in $\text{CR}_{I_{\text{as}}}^{\text{fake}}$ is representative for
 905 the I_{as} shape in the signal region. As the exact definition of the signal region will be
 906 addressed during optimisation, this test is done for various p_{T} selection cuts.

907 The comparison of the I_{as} shape of fake tracks can only be done with simulated events.
 908 Thus, simulated $W+\text{jets}$ events are used to select fake tracks in both regions. A comparison
 909 of the shape for the candidate track selection and the $\text{CR}_{I_{\text{as}}}^{\text{fake}}$ is shown in Fig. 1.6.6.

910 The I_{as} shape is almost identical in the signal and in the control region which makes the
 911 definition of the control region perfectly suited for estimating the I_{as} shape from $\text{CR}_{I_{\text{as}}}^{\text{fake}}$ in
 912 data. The remaining shape differences are taken into account as a systematic uncertainty
 913 (discussed in Section 1.6.4.2).

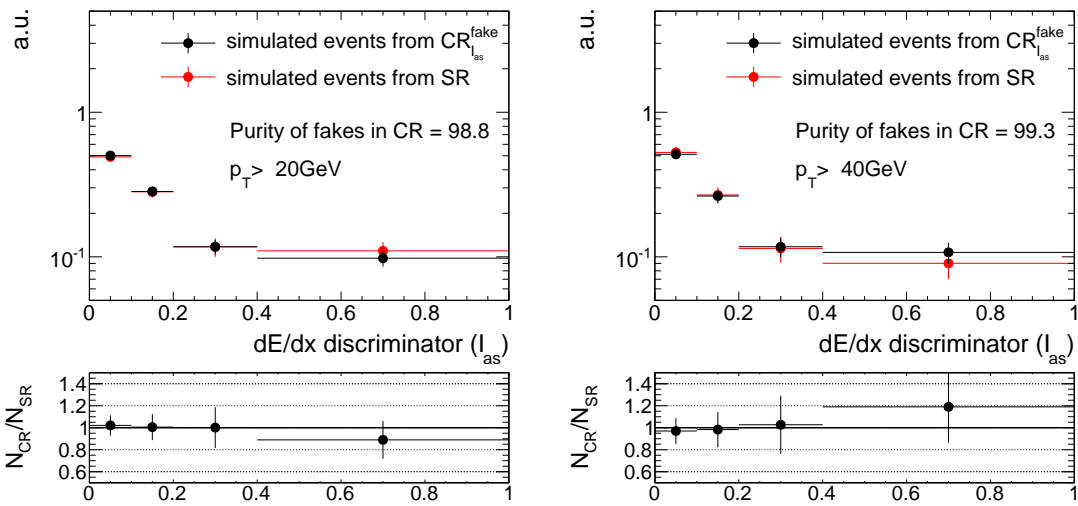


Figure 1.6.6: Comparison of the I_{as} shape between $\text{CR}_{I_{as}}^{\text{fake}}$ and the signal region for two different track p_T selections of $p_T > 20\text{ GeV}$ (left) and $p_T > 40\text{ GeV}$ (right). To enhance the statistical precision only the track-based selection is applied.

914 1.6.2 Leptonic background

915 The leptonic background of the here presented search is caused by non-reconstructed
 916 leptons that circumvent the lepton veto selection. However, at least non-reconstructed
 917 electrons or taus should in principle deposit enough energy in the calorimeters such that
 918 they can still be vetoed by the calorimeter isolation requirement $E_{\text{calo}}^{\Delta R < 0.5} < 5\text{ GeV}$. As
 919 muons don't deposit much energy in the calorimeters, this reasoning does not apply to
 920 them. All of the three lepton types behave like MIPs. Thus, they loose much less energy
 921 than hypothetical new heavy particles and can therefore be further discriminated by their
 922 ionisation loss in the tracker system.

923 In the following, the sources of the three different leptonic backgrounds are characterised.

924 Electrons

925 To reject unreconstructed electrons, all tracks pointing to a dead or noisy ECAL cell,
 926 to an ECAL intermodule gap, or to the region between ECAL barrel and endcap at
 927 $1.42 < |\eta| < 1.65$ are vetoed, as described in Section 1.5.2. By this selection, almost all
 928 electrons are efficiently rejected.

929 However, there is still the possibility that an electron fails reconstruction and pass the
 930 signal candidate selection. This can happen either, if an electron do bremsstrahlung and
 931 the direction of the electron is significantly changed. Thus, the energy deposits in the
 932 ECAL can possibly not be matched to the original electron. Alternatively, there is also

the possibility that an electron track is pointing towards a non-working ECAL cell, that is not included in the dead and noisy ECAL cell veto.

This possibility can be seen in the single event in the $W + \text{jets}$ sample that pass the full signal candidate selection and where the candidate track can be matched to a generator-level electron. This event is visualised in Fig. 1.6.7 (left). The neutrino, only weakly interacting does not show any signature in the detector, whereas the electron ($p_T \simeq 90 \text{ GeV}$) leaves a track with $p_T \simeq 70 \text{ GeV}$ in the tracker. Only little ECAL energy deposits in the direction of the electron are visible. This is caused by the fact that one of the corresponding ECAL crystal is not working properly and thus no energy deposition can be recorded (cf. Fig. 1.6.7 (right)). An ISR jet ($p_T \simeq 230 \text{ GeV}$) causes the \cancel{E}_T in the event.

943 Taus

Taus that decay hadronically are contributing to the leptonic background through the decay of a tau lepton to one charged pion $\tau \rightarrow \pi^\pm \nu_\tau$. Other hadronic decay modes of the tau lepton are suppressed by the track isolation criterion. Taus can fail reconstruction if they only deposit little energy in the HCAL or ECAL. This is usually due to a low energetic pion from the tau decay. Unreconstructed taus can therefore also easily bypass the calorimeter isolation criterion. Because of nuclear interactions in the tracker, pions often result in short reconstructed tracks that can easily be highly mismeasured in p_T . Thus, taus can contribute to the background even if imposing a tight selection in the transverse momentum.

Such an event is shown in Fig. 1.6.8. The transverse momentum of the generator-level pion is only $p_T \sim 10 \text{ GeV}$, but because the reconstructed track is very short, it leads to a high mismeasurement of the track p_T of $\sim 40 \text{ GeV}$. The shortness of the track is caused by nuclear interactions of the pion. As no corresponding ECAL or HCAL energy deposits are measured, the reconstruction of the pion fails. The ISR jet causes the \cancel{E}_T in the event.

958 Muons

Muons can fail reconstruction if they point towards a bad cathode strip chamber. This is taken into account in the candidate track selection. However, some of the muons still fail reconstruction if they fall within the gap between stations 0 and 1 of the drift tube system at $|\eta| = 0.25$. The muon reconstruction efficiency drops from around 99% to a value of around 94%, as shown in [39,40]. This possibility is illustrated in a simulated event shown in Fig. 1.6.9. There, the muon is pointing to the η -region between stations 0 and 1 of the DT system. No signal in the muon chambers is visible. Therefore the muon could not be reconstructed.

In [39,40] events are rejected if the track is pointing in a region of $0.15 < |\eta| < 0.35$. In this search, this cut was omitted to maximise signal acceptance. Due to the additional

selection in I_{as} , muons can be efficiently suppressed. E.g. in the event shown in Fig. 1.6.9, the muon has an I_{as} value of about 0.007.

971

972 As for the fakes, the leptonic background estimation is splitted into two parts. First, the
973 estimation of the inclusive background without I_{as} information. Second, the estimation of
974 the I_{as} shape for all three leptonic background sources. To have the possibility to make
975 an optimisation in the two main discriminating variables p_{T} and I_{as} , the background
976 estimation methods are designed to work for all different p_{T} and I_{as} selection cuts.

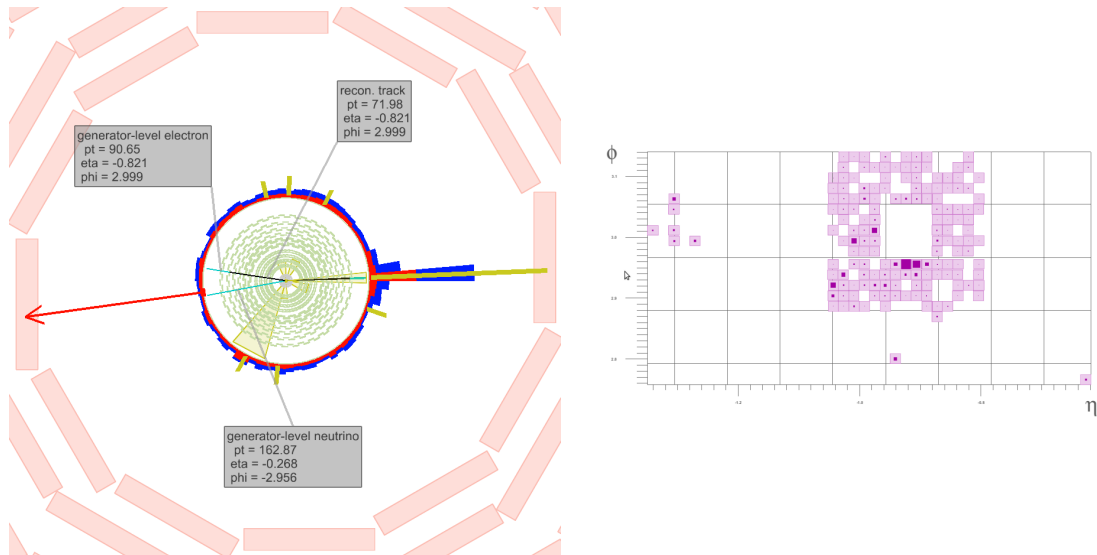


Figure 1.6.7: Left: Visualisation of a $W \rightarrow e\nu_e$ event contributing to the SM background. In light blue, generator-level particles including e and ν_e of the W -boson decay are shown. Black lines represent reconstructed tracks and the red arrow indicates the missing transverse energy in the event. Right: Detailed view of the corresponding towers in the direction of the e track.

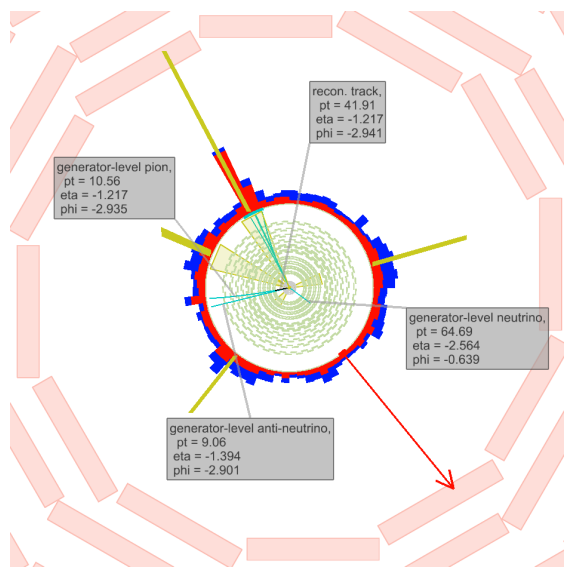


Figure 1.6.8: Visualisation of a $W^+ \rightarrow \tau^+\nu_\tau \rightarrow \pi^+\bar{\nu}_\tau\nu_\tau$ event contributing to the SM background. In light blue, the generator-level particles including π^+ , $\bar{\nu}_\tau$ and ν_τ are shown. The black line represents the reconstructed pion track and the red arrow indicates the missing transverse energy in the event.

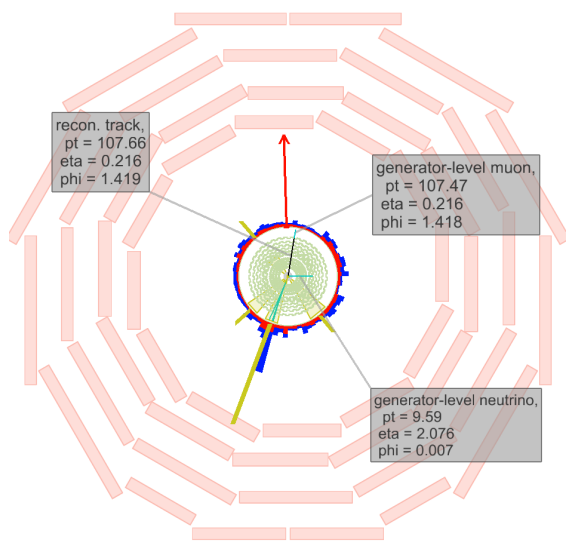


Figure 1.6.9: Visualisation of an $W \rightarrow \mu\nu_\mu$ event contributing to the SM background. In light blue, the generator-level particles including μ and ν_μ of the W decay are shown.

977 **1.6.2.1 Inclusive leptonic background estimation**

978 The inclusive (without dE/dx information) lepton background estimation method is sim-
979 ilar to the background estimation method used in [39, 40].

980 In order to estimate the number of events in the signal region originating from leptons
981 that pass the lepton veto, information from simulated events is used. With the help of
982 simulated $W + \text{jets}$ events, the ratio $\rho_{\text{MC}}^{\text{lep}_i}$ between the number of events in the signal region
983 with the selected track matched to a generator-level lepton $N_{\text{SR}}^{\text{trk matched to lepton}_i}$ and the
984 number of events in a control region $N_{\text{CR}}^{\text{lepton}_i \text{ veto inverted}}$ with a inverted lepton veto is
985 determined. For muons, this lead to the following expression

$$\rho_{\text{MC}}^\mu = \frac{N_{\text{SR},\text{MC}}^{\text{trk matched to } \mu}}{N_{\text{CR},\text{MC}}^{\mu \text{ veto inverted}}}.$$

986 Since for electrons and taus the reconstruction efficiency is highly correlated with the
987 $E_{\text{calo}}^{\Delta R < 0.5}$ selection requirement, the $E_{\text{calo}}^{\Delta R < 0.5}$ requirement is additionally removed in the
988 control regions for these two lepton types

$$\rho_{\text{MC}}^{e,\tau} = \frac{N_{\text{SR},\text{MC}}^{\text{trk matched to } e,\tau}}{N_{\text{CR},\text{MC}}^{e,\tau \text{ veto inverted}, \cancel{E_{\text{calo}}^{\Delta R < 0.5} < 5 \text{ GeV}}}^{\mu \text{ veto inverted}}}.$$

989 In order to estimate the inclusive background for all three lepton types, the scale factor
990 $\rho_{\text{MC}}^{\text{lep}_i}$ is applied to the number of events in the lepton veto inverted control region measured
991 in data. Also in data the control region for electrons and taus is defined with the $E_{\text{calo}}^{\Delta R < 0.5}$
992 requirement removed. Thus, the inclusive number of predicted background events can be
993 estimated with

$$N_{\text{predicted}}^{\mu, \text{ inclusive in I}_{\text{as}}} = \rho_{\text{MC}}^\mu \cdot N_{\text{CR,data}}^{\mu \text{ veto inverted}}.$$

994 for muons, and

$$N_{\text{predicted}}^{e,\tau, \text{ inclusive in I}_{\text{as}}} = \rho_{\text{MC}}^{e,\tau} \cdot N_{\text{CR,data}}^{e,\tau \text{ veto inverted}, \cancel{E_{\text{calo}}^{\Delta R < 0.5} < 5 \text{ GeV}}}.$$

995 for electrons and taus.

996 This method relies on the simulation of the lepton reconstruction efficiencies which is
997 known to be reasonably accurate [46–48]. For electrons and taus the simulation of the
998 calorimeter isolation is utilised as well. Possible discrepancies between simulation and
999 data are taken into account as a systematic uncertainty via a comparison of the lepton
1000 reconstruction efficiencies in data and simulation in $Z \rightarrow \ell\bar{\ell}$ events (see Section 1.6.4.3).

1001 To reduce the statistical uncertainty, the scale factor is calculated without applying the
1002 QCD suppression cuts. After the signal candidate selection described in Section 1.5.2,
1003 only one event remains in the simulated $W + \text{jets}$ sample where the candidate track can be

matched to an electron. There are five events with a track candidate that can be matched to a muon, and no selected events have tracks that can be matched to a pion from a tau decay. The statistical uncertainties are calculated as the 68% upper and lower limits on the inclusive background with the Neyman procedure [22, 49]. Table 1.6.5 gives the result for the prediction of the inclusive leptonic background for the signal candidate selection from Section 1.5.2.

Table 1.6.5: Scale factor $\rho_{\text{MC}}^{\text{lep}_i}$, number of events in the data control region $N_{\text{CR,data}}$ and the resulting inclusive estimation $N_{\text{predicted}}$ after the candidate track selection.

| | $\rho_{\text{MC}}^{\text{lep}_i}$ | $N_{\text{veto inverted}}$ | $N_{\text{predicted}}^{\text{inclusive in } I_{\text{as}}}$ |
|-----------|--------------------------------------|----------------------------|---|
| electrons | $1.25^{+1.70}_{-0.77} \cdot 10^{-4}$ | 60067 | $7.49^{+10.19}_{-4.63}$ |
| muons | $2.17^{+1.65}_{-0.93} \cdot 10^{-4}$ | 76664 | $16.64^{+12.64}_{-7.12}$ |
| taus | $< 2.13 \cdot 10^{-2}$ | 445 | < 9.46 |

1.6.2.2 dE/dx shape of leptonic background

In order to get information about the I_{as} (see Section 1.3.3) shape in the signal region of electrons, muons and taus, a control region should be found where the shape of the observable is at least similar to that in the signal region. The most natural control region, being the lepton veto inverted control region, cannot be used because the variable I_{as} differs between the signal and the control region, as can be seen in Fig. 1.6.10. The discrepancies reach factors up to an order of magnitude.

As this control region is not suitable, it is decided to use the I_{as} information from simulation. This introduces a large bias since dE/dx (and therefore I_{as}) is not simulated well. However, the corresponding bias is still smaller than the differences of the I_{as} shape between the signal and a control region: compare Fig. 1.6.10 and Fig. 1.6.11.

In order to take into account the bias when using I_{as} from simulation, a systematic uncertainty is estimated that addresses simulation-data differences of the I_{as} distributions. This systematic uncertainty is discussed in Section 1.6.4.4.

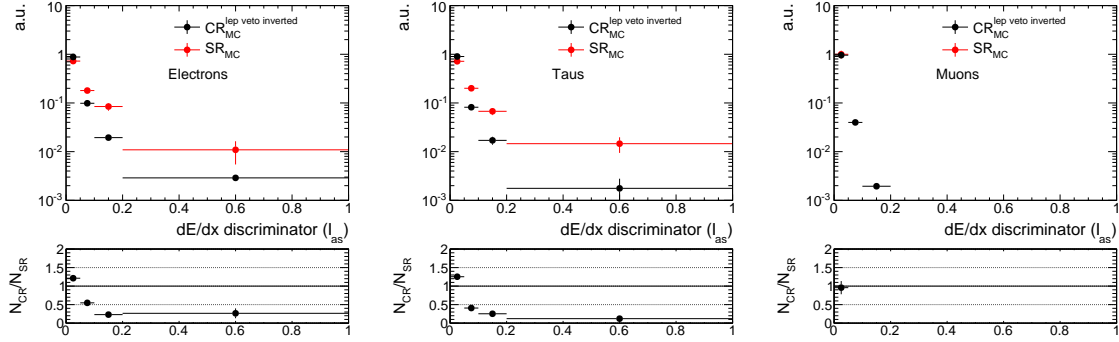


Figure 1.6.10: Normalised I_{as} distribution for electrons (left), pions from the tau decay (middle) and muons (right) in the signal region (red) and the lepton veto inverted control region (black).

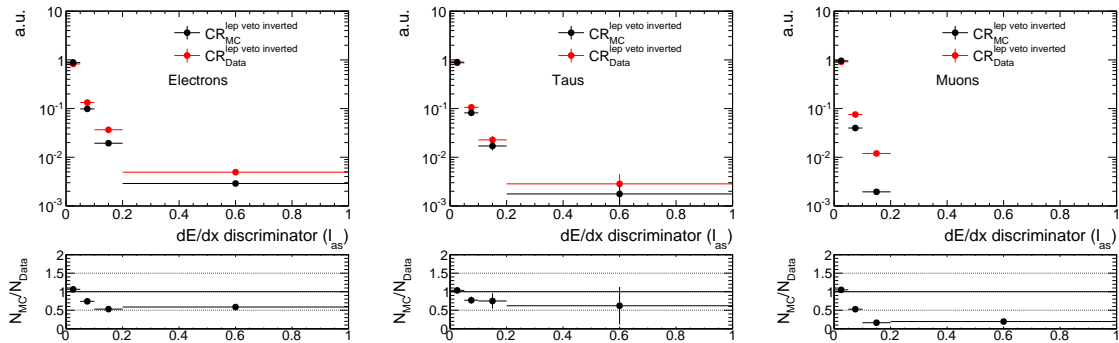


Figure 1.6.11: Normalised I_{as} distribution for electrons (left), pions from the tau decay (middle) and muons (right) in the lepton veto inverted control region from simulated events (black) and data (red).

1024 1.6.3 Background estimation validation

1025 The background estimation methods are exhaustively validated in signal depleted control
 1026 regions. Various control regions are used for validation. For each control region it has
 1027 been verified that the signal contamination is less than the statistical uncertainty of the
 1028 background prediction. For some of the models the expected number of events exceeds
 1029 this limit. However, these models are already ruled out by the search for disappearing
 1030 tracks [13] (see Appendix B.3).

1031 First, to validate the estimation method of the leptonic background, a leptonic control
 1032 region is defined by selecting only tracks with a minimum number of seven hits in the
 1033 tracker. This reduces the fake contribution to a negligible level (cf. Fig. 1.6.1). Addition-
 1034 ally in order to minimise signal contamination, the calorimeter isolation requirement is
 1035 inverted to $E_{\text{calo}}^{\Delta R < 0.5} > 10 \text{ GeV}$. This requirement ensures no overlap to the signal region.

1036 The validation test for the control region with $E_{\text{calo}}^{\Delta R < 0.5} > 10 \text{ GeV}$ and $N_{\text{hits}} > 6$ is shown
 1037 in Table 1.6.6. The predicted number of events by the leptonic background estimation is
 1038 compatible with the observed data yield.

Table 1.6.6: Validation test of leptonic background estimation. Left: $E_{\text{calo}}^{\Delta R < 0.5} > 10 \text{ GeV}$
 and $N_{\text{hits}} > 6$. Right: $E_{\text{calo}}^{\Delta R < 0.5} > 10 \text{ GeV}$, $N_{\text{hits}} > 6$ and $I_{\text{as}} > 0.2$. Only
 statistical uncertainties are included.

| | Predicted Yield | Data Yield | | Predicted Yield | Data Yield |
|-----------|----------------------------|------------|-----------|----------------------|------------|
| Total bkg | $131.70^{+26.30}_{-18.42}$ | 156 | Total bkg | $0.0^{+0.50}_{-0.0}$ | 1 |
| Electrons | $14.67^{+11.16}_{-6.29}$ | | Electrons | $0.0^{+0.07}_{-0.0}$ | |
| Muons | $7.99^{+10.90}_{-5.00}$ | | Muons | $0.0^{+0.32}_{-0.0}$ | |
| Taus | $109.04^{+21.18}_{-16.58}$ | | Taus | $0.0^{+0.38}_{-0.0}$ | |

1039
 1040 Second, the fake background can only be estimated within the low calorimeter isolation
 1041 region ($E_{\text{calo}}^{\Delta R < 0.5} < 10 \text{ GeV}$) to ensure high fake purity. To be able to validate the method
 1042 in the high calorimeter isolation region ($E_{\text{calo}}^{\Delta R < 0.5} > 10 \text{ GeV}$), a translation factor from the
 1043 low to the high calorimeter isolation region for the number of fake tracks is determined in
 1044 the fake enriched control region $\text{CR}_{I_{\text{as}}}^{\text{fake}}$ defined in Section 1.6.4.2. In this control region,
 1045 the ratio of $N_{E_{\text{calo}}^{\Delta R < 0.5} > 10 \text{ GeV}} / N_{E_{\text{calo}}^{\Delta R < 0.5} < 10 \text{ GeV}}$ is estimated and taken as a multiplicative
 1046 factor to the number of events predicted from the $E_{\text{calo}}^{\Delta R < 0.5} < 10 \text{ GeV}$ region. This method

is exposed to differences in the I_{as} shape of the two $E_{\text{calo}}^{\Delta R < 0.5}$ regions. In Fig. 1.6.12, a comparison between the I_{as} shape of fake tracks with low calorimeter energy deposits and high calorimeter energy deposits in the fake enriched control region is depicted. It shows, that fakes with higher associated calorimeter energy have typically lower I_{as} values. This can thus lead to an underprediction of the fake contribution in the high $E_{\text{calo}}^{\Delta R < 0.5}$ region. However, as the differences are not too pronounced, this effect is expected to be covered by

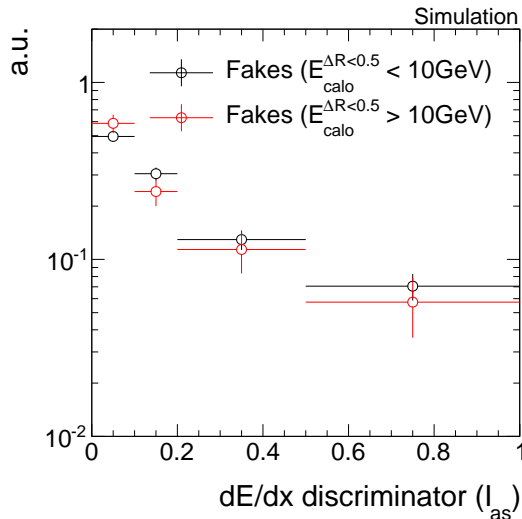


Figure 1.6.12: Comparison of the I_{as} shape of fake tracks with high calorimeter energy deposits (red) and low calorimeter energy deposits (black) in simulation. To enhance the statistical precision, no trigger selection is applied.

systematic uncertainties.FIXME, talk to Christian In Table 1.6.7, two different validation tests are shown, once an inclusive validation in I_{as} and once with an I_{as} selection of 0.2. Again, the predicted background events is in agreement with the number of observed events.

The whole validation is done for different selections in p_{T} and I_{as} . All validation tests show good agreement. Results of a variety of validation tests with different p_{T} and I_{as} selections can be found in Appendix B.4.

Still, systematic uncertainties need to be estimated. The sources of systematic uncertainties and how they are estimated will be explained in the following section.

Table 1.6.7: Validation test of fake and leptonic background estimation methods. Left: $E_{\text{calo}}^{\Delta R < 0.5} > 10 \text{ GeV}$. Right: $E_{\text{calo}}^{\Delta R < 0.5} > 10 \text{ GeV}$ and $I_{\text{as}} > 0.2$. Only statistical uncertainties are included.

| | Predicted Yield | Data Yield | | Predicted Yield | Data Yield |
|-----------|----------------------------|------------|-----------|-------------------------|------------|
| Total bkg | $308.35^{+33.48}_{-26.64}$ | 324 | Total bkg | $14.69^{+2.91}_{-2.84}$ | 16 |
| Electrons | $59.92^{+16.11}_{-11.85}$ | | Electrons | $0.75^{+0.36}_{-0.25}$ | |
| Muons | $8.04^{+10.97}_{-5.03}$ | | Muons | $0.00^{+0.32}_{-0.00}$ | |
| Taus | $173.06^{+24.62}_{-20.23}$ | | Taus | $2.33^{+0.74}_{-0.55}$ | |
| Fakes | $67.34^{+11.61}_{-11.61}$ | | Fakes | $11.61^{+2.78}_{-2.78}$ | |

1.6.4 Systematic uncertainties

Systematic uncertainties on the background estimation include:

- the uncertainty on the fake rate ρ_{fake} ;
- the uncertainty on the I_{as} shape of fake tracks predicted from a control region;
- the uncertainty on the leptonic scale factor $\rho_{\text{MC}}^{\text{lep}_i}$ determined with simulated events;
- the uncertainty on the I_{as} shape of the leptonic background.

1.6.4.1 Uncertainty on the fake rate

The fake rate ρ_{fake} is determined with the help of observed $Z \rightarrow \ell\bar{\ell}$ events. To estimate the uncertainty on this fake rate caused by differences in the fake rate between different underlying processes, a comparison between the fake rate in simulated $Z \rightarrow \ell\bar{\ell} + \text{jets}$ and simulated $W + \text{jets}$ events is done. The fake rate in the $Z \rightarrow \ell\bar{\ell} + \text{fake track control}$ samples (see Tables 1.6.2 and 1.6.3) and the fake rate in the signal candidate selection from Table 1.5.4 in $W + \text{jets}$ events are compared.

Unfortunately, the statistical precision of the simulated $W + \text{jets}$ dataset is limited. Thus, the estimation of the systematic uncertainty is mainly driven by statistical uncertainties. In order to enhance the statistical precision of the estimation, the selection requirements on \cancel{E}_{T} and $p_{\text{T}}^{\text{1st jet}}$ are loosened and the QCD suppression requirements are removed. These variables are not expected to be correlated with the fake rate and thus should not affect it. That this is indeed the case, can be seen in Table 1.6.8.

Table 1.6.8: Fake rates in simulated $W + \text{jets}$ and $Z \rightarrow \ell\bar{\ell} + \text{jets}$ events for different event-based selections of the $W + \text{jets}$ sample. The track-based selection is the candidate track selection from Table 1.5.4.

| $W + \text{jets}$ selection | $\rho_{\text{fake}}^{W+\text{jets}}$ | $\rho_{\text{fake}}^{Z \rightarrow \ell\bar{\ell}}$ |
|---|--|---|
| $\cancel{E}_{\text{T}} > 100 \text{ GeV}, p_{\text{T}}^{\text{1st jet}} > 110 \text{ GeV}$ | $(3.16^{+4.26}_{-1.94}) \cdot 10^{-5}$ | $(3.17 \pm 0.21) \cdot 10^{-5}$ |
| $\cancel{E}_{\text{T}} > 0 \text{ GeV}, p_{\text{T}}^{\text{1st jet}} > 70 \text{ GeV}$ | $(3.03 \pm 0.68) \cdot 10^{-5}$ | $(3.17 \pm 0.21) \cdot 10^{-5}$ |
| $\cancel{E}_{\text{T}} > 0 \text{ GeV}, p_{\text{T}}^{\text{1st jet}} > 70 \text{ GeV}, \text{no QCD cuts}$ | $(3.05 \pm 0.44) \cdot 10^{-5}$ | $(3.17 \pm 0.21) \cdot 10^{-5}$ |

The systematic uncertainty is estimated as the largest difference from one of the ratio $\rho_{\text{fake}}^{W+\text{jets}} / \rho_{\text{fake}}^{Z \rightarrow \ell\bar{\ell}}$ and its statistical uncertainty. For the candidate track selection, this is

estimated to $\rho_{\text{fake}}^{W+\text{jets}}/\rho_{\text{fake}}^{Z \rightarrow \ell\bar{\ell}} = 0.96 \pm 0.16$ leading to a systematic uncertainty on the fake rate of 20%.

1.6.4.2 Uncertainty on the dE/dx shape of fake tracks

The systematic uncertainty on the shape of the I_{as} distribution takes into account the differences between the I_{as} shape in the fake control region $\text{CR}_{I_{\text{as}}}^{\text{fake}}$ and in the signal region. For the estimation, information from simulated $W + \text{jets}$ events is used. A comparison between the simulated I_{as} shape in the signal and in the control region can be seen in Fig. 1.6.13. To enhance the statistical precision only track-based selection cuts are applied.

The largest deviation from one of the ratio of the number of events in the signal region and the control region with its 1-sigma statistical uncertainty is taken as systematic uncertainty. For a signal region definition with $p_T > 20 \text{ GeV}$ and $I_{\text{as}} > 0.2$ this corresponds to an uncertainty of around 21% and for a definition with $p_T > 40 \text{ GeV}$ and $I_{\text{as}} > 0.2$ of around 25%.

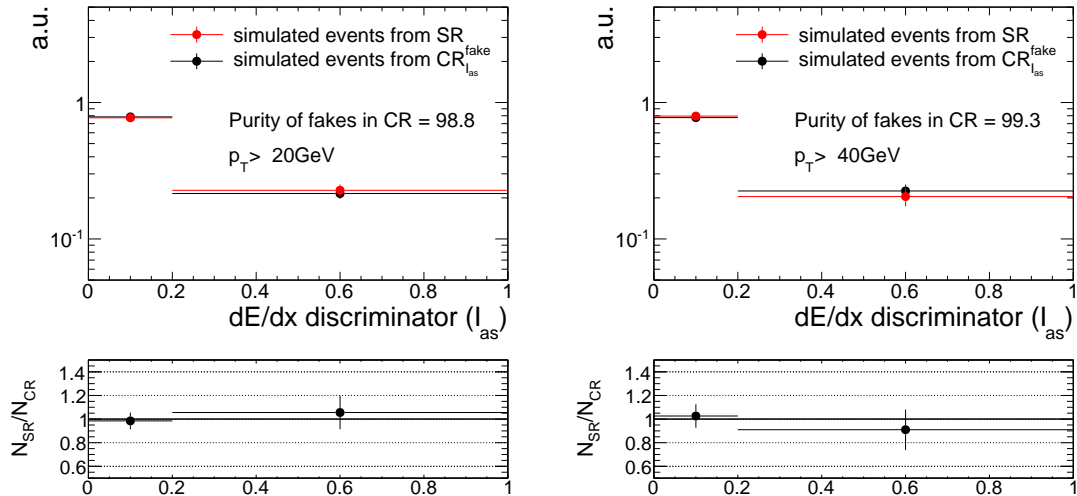


Figure 1.6.13: Normalised distributions of the I_{as} shape of fake tracks in the signal and control region of simulated $W + \text{jets}$ events with a p_T selection of 20 GeV (left) and a 40 GeV (right).

1095

1.6.4.3 Uncertainty on the leptonic scale factor

The leptonic scale factor $\rho_{\text{MC}}^{\text{lept}_i}$ is estimated on simulated $W + \text{jets}$ events. The corresponding systematic uncertainty that addresses the use of information from simulation is derived by a “tag-and-probe” method performed on real data and simulated events.

For this method a selection of $Z \rightarrow \ell\bar{\ell}$ events is done with one “tagged” well reconstructed lepton and one “probed” candidate track. To ensure a selection of $Z \rightarrow \ell\bar{\ell}$ events, a selection on the invariant mass of the reconstructed lepton and the candidate track is applied with $80 \text{ GeV} < M_{\text{inv}}(\text{lepton, cand. trk}) < 100 \text{ GeV}$ for muons and electrons. For taus, a muon from a $\tau \rightarrow \mu\nu\nu$ decay is selected with $40 \text{ GeV} < M_{\text{inv}}(\mu, \text{cand. trk}) < 75 \text{ GeV}$ and $m_T(\mu, \cancel{E}_T) < 40 \text{ GeV}$ [39, 40]. Furthermore, the candidate track and the lepton are required to be opposite in charge. In order to reduce the contamination of fakes in the “tag-and-probe” samples an additional selection on the number of hits of $N_{\text{hits}} > 5$ is required.

The “tag-and-probe” selection is done for each lepton type separately. In order to determine the leptonic scale factors, the number of events is once estimated for the candidate track selection including the corresponding lepton veto which gives the number of events in the “tag-and-probe” signal region $N_{\text{SR}}^{\text{T&P}}$, and once inverting the lepton veto selection requirement which gives the number of events in the “tag-and-probe” lepton inverted control region $N_{\text{CR, lepton veto inverted}}^{\text{T&P}}$. As for the determination of the tau and electron scale factor with simulated $W + \text{jets}$ events, no requirement on the calorimeter isolation is applied in the lepton veto inverted control region for taus and electrons. This leads to the following expression of the lepton scale factor for muons

$$\rho^\mu = \frac{N_{\text{SR}}^{\text{T&P}\mu}}{N_{\text{CR, } \mu \text{ veto inverted}}^{\text{T&P}}}.$$

and for electrons and taus

$$\rho^{e,\tau} = \frac{N_{\text{SR}}^{\text{T&P}e,\tau}}{N_{\text{CR, } e,\tau \text{ veto inverted}}^{\text{T&P}}}.$$

The selection requirements for the three tag-and-probe samples are listed in Tables B.11, B.12 and B.13 in Appendix B.5.

The leptonic scale factors are calculated using simulated $Z \rightarrow \ell\bar{\ell}$ events and real data from the single-muon and single-electron samples listed in Table 1.6.1. The largest difference from unity of the ratio $\rho_{\text{MC}}^{\text{lep}_i}/\rho_{\text{Data}}^{\text{lep}_i}$ and its statistical uncertainty is taken as systematic uncertainty. In Table 1.6.9, the results of the event yield in all control regions and the corresponding lepton scale factor are depicted. This results for the signal candidate selection in an uncertainty of 69% for the electron, 39% for the muon and 79% for the tau scale factor.

1.6.4.4 Uncertainty on the leptonic dE/dx shape

The uncertainty on lepton I_{as} shape is estimated by a comparison of the I_{as} shape in data and simulation in the lepton veto inverted control region. Figure 1.6.14 shows the leptonic I_{as} distributions for all three lepton types in the lepton veto inverted control region in data

Table 1.6.9: Event yields in the tag-and-probe signal region and control region with the resulting scale factors in simulation and data.

| | | Muons | Electrons | Taus |
|------------|--|---------------------------------|---------------------------------|---------------------------------|
| Data | $N_{\text{SR}}^{\text{T}\&\text{P} \ell_i}$ | 211 | 319 | 19 |
| | $N_{\text{CR}, \text{lep}_i \text{ veto inverted}}^{\text{T}\&\text{P}}$ | $4.10 \cdot 10^6$ | $3.74 \cdot 10^6$ | 33 |
| | ρ^{lep_i} | $(5.14 \pm 0.35) \cdot 10^{-5}$ | $(8.52 \pm 0.48) \cdot 10^{-5}$ | $(5.76 \pm 1.66) \cdot 10^{-1}$ |
| Simulation | $N_{\text{SR}}^{\text{T}\&\text{P} \ell_i}$ | 153.9 ± 15.4 | 125.1 ± 15.8 | 9.1 ± 4.0 |
| | $N_{\text{CR}, \text{lep}_i \text{ veto inverted}}^{\text{T}\&\text{P}}$ | $(4.284 \pm 0.003) \cdot 10^6$ | $(4.112 \pm 0.003) \cdot 10^6$ | $30.9 + / - 7.8$ |
| | ρ^{lep_i} | $(3.59 \pm 0.36) \cdot 10^{-5}$ | $(3.04 \pm 0.39) \cdot 10^{-5}$ | $(2.95 \pm 1.49) \cdot 10^{-1}$ |

and simulation. The largest difference from one of the ratio (and its statistical uncertainty) of the number of events in the control region in data and simulation is taken as systematic uncertainty. This leads for example to uncertainties between 37% – 81% for the signal candidate selection plus a selection requirement of $I_{\text{as}} > 0.2$.

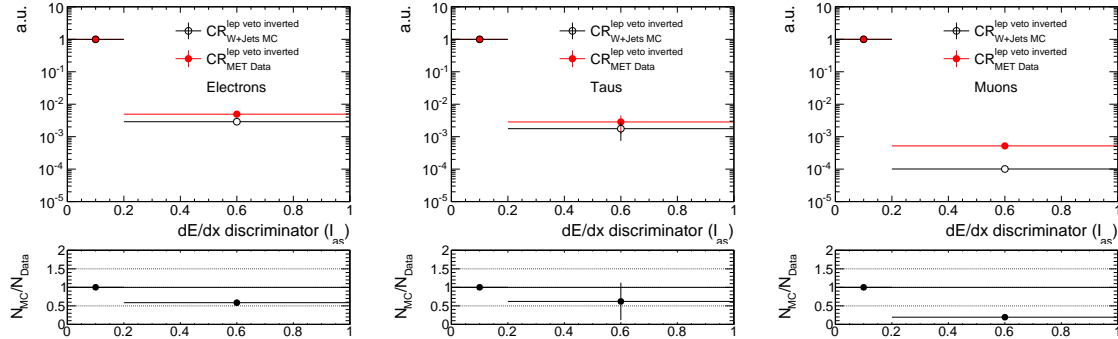


Figure 1.6.14: Normalised distributions of the lepton I_{as} distributions in the lepton veto inverted control region for data (red) and simulation (black) for all three lepton types. The event-based selection requirements and the calorimeter isolation requirement are removed to enhance the statistical precision.

¹¹³⁶ 1.7 Optimisation of the search sensitivity

¹¹³⁷ Finally, having all background estimation methods in place, an optimisation procedure is
¹¹³⁸ performed in order to increase the search sensitivity with respect to different signal models
¹¹³⁹ as introduced in Section 1.4.2. The optimisation is done in the most sensitive variables,
¹¹⁴⁰ p_T and I_{as} (see Section 1.3.3 for a definition and explanation of the Asymmetric Smirnov
¹¹⁴¹ discriminator I_{as}). A potential additional discriminating variable is the number of miss-
¹¹⁴² ing outer hits $N_{\text{lost}}^{\text{outer}}$ in the tracker system. This variable is, however, not considered in
¹¹⁴³ this analysis because the discriminating potential for this search is limited, as shown in
¹¹⁴⁴ Appendix B.6.

¹¹⁴⁵

¹¹⁴⁶ SUSY models with different chargino lifetimes and masses are characterised by different
¹¹⁴⁷ p_T and I_{as} distributions as well as different theoretical cross sections. Therefore, the usual
¹¹⁴⁸ search optimisation strategy that maximises $N_S/\Delta B$ (N_S = number of signal events of
¹¹⁴⁹ model S , ΔB = background uncertainty) implies a potential fine-tuning on the specific
¹¹⁵⁰ SUSY cross sections. In order to keep the search as general as possible, a cross section
¹¹⁵¹ independent optimisation is performed. This is achieved by a minimisation of the cross
¹¹⁵² section for which a 5σ -discovery ($\kappa = 5$) of the corresponding signal model is expected,
¹¹⁵³ i. e. finding the optimal selection cuts for p_T and I_{as} for which the lowest possible cross
¹¹⁵⁴ section, σ_{\min} , can be discovered

$$\kappa = \frac{\alpha_{\min} \cdot N_S(\text{mass}, c\tau, p_T^{\text{cut}}, I_{\text{as}}^{\text{cut}})}{\Delta B(p_T^{\text{cut}}, I_{\text{as}}^{\text{cut}})} = 5. \quad \text{with } \alpha_{\min} = \frac{\sigma_{\min}}{\sigma_S}. \quad (1.7.1)$$

¹¹⁵⁵ The number of expected events N_S of the signal model S depends on the p_T and I_{as} se-
¹¹⁵⁶ lection cut as well as the mass and the lifetime of the chargino. The uncertainty on the
¹¹⁵⁷ background ΔB is dependent on the p_T and I_{as} cut, and takes into account the full system-
¹¹⁵⁸ atic uncertainty as well as the statistical uncertainty on the background prediction which is
¹¹⁵⁹ defined as the 68% one sided upper limit of a Poisson distribution with $\mu = N_B$ estimated
¹¹⁶⁰ with the Neyman construction [22, 49]. The systematic uncertainty on the background
¹¹⁶¹ prediction includes systematic uncertainties as described in Section 1.6.4, and statistical
¹¹⁶² uncertainties arising from limited statistical precision of the control regions and simulated
¹¹⁶³ samples used in the background estimation. The factor α_{\min} that is minimised is the ratio
¹¹⁶⁴ of the minimum cross section σ_{\min} divided by the nominal cross section σ_S of the signal
¹¹⁶⁵ model S .

¹¹⁶⁶

As this analysis focuses on short tracks, rather low lifetimes are considered in the optimisation procedure: $c\tau = 1 \text{ cm}, 10 \text{ cm}, 50 \text{ cm}$. These lifetimes are further suitable as they lie at the edge of the sensitivity of the search for disappearing tracks [13]. To cover the full mass space, the optimisation is done for masses between 100 GeV and 500 GeV in steps of 100 GeV.

The corresponding results are shown in Table 1.7.1. It can be seen that the optimal

Table 1.7.1: Optimal p_T and I_{as} selection cuts and the corresponding minimum cross section σ_{\min} that can be discovered with 5σ significance for different signal models. For some signal samples, an optimisation result is not available due to the limited size of these samples.

| Mass [GeV] | Lifetime $c\tau$ [cm] | Optimal p_T cut | Optimal I_{as} cut | σ_{\min} |
|------------|-----------------------|-------------------|-----------------------------|-----------------|
| 100 | 1 | 30 | 0.05 | 61.596 |
| 200 | 1 | 20 | 0.05 | 43.414 |
| 300 | 1 | n/a | n/a | n/a |
| 400 | 1 | n/a | n/a | n/a |
| 500 | 1 | n/a | n/a | n/a |
| 100 | 10 | 30 | 0.05 | 1.531 |
| 200 | 10 | 30 | 0.30 | 0.561 |
| 300 | 10 | 30 | 0.30 | 0.354 |
| 400 | 10 | 30 | 0.30 | 0.238 |
| 500 | 10 | 50 | 0.30 | 0.201 |
| 100 | 50 | 50 | 0.30 | 0.435 |
| 200 | 50 | 50 | 0.30 | 0.110 |
| 300 | 50 | 50 | 0.30 | 0.063 |
| 400 | 50 | 50 | 0.30 | 0.045 |
| 500 | 50 | 50 | 0.30 | 0.037 |

selection is highly dependent on the signal models. The best sensitivity for low masses ($\leq 200 \text{ GeV}$) is mainly achieved by soft selection cuts in p_T between 20 to 30 GeV, while models with higher chargino masses require tighter p_T selections of around 50 GeV. The

optimal I_{as} selection is mostly dependent on the mass of the chargino. For low masses and low lifetimes a soft selection in $I_{\text{as}} > 0.05$ is preferred. Since for longer lifetimes more charginos are able to reach the tracking system, a tighter selection in I_{as} of 0.3 is preferable. Additionally, signal models with longer chargino lifetimes have a more pronounced right tail in the I_{as} distribution (cf. Fig. 1.3.9 (right)). For high masses the highest search sensitivity is always achieved by a high I_{as} selection cut of 0.3.

1182

In order to visualise the mass and $c\tau$ dependence of the optimal p_{T} and I_{as} selection, the optimisation results for two very different lifetimes (5 cm and 50 cm) and masses (100 GeV and 500 GeV) are shown in Fig. 1.7.1, where the minimum cross section that is possible to discover is shown in the $p_{\text{T}} - I_{\text{as}}$ plane. For simplicity, general systematic uncertainties on the leptonic and the fake background of 100% and 20% respectively are imposed in the visualisation. Uncertainties arising from limited statistical precision of the samples used for the background estimation are propagated consistently into formula 1.7.1. Similar to the full optimisation, it can be seen that for low masses and low lifetimes, the highest search sensitivity is achieved by imposing rather soft selection cuts on I_{as} and p_{T} . Optimising for higher lifetime pushes the optimal selection in p_{T} and I_{as} to larger values, where signal models with higher masses prefer even tighter I_{as} selection cuts than the corresponding lower mass signal model. It can also be seen, that for low lifetimes, the p_{T} dependence of the search sensitivity is less pronounced than for long lifetimes.

1196

Based on the optimisation, four different exclusive signal regions are defined in order to achieve an optimal coverage over a wide mass space and a high sensitivity for different lifetimes:

- 1200 1.) $30 \text{ GeV} < p_{\text{T}} < 50 \text{ GeV}$ and $0.05 < I_{\text{as}} < 0.3$
- 1201 2.) $p_{\text{T}} > 50 \text{ GeV}$ and $0.05 < I_{\text{as}} < 0.3$
- 1202 3.) $30 \text{ GeV} < p_{\text{T}} < 50 \text{ GeV}$ and $I_{\text{as}} > 0.3$
- 1203 4.) $p_{\text{T}} > 50 \text{ GeV}$ and $I_{\text{as}} > 0.3$.

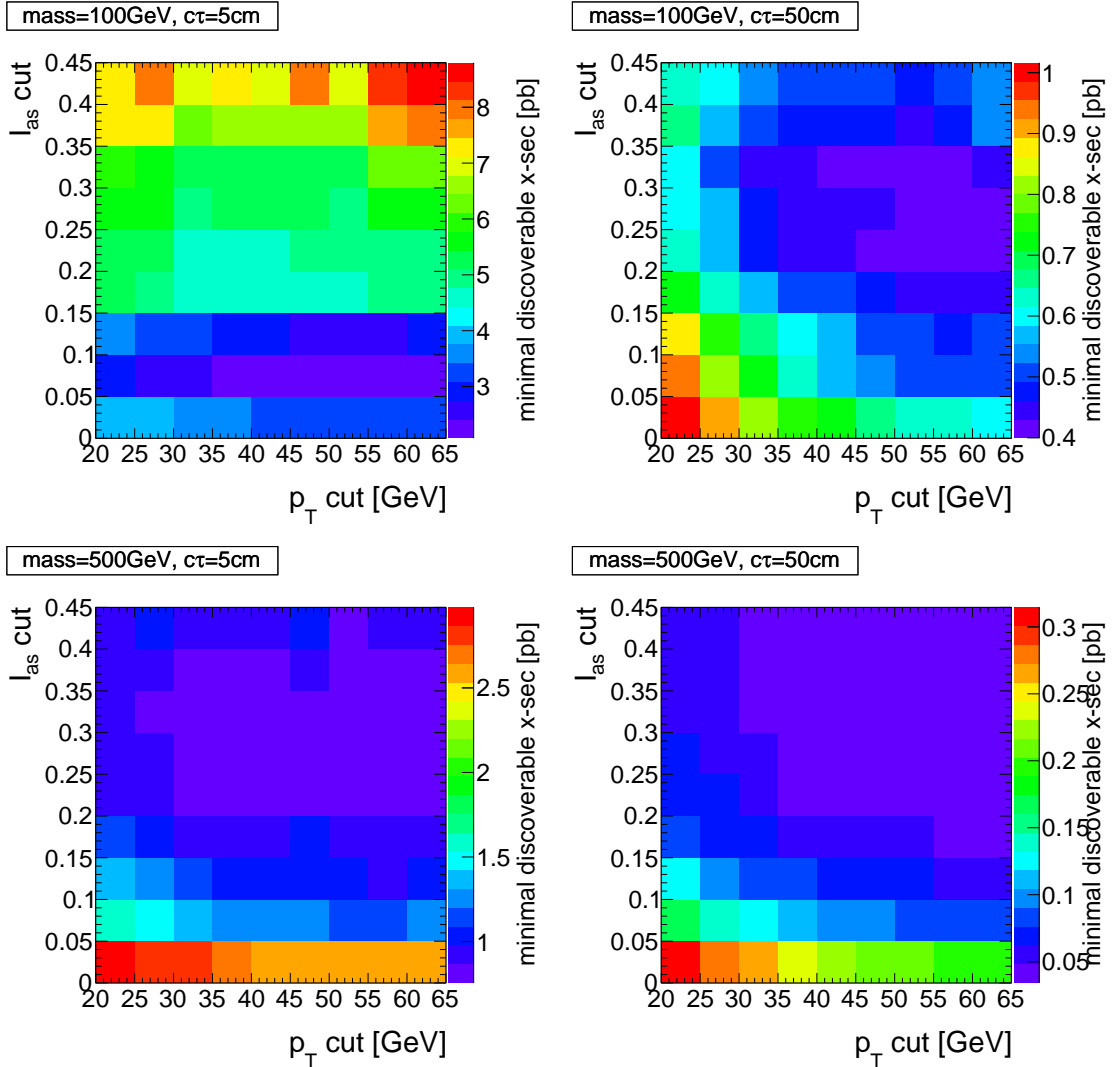


Figure 1.7.1: Minimum possible cross section that can be discovered with 5σ significance as a function of minimum p_T and I_{as} requirements for four different signal models. The systematic uncertainties are taken to be 20% and 100% for the fake and the leptonic background respectively. The uncertainty on the background arising from the limited size of the used samples are propagated consistently to the search optimisation. In Table B.3 of Appendix B.7, the corresponding histograms of the background yield, the background uncertainty and the signal yield for the four signal models can be found.

¹²⁰⁴ 1.8 Results

¹²⁰⁵ FIXME After developing the methods of the background estimation for all different back-
¹²⁰⁶ ground sources and their corresponding systematic uncertainties (all explained in Sec-
¹²⁰⁷ tion 1.6), the search is performed in four exclusive signal regions with 19.7 fb^{-1} of data
¹²⁰⁸ collected at a centre-of-mass energy of $\sqrt{s} = 8 \text{ TeV}$ at the CMS experiment. The predicted
¹²⁰⁹ numbers of events for the fake and the leptonic background in the four signal regions, as
¹²¹⁰ well as the number of observed events are listed in Table 1.8.1. It can be seen, that
¹²¹¹ fake tracks are by far the dominant background to this search. The leptonic background
¹²¹² contributes only in one signal region to the total background with a share of about 10%.

¹²¹³ Furthermore, the results are compatible with the Standard Model background within
¹²¹⁴ 1σ uncertainties in all four signal regions. This is also visualised in Fig. 1.8.1, where a
¹²¹⁵ comparison of the total background prediction to the number of observed events is shown.
¹²¹⁶ No excess above the SM prediction is observed in either of the four signal regions. Thus,
¹²¹⁷ no evidence for physics beyond the Standard Model could be found.

¹²¹⁸ Therefore, in the following section these results will be used to constrain the parameter
¹²¹⁹ space of supersymmetric models with almost mass degenerate charginos and neutralinos.

Table 1.8.1: Number of predicted (fake, leptonic and total) and observed events for the four different signal regions.

| Signal region | | Fake Bkg | | | Leptonic Bkg | | | Total Bkg | | | Data |
|---------------|-----------|----------|--------------------|------------|--------------|--------------------|------------|-----------|--------------------|------------|------|
| p_T [GeV] | I_{as} | pred | stat | sys | pred | stat | sys | pred | stat | sys | |
| 30-50 | 0.05-0.30 | 19.11 | $^{+2.61}_{-2.61}$ | ± 9.35 | 0.00 | $^{+2.58}_{-0.00}$ | ± 0.00 | 19.11 | $^{+3.67}_{-2.61}$ | ± 9.35 | 18 |
| 50- ∞ | 0.05-0.30 | 22.21 | $^{+3.60}_{-3.60}$ | ± 8.78 | 2.17 | $^{+2.99}_{-1.34}$ | ± 1.65 | 24.38 | $^{+4.68}_{-3.84}$ | ± 8.93 | 34 |
| 30-50 | 0.30-1.00 | 2.49 | $^{+0.85}_{-0.85}$ | ± 1.98 | 0.00 | $^{+0.22}_{-0.00}$ | ± 0.00 | 2.49 | $^{+0.87}_{-0.85}$ | ± 1.98 | 0 |
| 50- ∞ | 0.30-1.00 | 2.52 | $^{+1.14}_{-1.14}$ | ± 1.27 | 0.04 | $^{+0.30}_{-0.03}$ | ± 0.03 | 2.57 | $^{+1.18}_{-1.14}$ | ± 1.27 | 4 |

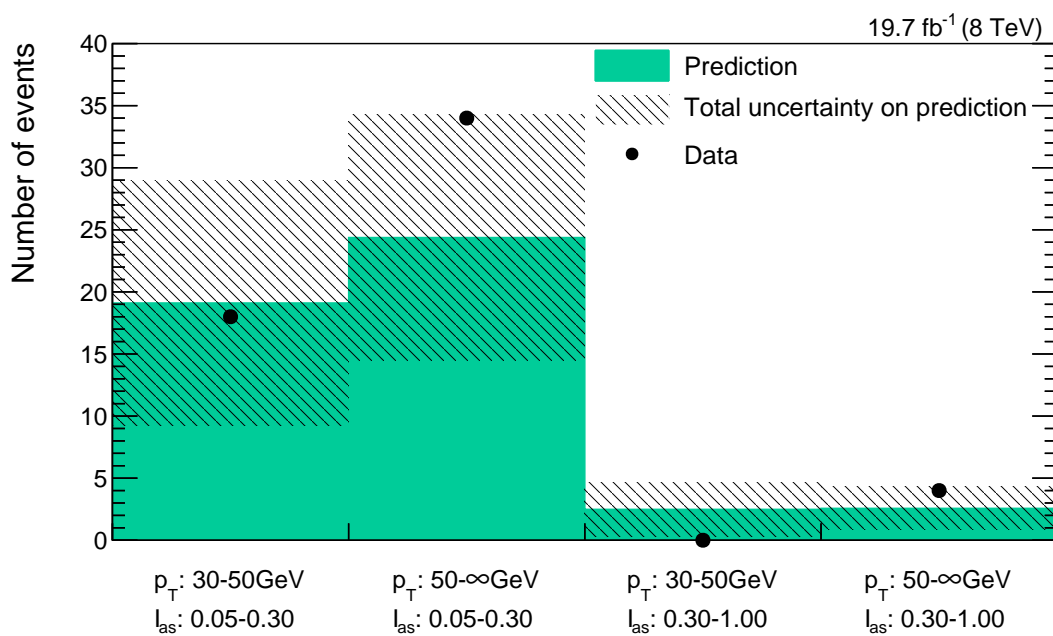


Figure 1.8.1: Number of predicted (green area) and observed (black dots) events for the four different signal regions. The hashed area represents the total uncertainty on the background prediction.

1220 1.9 Interpretation

1221 In order to interpret the result of the search in the context of supersymmetric models with
1222 almost mass degenerate charginos and neutralinos, sources of systematic uncertainties on
1223 the number of selected signal events must be identified and quantified. The interpretation
1224 will then be done with statistical methods that allow for the exclusion of parts of the
1225 supersymmetric parameter space on a 95% confidence level. The signal models used for
1226 this interpretation are listed in Section 1.4.2.

1227 1.9.1 Systematic uncertainties of simulated signal samples

1228 The systematic uncertainties on the number of signal events in the four signal regions are
1229 caused by uncertainties in the generation and simulation of signal events and the integrated
1230 luminosity of the considered data.

1231 All systematic uncertainties are estimated for each signal model (cf. Section 1.4.2) and
1232 each search bin separately. In the following, the sources of systematic uncertainties are
1233 discussed and the range of the corresponding uncertainty is given.

1234 Theoretical cross section

1235 The theoretical cross sections of $\tilde{\chi}_1^\pm \tilde{\chi}_1^\mp$ and $\tilde{\chi}_1^\pm \tilde{\chi}_1^0$ production at a centre-of-mass energy of
1236 8 TeV are taken from [37, 38]. The corresponding theoretical uncertainties range between
1237 4.5 – 12.1%.

1238 Luminosity

1239 The integrated luminosity recorded at CMS during the year 2012 is measured by count-
1240 ing of pixel clusters during the crossing of two bunches (zero-bias event). A detailed
1241 explanation of this method and the corresponding total uncertainty of 2.6% can be found
1242 in [50].

1243 Simulation of initial state radiation

1244 Initial state radiation (ISR) affects the transverse momentum distribution of the 2-particle
1245 system, $p_T(p_1^\mu + p_2^\mu)$, in a 2-body decay. Differences between data and simulation of ISR

are taken into account by reweighting the simulated events, such that the simulated transverse momentum distribution matches the measured distribution in data. The weights and associated systematic uncertainties are determined in [51] by comparing simulated and observed p_T distributions of Z and $t\bar{t}$ events. These weights are applied to the simulated $\tilde{\chi}_1^\pm \tilde{\chi}_1^\mp$ and $\tilde{\chi}_1^\pm \tilde{\chi}_1^0$ events. To account for the systematic uncertainties on the reweighting procedure, the event weights are varied up and down by up to 25% according to [51] depending on the transverse momentum of the $\chi_1\chi_2$ system. The resulting uncertainty on the ISR simulation is between 9.2 – 12.6%.

1254 Simulation of the trigger efficiency

1255 The HLTMonoCentralPFJet80_PFMETnoMu105_NHEF0p95 trigger with the higher MET
 1256 threshold of 105 GeV active in Run C and Run D during 2012 was not available in the simu-
 1257 lated signal samples. It is therefore emulated using HLT trigger information. More details
 1258 on the emulation of this trigger can be found in Appendix B.8.

1259 The trigger uncertainty is assessed by comparing data-simulation differences of the trig-
 1260 ger efficiency. This uncertainty has been quantified within [39,40] by comparing simulated
 1261 and measured trigger turn-on curves and determining weights for simulated events such
 1262 that simulated and observed turn-on curves are compatible. These event weights are ap-
 1263 plied on the simulated signal samples in this analysis and lead to changes in the signal
 1264 prediction of 1.9 to 4.4%, which are taken as systematic uncertainties.

1265 Jet energy scale

1266 The transverse momentum of all jets is corrected for non-uniformities in the energy re-
 1267 sponse as a function of the jet η and p_T and for data-simulation differences. The uncer-
 1268 tainty on the jet energy scale (JES) is neatly described and quantified in [52]. It arises
 1269 from uncertainties on the measured jet response in data including jet fragmentation, jet
 1270 flavor composition, etc.. The JES correction is applied as a multiplicative factor on each
 1271 jet’s transverse momentum contained in an event. The corresponding systematic uncer-
 1272 tainty is assessed by an up- and downward variation of the correction factor within 1σ .
 1273 The resulting uncertainties are of minor importance and range between 0.4 – 3.1%.

1274 Jet transverse-momentum resolution

1275 The jet transverse-momentum resolution (JER) is smaller in simulation than in measured
 1276 data (see Part ??). In order to take these differences into account, the simulated jet
 1277 transverse-momentum response is smeared to match the measured response. The system-
 1278 atic uncertainty on the smearing factors is estimated in [52,53]. It covers the uncertainty
 1279 on JER in data, including the JES uncertainty, uncertainties arising from out-of-cone

1280 showering etc. [52, 53]. The resulting uncertainty on the signal efficiency in this study is
 1281 between 0.1 – 2.0% and therefore almost negligible.

1282 **Simulation of the parton distribution functions**

1283 The parton distribution function (PDF) used for the simulation of proton-proton collisions
 1284 is provided by the CTEQ group [54] (see Section ?? for more information about PDFs).
 1285 In [54], a detailed description of the determination of a parton distribution function and
 1286 its uncertainties is given. Practically, the estimation of the PDF uncertainty is done by
 1287 the application of 44 different sets of event weights which take into account 22 different
 1288 sources of uncertainties [55,56] (up and down variations lead to a factor of 2). The sources
 1289 correspond inter alia to uncertainties in the single distributions of gluons, up/down-quarks,
 1290 etc, with the gluon distribution being by far the largest source of uncertainty. The resulting
 1291 uncertainties on the signal efficiency for this search are between 2.6 – 6.8%.

1292 **Pileup reweighting**

1293 The distribution of the number of primary vertices in simulation is reweighted to match the
 1294 measured distribution in data. The distribution of the number of primary vertices in data
 1295 is estimated by the luminosity of each bunch-crossing times the proton-proton inelastic
 1296 cross section which is 69.4 mb [57]. The uncertainty on the number of interactions thus
 1297 consists of the uncertainty on the luminosity and the uncertainty on the cross section. To
 1298 cover both sources, a variation of the inelastic cross section by plus/minus 5% is done
 1299 according to the recommendation by [58].

1300 For most of the signal models and signal regions, the signal efficiency is only affected by
 1301 less than 1% by the pileup reweighting uncertainty. If the statistical precision of the signal
 1302 prediction in a specific search bin is low, the uncertainty can become significantly larger.
 1303 However, the search sensitivity is always driven by search bins with high signal content so
 1304 that large values of this uncertainty have no effect on the overall search sensitivity.

1305 **Simulation of the calorimeter isolation**

1306 The uncertainty on the simulation of the calorimeter isolation $E_{\text{calo}}^{\Delta R < 0.5}$ is estimated by
 1307 comparing simulated and measured selection efficiencies of $E_{\text{calo}}^{\Delta R < 0.5} < 5 \text{ GeV}$ in the fake
 1308 enriched control sample $\text{CR}_{I_{\text{as}}}^{\text{fake}}$. The fake enriched control region is well suited for this es-
 1309 timation, because fake tracks are not correlated to the energy deposits in the calorimeters.
 1310 The selection efficiency in data is higher than in simulation in both p_T bins of $30 - 50 \text{ GeV}$
 1311 and $50 - \infty \text{ GeV}$. This difference between data and simulation is taken as systematic
 1312 uncertainty, resulting in uncertainties of 12.1% and 3.0%.

1313 Simulation of missing middle/inner hits

1314 The uncertainty on the simulation of the number of missing inner and middle hits is
 1315 assessed by comparing the probability in simulation and data of passing the selection
 1316 requirements of $N_{\text{miss}}^{\text{middle/inner}} = 0$ of a candidate track in the muon-veto inverted control
 1317 region. This control region is particularly suitable because muons are not expected to
 1318 have intrinsic sources of missing hits, as e.g. pions or electrons have. Pions can interact
 1319 nuclearly with the tracker material and electrons can have sizable radiative losses, such
 1320 that both can change direction or don't deposit energy in a tracker layer. For muons, on
 1321 the other hand, sources of missing inner and middle hits are mainly algorithmic [39, 40],
 1322 making them very similar to the algorithmic sources of missing inner/middle hits for
 1323 chargino tracks.

1324 The uncertainty is estimated as the observed difference of the cut selection efficiency
 1325 of $N_{\text{miss}}^{\text{middle/inner}} = 0$ in data and simulation. The selection efficiency is always higher
 1326 in simulation, resulting in systematic uncertainties of around 3.5% for the simulation of
 1327 $N_{\text{miss}}^{\text{inner}} = 0$ and around 2.2% for $N_{\text{miss}}^{\text{middle}} = 0$. The uncertainties are of very similar size in
 1328 the signal regions with different p_{T} . No I_{as} dependence is considered.

1329 Simulation of I_{as}

1330 An uncertainty on the simulation of I_{as} needs to be estimated in order to account for
 1331 possible data-simulation differences for highly ionising particles. The estimation of the
 1332 I_{as} uncertainty is done following the methodology in [14, 59]. The I_{as} uncertainty can be
 1333 assessed by comparing data and simulation differences of slow protons. Slow protons are
 1334 highly ionising and can thus be used to determine the uncertainty in the high I_{as} region.

1335 In order to select slow protons, high quality tracks with a momentum smaller than
 1336 2.5 GeV are selected. The I_{as} versus momentum distribution for the selected tracks is
 1337 shown in Fig. 1.9.1. The kaon and proton line are visible in both datasets. The deuteron
 1338 line is only visible in data, as deuteron's are not simulated. Two different slices in the
 1339 momentum are extracted where the proton line is contained: p between 0.80 – 0.85 GeV
 1340 and 0.95 – 1.00 GeV. A Gaussian function is fitted to the proton peak and the maximum
 1341 difference of the mean of the fitted Gaussian between simulation and observed data is
 1342 taken as systematic uncertainty. The I_{as} distribution for the two momentum ranges with
 1343 the Gaussian fit is depicted in Fig. 1.9.2. The systematic uncertainty is estimated to a
 1344 value of 6%.

1345 Simulation of the track reconstruction efficiency

1346 One final source of uncertainty is the simulation of the track reconstruction efficiency.
 1347 Possible differences of the reconstruction efficiency in simulation and data can lead to a

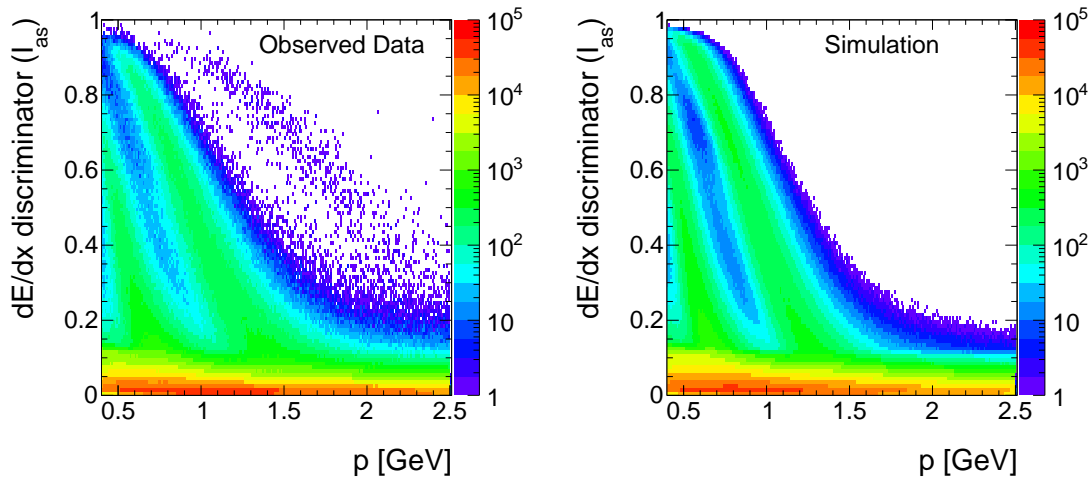


Figure 1.9.1: I_{as} versus momentum for good quality tracks with at least eight hits in observed data (left) and simulation (right).

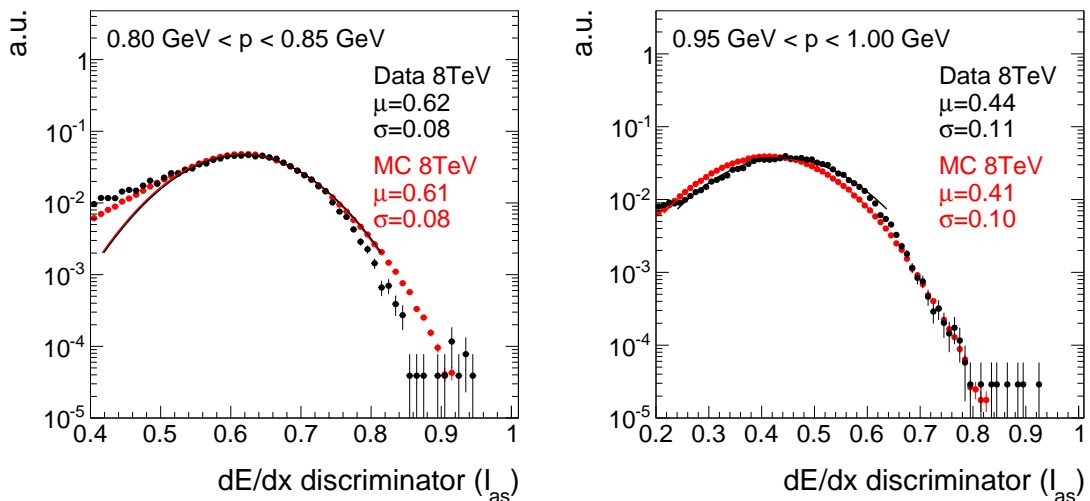


Figure 1.9.2: I_{as} distribution for slow protons in simulation and observed data for a momentum range of $0.80 - 0.85 \text{ GeV}$ (left) and $0.95 - 1.00 \text{ GeV}$ (right). For the momentum range of $0.80 - 0.85 \text{ GeV}$, the proton line is contained between I_{as} values of $0.4 - 0.8$, whereas for the momentum range of $0.95 - 1.00 \text{ GeV}$, the proton line I_{as} lies between $0.2 - 0.6$.

¹³⁴⁸ different signal acceptance. Differences in the track reconstruction efficiency are especially
¹³⁴⁹ expected for short tracks. Therefore, a worst case estimation is done, comparing the track
¹³⁵⁰ reconstruction efficiency in data and simulation for tracks with only three hits.

1351 In simulation and observed data, well reconstructed muon tracks are selected and all
1352 hits after the third hit are removed. Afterwards the full track reconstruction is performed
1353 again. The relative difference of this track reconstruction efficiency in data and simulation
1354 is taken as systematic uncertainty. The track reconstruction efficiency is higher in simu-
1355 lation than in data and results in uncertainties between 4.6 – 6.0%.

1356

1357 **Summary of systematic uncertainties on the simulated signal samples**

1358 All systematic uncertainties are estimated for all simulated signal samples and in each of
1359 the four signal regions. An overview of the range of the uncertainties is given in Table 1.9.1.

Table 1.9.1: Ranges of systematic uncertainties on the simulated signal samples. Min and Max correspond to variations between different signal samples and search bins.

| Uncertainty | Min [%] | Max [%] |
|---|---------|---------|
| Theoretical x-section | 4.5 | 12.1 |
| Luminosity | 2.6 | 2.6 |
| Simulation of ISR | 9.2 | 12.6 |
| Simulation of trigger efficiency | 1.9 | 4.4 |
| JES | 0.4 | 3.1 |
| JER | 0.1 | 2.0 |
| Simulation of PDF | 2.6 | 6.8 |
| Pileup reweighting | 0.0 | 16.0 |
| Simulation of calorimeter isolation | 3.0 | 12.1 |
| Simulation of missing middle hits | 2.2 | 2.2 |
| Simulation of missing inner hits | 3.3 | 3.7 |
| Simulation of I_{as} | 6.0 | 6.0 |
| Simulation of track reconstruction efficiency | 4.6 | 6.0 |

1360 In order to avoid an overestimation of the systematic uncertainties due to limited sizes
1361 of the samples (especially for low lifetimes like 1 cm), the corresponding signal sample with
1362 longer lifetime (100 cm) is used instead for determining the systematic uncertainty. This

1363 is possible for uncertainty sources, where the size is not affected by the lifetime of the
 1364 chargino, including ISR, trigger efficiency, JES, JER, and PDF uncertainties.

1365 It can be seen, that major uncertainties are the simulation of the initial state radiation,
 1366 of the calorimeter isolation, and of I_{as} . The high maximum value of the pileup uncertainty
 1367 is caused by limited statistical precision.

1368 The systematic uncertainties on the simulated signal samples are considered as fully
 1369 correlated among the four signal regions.

1370 1.9.2 Statistical Methods/ Limit setting

1371 This section is a small interlude to briefly introduce the methods and techniques that are
 1372 used to exclude beyond-SM models with the results of this search. For a detailed and
 1373 pedagogical introduction to the methods, the reader is referred to [60].

1374 In this analysis, the exclusion of the underlying theoretical model is achieved with the
 1375 CL_s method [61–63]. A model is considered as excluded at a 95% confidence level if CL_s
 1376 is smaller than 5%. The CL_s method was developed for the Higgs searches at LEP in
 1377 order not to overestimate the exclusion power of a result if an under-fluctuation of the
 1378 background expectation occurs. CL_s is defined as the confidence level of the background
 1379 plus signal hypothesis divided by the confidence level of the background only hypothesis

$$\text{CL}_s = \frac{\text{CL}_{s+b}}{\text{CL}_b}.$$

1380 The confidence level CL is defined as the probability of obtaining less than or equal the
 1381 number of observed events $P(n \leq n_{\text{obs}})$ for a given background (or background+signal)
 1382 hypothesis. For Poissonian statistics it leads to the following expressions for CL_{s+b} and
 1383 CL_b for one signal region

$$\begin{aligned} \text{CL}_{s+b} &= \text{Poisson}(n \leq n_{\text{obs}} | \lambda = b + \mu \cdot s), \\ \text{CL}_b &= \text{Poisson}(n \leq n_{\text{obs}} | \lambda = b), \end{aligned} \quad (1.9.1)$$

1384 where λ is the mean of the Poisson distribution and the signal strength μ is the measure
 1385 for the size of the signal cross section.

1386 Systematic uncertainties are included by varying the background expectation b and the
 1387 signal expectation $\mu \cdot s$ according to a predefined probability density function (pdf). For
 1388 one Gaussian distributed source of systematic uncertainty on the background, this leads
 1389 to the following expressions for CL_{s+b} and CL_b

$$\begin{aligned} \text{CL}_{s+b} &= \text{Poisson}(n \leq n_{\text{obs}} | \lambda = b \cdot (1 + \delta_b) + \mu \cdot s) \text{Gauss}(\delta_b | \text{mean} = 0, \sigma = \sigma_b), \\ \text{CL}_b &= \text{Poisson}(n \leq n_{\text{obs}} | \lambda = b \cdot (1 + \delta_b)) \text{Gauss}(\delta_b | \text{mean} = 0, \sigma = \sigma_b), \end{aligned} \quad (1.9.2)$$

1390 These expressions can be generalised for more than one signal region and more than one
 1391 systematic uncertainty [60]. In case of multiple signal regions, the distribution of the
 1392 systematic uncertainties becomes a multi-dimensional probability density function that
 1393 takes the covariance matrix of the systematic uncertainties in different signal regions into
 1394 account.

1395 In this analysis, the procedure for limit setting follows [64]. Instead of the number of
 1396 observed events, the profile likelihood ratio

$$q(n, \mu) = -2 \ln \frac{\mathcal{L}(n|\mu, \hat{\delta}_b, \hat{\delta}_s)}{\mathcal{L}(n|\hat{\mu}, \hat{\delta}_b, \hat{\delta}_s)}, \quad (1.9.3)$$

1397 is used as the test statistics for determining CL_{s+b} and CL_b ($\mu = 0$). \mathcal{L} refers to the
 1398 likelihood function

$$\mathcal{L}(n|b, s, \delta_b, \delta_s) = \text{Poisson}(n|\lambda = b \cdot (1 + \delta_b) + \mu \cdot s(1 + \delta_s)) p(\delta_b) p(\delta_s). \quad (1.9.4)$$

1399 that already appeared in Eq. (1.9.1). The parameters $\hat{\mu}$, $\hat{\delta}_b$ and $\hat{\delta}_s$ are fixed to the values
 1400 that maximise the likelihood with respect to the observed data. Determining CL_{s+b} and
 1401 CL_b requires knowing the probability distributions of q for the signal+background hypoth-
 1402 esis (depending on μ) and the background-only hypothesis ($\mu = 0$). These distributions
 1403 are determined by toy pseudo data with fixed values for δ_s and δ_b . Finally, the signal
 1404 strength μ is adjusted until CL_{s+b} calculated based on q - equals 0.05%. Signal models are
 1405 considered as excluded on a 95% confidence level, if the signal strength is larger than the
 1406 one found by the limit setting procedure.

1407

1408 In this search, the systematic uncertainties on the background and the signal yields as
 1409 well as the statistical uncertainty on the fake background are modelled with log-normal
 1410 distributions, whereas the statistical uncertainties on the leptonic background are mod-
 1411 elled using gamma distributions. A log-normal distribution is used instead of a normal
 1412 distribution to ensure that the prediction cannot become negative. The gamma distribu-
 1413 tion is well suited for statistical uncertainties arising from very limited statistical precision
 1414 in control regions or in simulated samples that are used for the background estimation [65].

1415 Correlations between systematic uncertainties on the background expectation in differ-
 1416 ent search bins are assumed as shown in Table 1.9.2. The systematic uncertainties on the
 1417 expected signal yields are considered fully correlated across search bins.

1418 The exclusion limits are derived according to the above presented methodology using
 1419 the *Combine* framework [65] which was developed for the Higgs searches at CMS.

Table 1.9.2: Correlation of systematic and statistical uncertainties between the four different signal regions. Statistical uncertainties include uncertainties arising from the limited size of control regions and the simulated samples.

| | Fakes | Taus | Electrons | Muons |
|-----------------------------------|---|---|---|---|
| Statistical uncertainty | 0% correlated | 100% for bins with same I_{as} | 0% correlated | 100% for bins with same I_{as} |
| Leptonic scale factor uncertainty | - | 100% for bins with same I_{as} | 100% for bins with same I_{as} | 100% for bins with same I_{as} |
| Fake rate uncertainty | 100% for bins with same I_{as} | - | - | - |
| I_{as} uncertainty | 0% correlated | 100% for bins with same p_T | 100% for bins with same p_T | 100% for bins with same p_T |

1.9.3 Exclusion limits

The presented search for highly ionising, short tracks is interpreted in the context of SUSY models with almost mass degenerate wino-like charginos and neutralinos. As explained in the previous section, the exclusion is done with the help of the CL_s method. Two direct production channels are taken into account: chargino pair production and chargino neutralino production. The corresponding cross sections can be found in Table 1.4.2.

In total, 37 different lifetimes from $c\tau = 1 - 10000 \text{ cm}$ for each mass point ($100 - 600 \text{ GeV}$ in steps of 100 GeV) are considered. Four exemplary exclusion limits are shown in Fig. 1.9.3, the full set of exclusion limits can be found in Appendix B.9.

1429

The upper 95% confidence level (CL) limit on the signal cross section is strongest for lifetimes between $10 - 100 \text{ cm}$. For lower lifetimes a sizable fraction of the charginos already decay before reaching the tracker. For longer lifetimes, the cross section upper limit gets weaker again because the charginos start to be reconstructed as muons and do not pass the muon veto. Also, the $E_{\text{calo}}^{\Delta R < 0.5}$ requirement rejects these charginos with higher efficiency.

Due to the falling spectrum of the chargino production cross section, charginos with lower masses are more effectively excluded than charginos with higher masses. A 2-dimensional exclusion limit in the chargino lifetime-mass parameter space is shown in

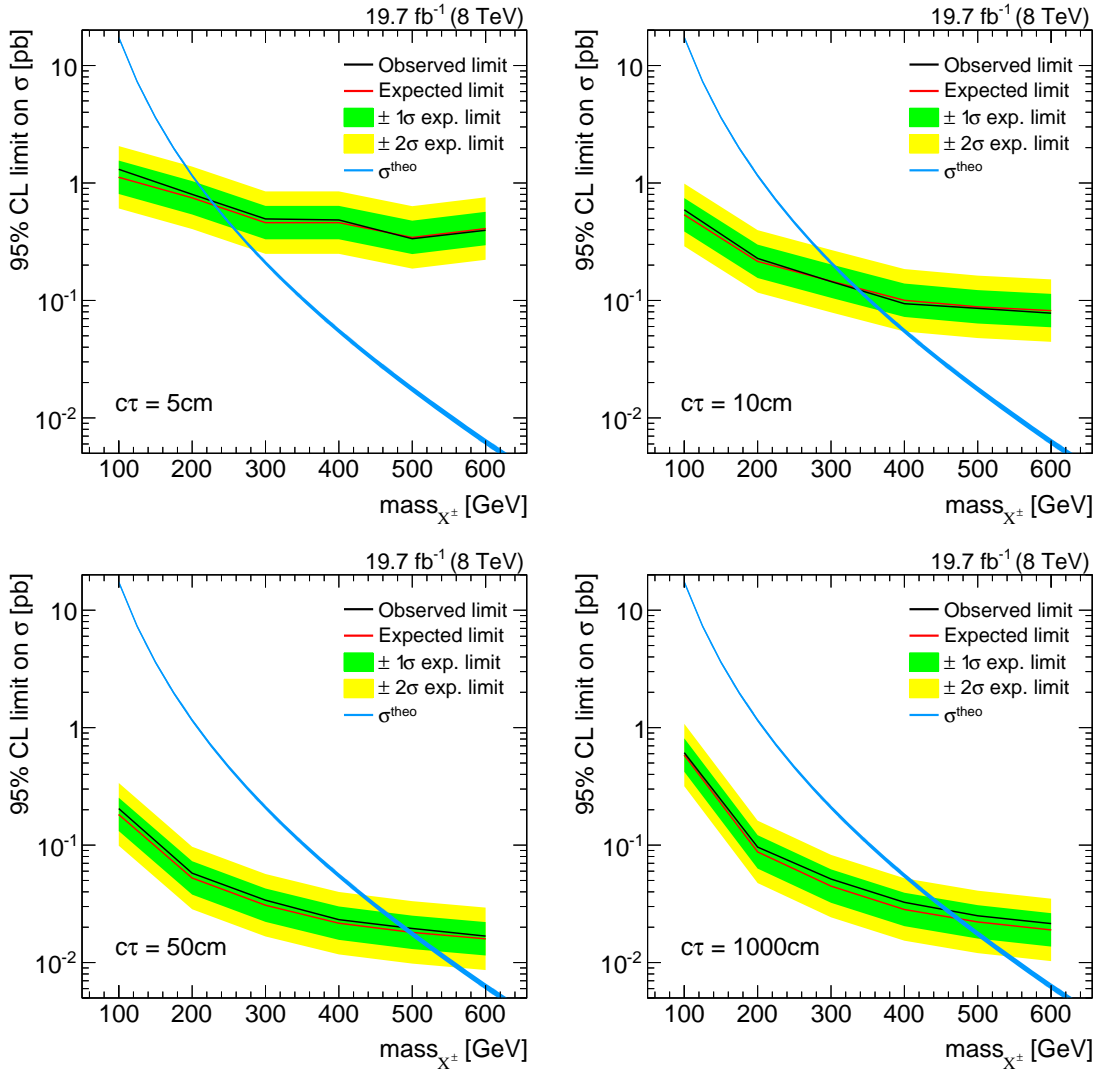


Figure 1.9.3: Four different CL_s exclusion limits for charginos with mean lifetimes of 5 cm (top left), 10 cm (top right), 50 cm (bottom left), 1000 cm (bottom right). The red line depicts the expected 95% confidence level (CL) upper cross-section limit with the $1-\sigma$ (green band) and $2-\sigma$ (yellow band) intervals. The black line is the observed limit. The signal cross section is depicted as a blue line. SUSY models can be excluded at 95% CL if the signal cross section is at least as large as the 95% CL observed upper limit on the cross section.

Fig. 1.9.4.

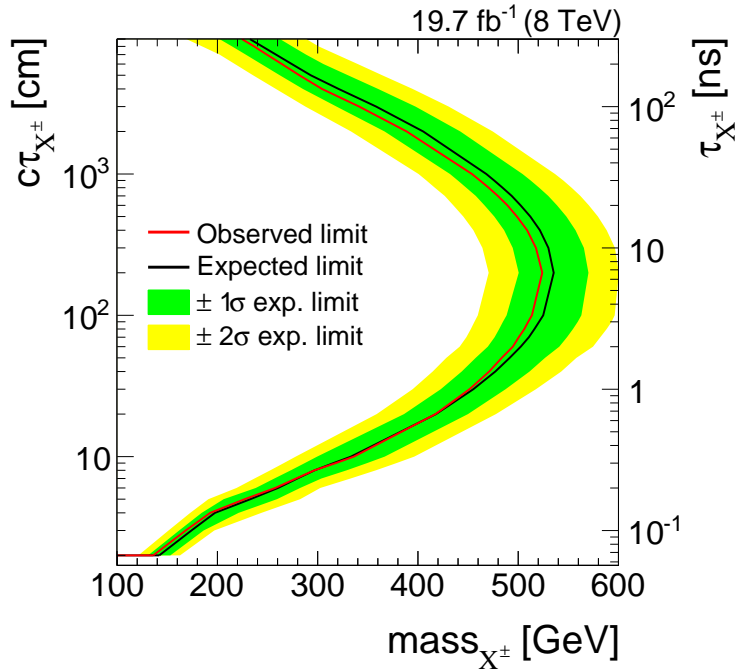


Figure 1.9.4: Excluded regions in the mass versus lifetime space. All excluded models are located left of the contour line. The red line depicts the expected 95% CL upper cross-section limit with the 1- σ (green band) and 2- σ (yellow band) intervals. The black line is the observed limit.

1438

1439 Charginos with masses of 100 GeV can be excluded down to a lifetime of $c\tau = 2$ cm.

1440 Charginos with a higher mass of 500 GeV are excluded for lifetimes between $c\tau = 70 -$
1441 500 cm.

1442

1443 Since the lifetime of a wino-like chargino is determined by the mass splitting between
1444 $m_{\tilde{\chi}_1^\pm}$ and $m_{\tilde{\chi}_1^0}$, it is possible to express the lifetime of the chargino as a mass gap $\Delta m_{\tilde{\chi}_1^\pm \tilde{\chi}_1^0}$
1445 between the chargino and the lightest neutralino. The correspondence between lifetime
1446 and mass gap is taken from [66], where the decay width of $\tilde{\chi}_1^\pm \rightarrow \tilde{\chi}_1^0 \pi^\pm$ is expressed in
1447 terms of chargino, neutralino, and pion mass. Thus, the mass gaps that are considered
1448 are bounded by the pion mass of ~ 140 MeV. The corresponding 2d exclusion limit can be
1449 found in Fig. 1.9.5. It can be seen that this search is sensitive to mass splittings between
1450 ~ 140 MeV – 210 MeV.

1451

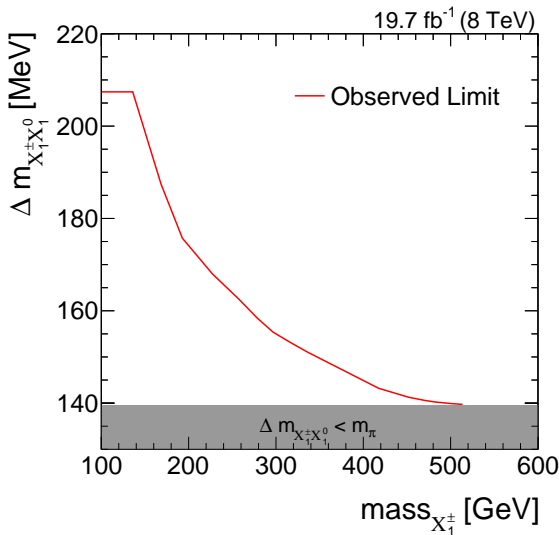


Figure 1.9.5: Excluded parameter region at 95% CL for wino-like charginos and neutralinos depending on the chargino mass and the mass splitting between $\tilde{\chi}_1^\pm$ and $\tilde{\chi}_1^0$, $\Delta m_{\tilde{\chi}_1^\pm \tilde{\chi}_1^0}$. All SUSY models between the red line and the grey area are excluded.

1.9.4 Comparison to the search for disappearing tracks

The presented exclusion limits confirm the exclusion from the search for disappearing tracks [13] with slight improvements in the low lifetime region. The comparison of the two searches is shown in Fig. 1.9.6.

For charginos with a lifetime of $\tau = 0.07$ ns ($c\tau = 2.1$ cm), the observed limit of this search improves the limits derived in [13] by ~ 35 GeV in chargino mass, for a lifetime of $\tau = 0.4$ ns ($c\tau = 12.0$ cm) by ~ 25 GeV. For SUSY models with long chargino lifetimes the here presented search shows a higher exclusion power. The weaker exclusion for long lifetimes in [13] is caused by the additional selection cut on the number of missing outer hits, $N_{\text{lost}}^{\text{outer}} \geq 3$.

The confirmation of the excluded parameter space in [13] is especially interesting since the signal regions of the two searches show little correlation for small lifetimes. The correlation between simulated signal events, that pass the selection from [13], N_A , and the selection used in this analysis, N_B , can be estimated by the event overlap ρ_{corr}

$$\rho_{\text{corr}} = \frac{N_{A \cap B}}{N_{A \cup B}} = \frac{N_{A \cap B}}{N_A + N_B - N_{A \cap B}}.$$

In order to avoid an over- or underestimation of the event overlap, only the most sensitive signal region from this search is included in N_B . The degree of correlation is depicted in Fig. 1.9.7 which shows the event overlap for signal models with chargino masses between

¹⁴⁶⁹ 100 – 600 GeV and lifetimes between 5 cm – 1000 cm.

¹⁴⁷⁰ It can be seen that the event overlap for intermediate lifetimes of around 100 cm is
¹⁴⁷¹ around 60% and decreases for shorter lifetimes to small overlaps of around 15 – 20%.
¹⁴⁷² Additionally, the two events that were observed in data by [13] in their signal region
¹⁴⁷³ are not contained in any of the signal regions in the here presented analysis. Thus, this
¹⁴⁷⁴ analysis constitutes an independent confirmation of the exclusion limits derived in [13].

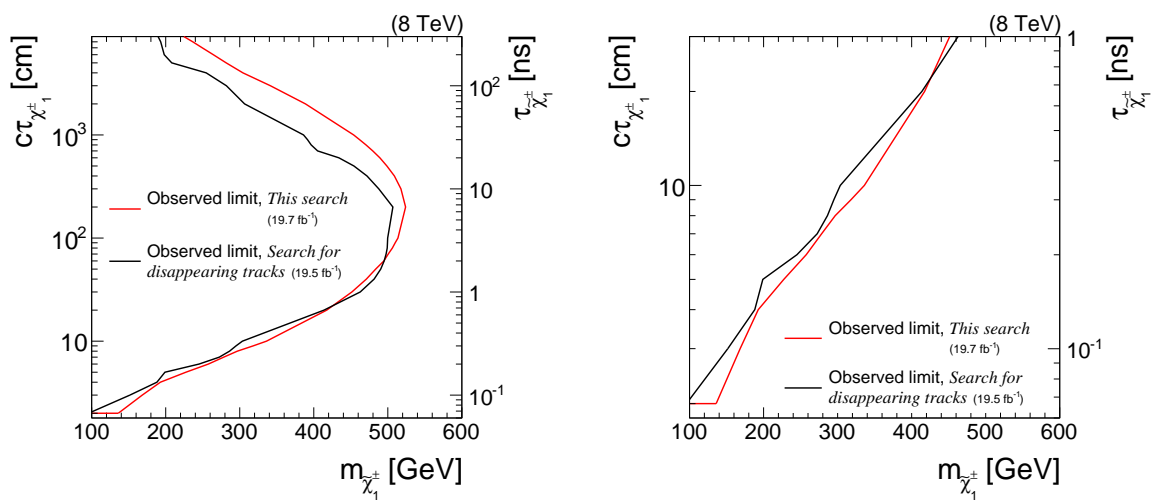


Figure 1.9.6: Comparison of the excluded regions in the mass versus lifetime space in this analysis (red line) and the search for disappearing tracks [13] (black line). The right figure is a zoom on the low lifetime region. All SUSY models left of the lines are excluded.

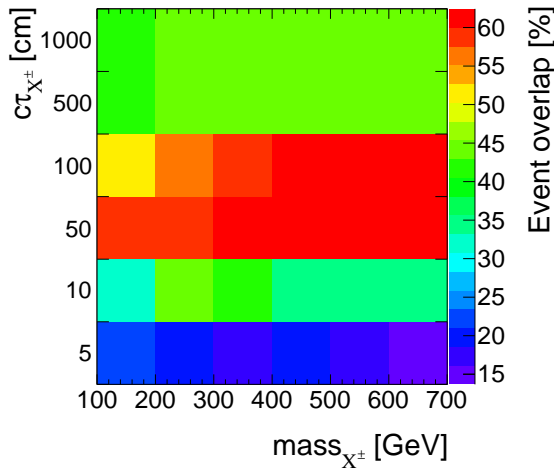


Figure 1.9.7: The event overlap between simulated signal events, that pass the selection from [13] and the selection used in this analysis for different signal models. The correlation is determined using only the signal region with the highest sensitivity of this analysis.

¹⁴⁷⁵ 1.10 Conclusion and outlook

¹⁴⁷⁶ The here presented search for highly ionising, short tracks is motivated by supersym-
¹⁴⁷⁷ metric models with almost mass-degenerate wino-like charginos $\tilde{\chi}_1^\pm$ and neutralinos $\tilde{\chi}_1^0$.
¹⁴⁷⁸ Such scenarios can have interesting astrophysical implications [9] and occur naturally in
¹⁴⁷⁹ Supersymmetry, if the wino mass parameter is smaller than the bino and higgsino mass
¹⁴⁸⁰ parameters.

¹⁴⁸¹

¹⁴⁸² The presented analysis targets SUSY models with intermediate chargino lifetimes. This
¹⁴⁸³ is achieved by searching for isolated, high p_T tracks that are highly ionising. No require-
¹⁴⁸⁴ ment on the number of tracker hits is enforced, thus, possibly very short tracks from early
¹⁴⁸⁵ decaying charginos are included in this analysis.

¹⁴⁸⁶ It, thus, extends the search for disappearing tracks [13] by the inclusion of the variable
¹⁴⁸⁷ dE/dx and the loosening of the requirement on the number of hits in the tracker ($N_{\text{hits}} \geq 3$)
¹⁴⁸⁸ that leads to a strong suppression of signal events for low chargino lifetimes (cf. Fig. 1.2.7).
¹⁴⁸⁹ It is thereby the first analysis at CMS that studies disappearing tracks with down to three

1490 hits.

1491 In order to increase the search sensitivity with respect to shorter lifetimes, energy infor-
 1492 mation from the pixel silicon tracker is taken into account. For this purpose, a dedicated
 1493 pixel energy calibration was carried out within this thesis to ensure stable energy mea-
 1494 surements over time and across pixel modules. This is thus the first time that an analysis
 1495 at CMS makes use of energy information from the pixel tracker. By adding pixel energy
 1496 information, the discrimination power of dE/dx is substantially increased (cf. Fig. 1.3.10).

1497

1498 The Standard Model background is mainly estimated with data-based techniques. The
 1499 main background to this search is arising from fake tracks, i. e. tracks that are reconstructed
 1500 out of the tracker hits of more than one particle. Fake tracks are typically short and can
 1501 have large values of I_{as} , thus showing a very signal-like signature in the detector. The
 1502 background contribution by leptons that are passing the lepton veto is very small and in
 1503 most of the signal regions almost negligible.

1504 In the current analysis, the background is estimated at 19 and 24 events in the low I_{as}
 1505 signal regions and 2.5 and 2.6 events in the high I_{as} regions. This background estimate is
 1506 confronted with collision data recorded during the year 2012 at the CMS experiment at
 1507 a centre-of-mass energy of 8 TeV. No evidence for physics beyond the Standard Model is
 1508 found. Thus, the absence of any deviation from the Standard Model prediction is used to
 1509 constrain the supersymmetric parameter space. Wino-like charginos are excluded down to
 1510 lifetimes of $c\tau = 2$ cm for $m_{\tilde{\chi}_1^\pm} = 100$ GeV. For high mass scenarios of $m_{\tilde{\chi}_1^\pm} = 500$ GeV, the
 1511 excluded lifetime ranges between $c\tau = 70 - 500$ cm. This confirms the parameter exclusion
 1512 limits of the search for disappearing tracks [13]. Interestingly, the signal regions of the
 1513 here presented search and the search from [13] show little overlap. Therefore, this analysis
 1514 yields a complementary result with respect to the search for disappearing tracks [13]. In
 1515 summary, the exclusion of SUSY models with respect to earlier searches could be indepen-
 1516 dently confirmed and improvements in the exclusions of around 10 – 40 GeV in chargino
 1517 mass in the low lifetime region are achieved.

1518

1519 While this analysis is able to exclude many SUSY models with intermediate lifetime
 1520 charginos, there are several promising avenues for even enhancing the search sensitivity.

1521 First, since the sensitivity of the current analysis is mainly limited by large systematic
 1522 uncertainties originating from low statistical precision in the simulated datasets, simulat-
 1523 ing more events could significantly improve the search sensitivity. This strategy is however
 1524 technically challenging, since storage capacity limits were already reached within the cur-
 1525 rent analysis. Still, reducing this systematic uncertainty will be one of the main tasks for
 1526 future research.

1527 Second, even though this search already features low background, a further background

suppression is desirable. However, the impact on the search sensitivity will be limited because of the high relative Poisson error on low background predictions. For instance, without considering systematic uncertainties (FIXME), a reduction of the number of background events by 50% from 2 to 1 reduces the signal yield required for a 5σ -discovery by around 8%, whereas a 50% reduction of expected background events from 200 to 100 reduces the required signal yield by 26%.

Thus, in order to improve the here presented analysis, the focus should be on the other determinant of search sensitivity: the signal acceptance. First and foremost, it is important to lower the signal losses due to trigger requirements. For this purpose, a dedicated track trigger is indispensable and it is very promising that such a trigger is included in Run II trigger menues.

Furthermore, an implementation of a dedicated track reconstruction algorithm optimised for short tracks could increase the reconstruction efficiency of possible chargino tracks, which is currently $\sim 20\text{--}40\%$ for chargino tracks with 3 – 4 hits. Additionally, a track reconstruction optimised for the reconstruction of soft particles that are not produced in the primary vertex could allow for a reconstruction of the Standard Model decay products of charginos, thereby enabling a better discrimination against Standard Model background.

In summary, the here presented analysis explored a new path for searching for long-lived charginos decaying early inside the detector. It is the first analysis that incorporates reconstructed tracks down to three hits. Furthermore, for the first time, ionisation losses are measured taking energy information from the pixel silicon tracker into account.

As argued, further improvements can allow for accessing new, unexplored SUSY models with long-lived charginos. Additionally, a search in collisions at a centre-of-mass energy of 13 TeV with increased cross sections makes the exploration of SUSY models with higher chargino masses possible. Since dE/dx is much more discriminating for high masses, the inclusion of dE/dx in this analysis will become even more powerful.

1556 **A Measurement of the jet transverse-momentum resolution**

1557

1558 **A.1 Pileup reweighting**

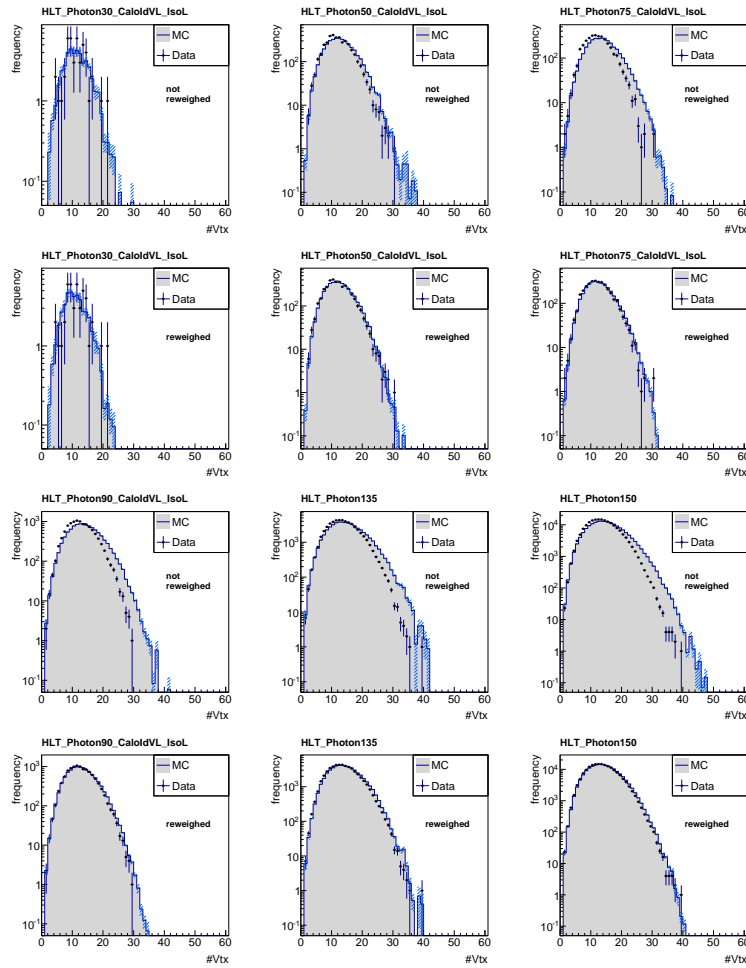


Figure A.1: The number of primary vertices in data and simulation before (1st row) and after (2nd row) pileup reweighting for $36 \text{ GeV} < p_T^\gamma < 60 \text{ GeV}$ (left), $60 \text{ GeV} < p_T^\gamma < 88 \text{ GeV}$ (middle), and $88 \text{ GeV} < p_T^\gamma < 105 \text{ GeV}$ (right) and the number of primary vertices in data and simulation before (3rd row) and after (4th row) pileup reweighting for $105 \text{ GeV} < p_T^\gamma < 149 \text{ GeV}$ (left), $149 \text{ GeV} < p_T^\gamma < 165 \text{ GeV}$ (middle), and $165 \text{ GeV} < p_T^\gamma < 180 \text{ GeV}$ (right).

¹⁵⁵⁹ **A.2 Summary of all selection requirements**

Table A.1: Summary of all selection criteria for the measurements of the jet transverse-momentum resolution with $\gamma + \text{jet}$ events.

| | |
|-----------------------|---|
| One jet with | $p_T > 10 \text{ GeV}$ Neutral hadron fraction < 0.90 Neutral electromagnetic fraction < 0.90 Number of constituents > 1 Charged hadron fraction > 0 Charged hadron multiplicity > 0 |
| One photon with | $p_T > 22 \text{ GeV}$ $ \eta < 1.3$ $\frac{H}{E} < 0.05$ $\sigma_{in\eta} < 0.013$ ECAL isolation $< 4.2 \text{ GeV} + 0.0060 \cdot p_T^\gamma$ HCAL isolation $< 2.2 \text{ GeV} + 0.0025 \cdot p_T^\gamma$ Track Isolation $< 2.0 \text{ GeV} + 0.0010 \cdot p_T^\gamma$ Pixel seed veto |
| Event-based selection | $p_T^{2\text{nd jet}} > 10 \text{ GeV}$ $\frac{p_T^{2\text{nd jet}}}{p_T^\gamma} < 0.20$ $\Delta\phi(1^{\text{st}} \text{ jet}, \gamma) > 2.95$ |

¹⁵⁶⁰ **A.3 Generator-level jet flavor definition**

¹⁵⁶¹ The algorithmic flavor definition uses the following discrimination:

- ¹⁵⁶² • Try to find the parton that most likely determines the properties of the jet and assign
¹⁵⁶³ that flavor as true flavor

- 1564 • Here, the “final state” partons (after showering, radiation) are analyzed (also within
1565 $\Delta R < 0.3$ of reconstructed jet cone)
- 1566 • Jets from radiation are matched with full efficiency
- 1567 • If there is a b/c within the jet cone: label as b/c
- 1568 • Otherwise: assign flavor of the hardest parton

1569 A.4 Extrapolation plots

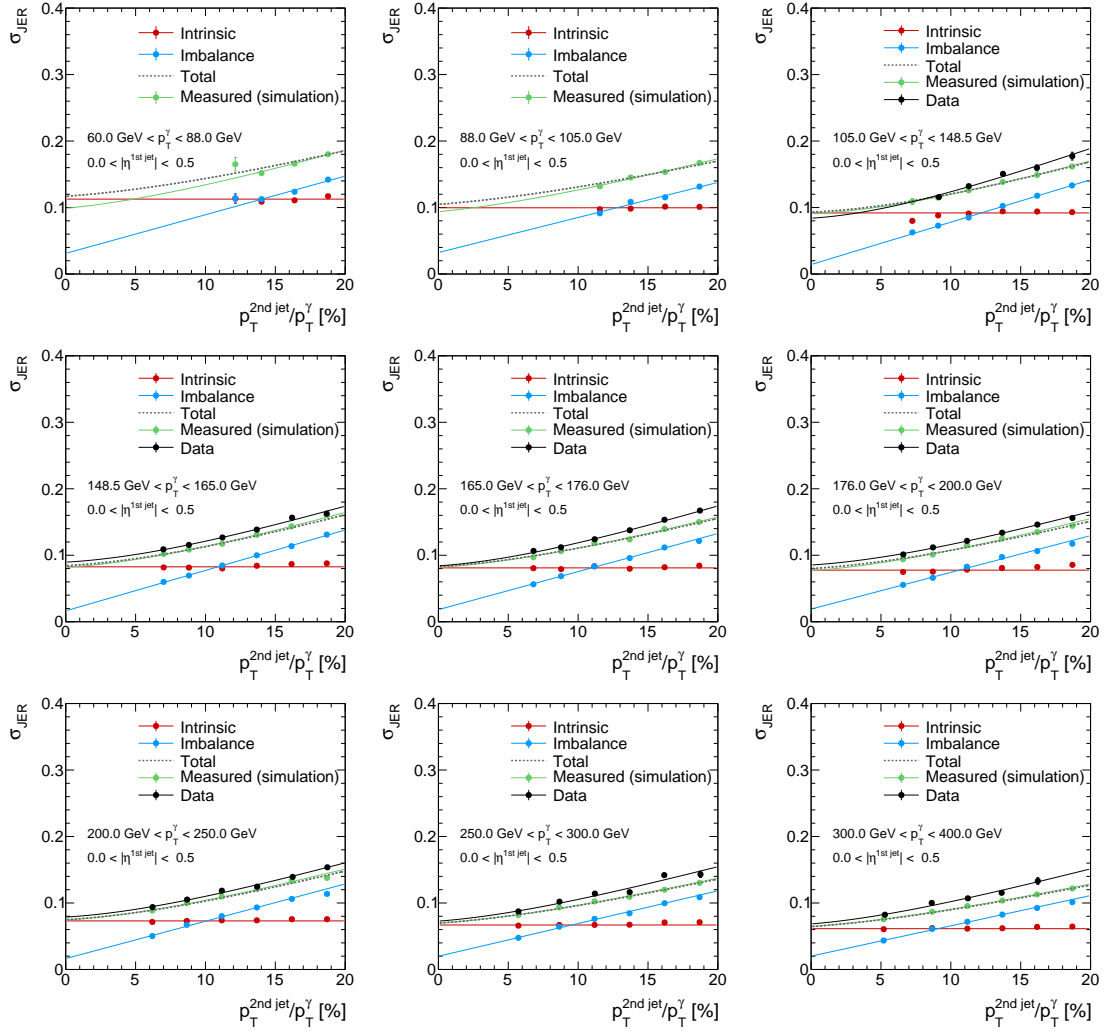


Figure A.2: σ_{JER} (α) of the intrinsic, imbalance and measured resolution in simulation and the resolution measured in data for all $|\eta^{1st\ jet}|$ and p_T^γ bins.

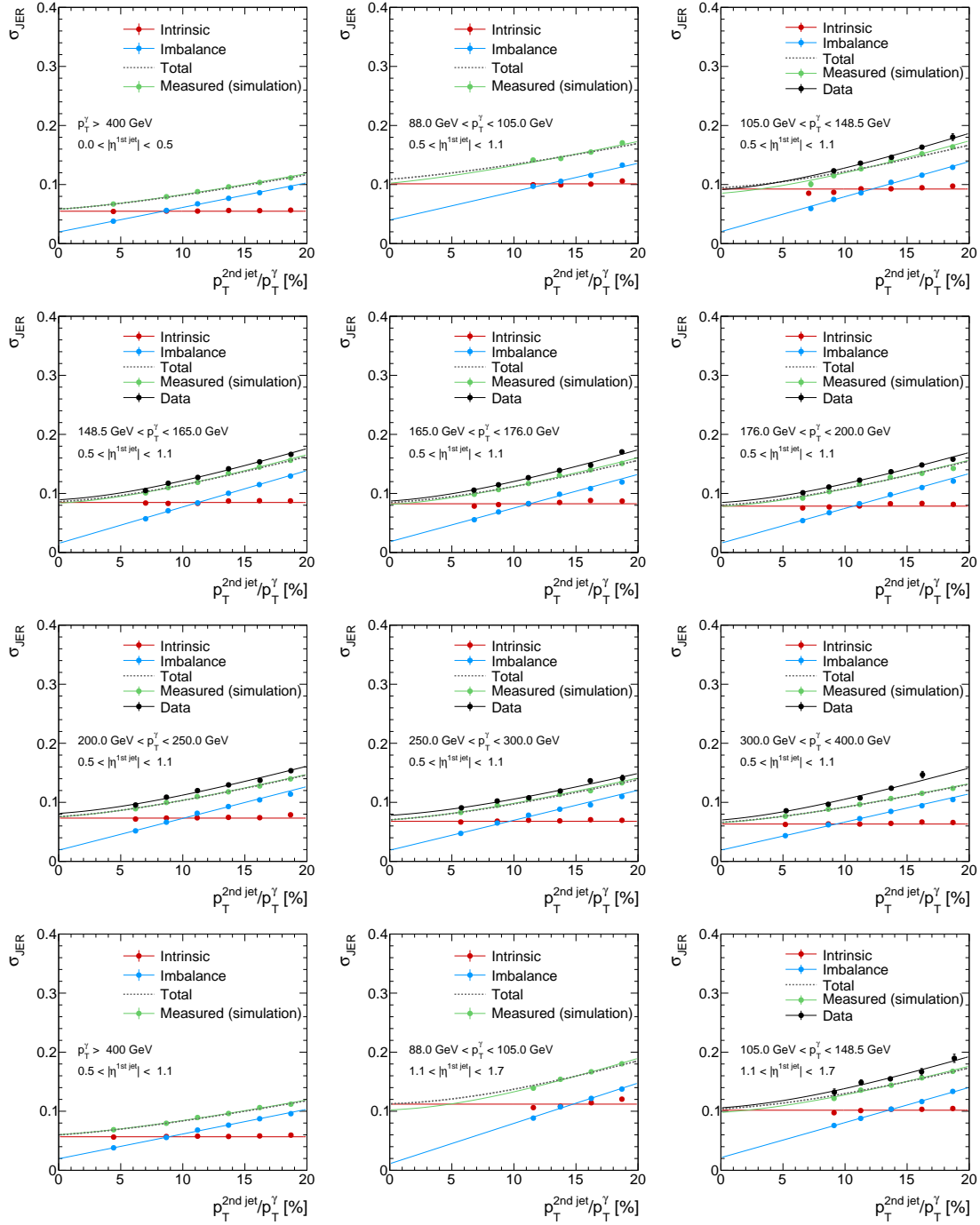


Figure A.3: Continued from Fig. A.2: σ_{JER} (α) of the intrinsic, imbalance and measured resolution in simulation and the resolution measured in data for all $|\eta^{\text{1st jet}}|$ and p_T^γ bins.

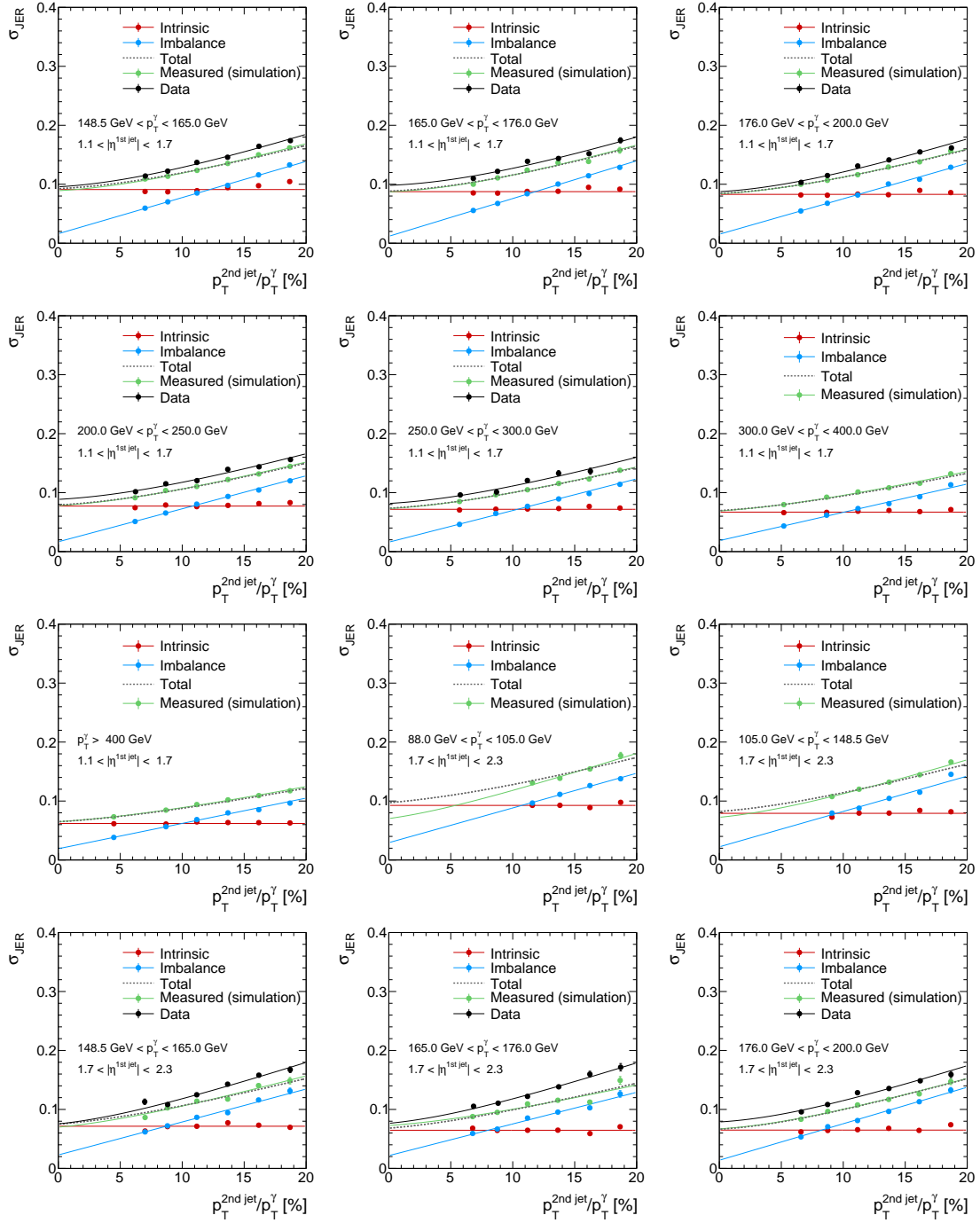


Figure A.4: Continued from Fig. A.3: σ_{JER} (α) of the intrinsic, imbalance and measured resolution in simulation and the resolution measured in data for all $|\eta^{\text{1st jet}}|$ and p_T^γ bins.

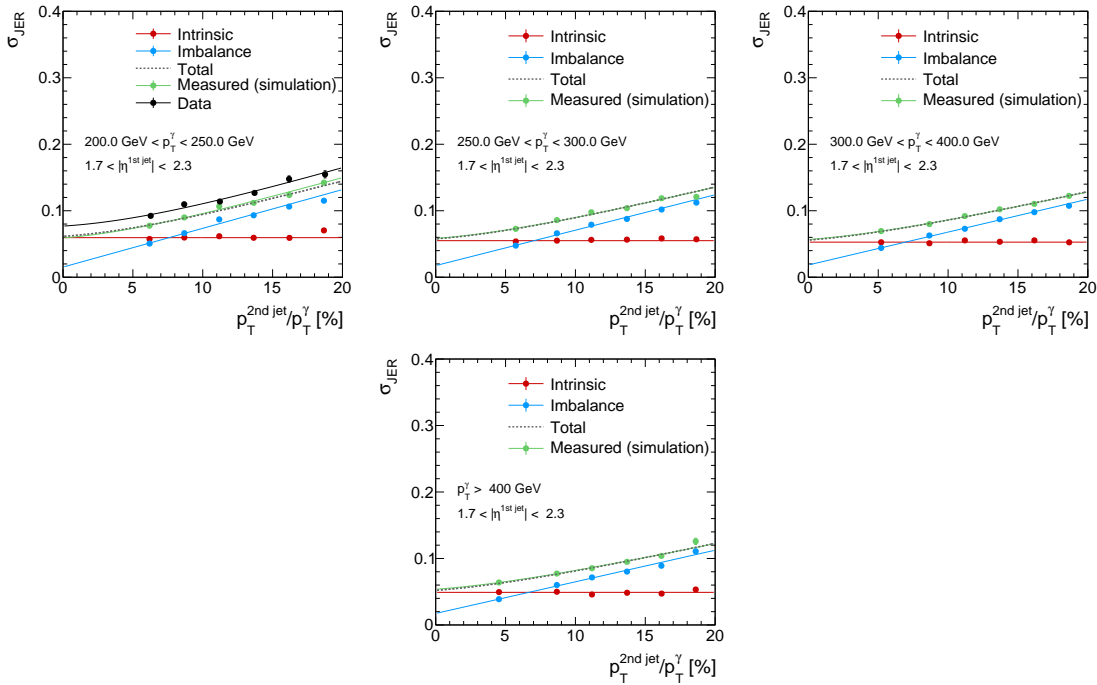


Figure A.5: Continued from Fig. A.4: σ_{JER} (α) of the intrinsic, imbalance and measured resolution in simulation and the resolution measured in data for all $|\eta^{\text{1st jet}}|$ and p_T^γ bins.

1570 B A search for highly ionising, short tracks

1571 B.1 Lifetime reweighting

1572 The probability density function of a particle's proper lifetime for a sample generated with
 1573 a particle's mean lifetime τ^{gen} is given by

$$p(t) = \frac{1}{\tau^{\text{gen}}} \cdot \exp \left[-\frac{t}{\tau^{\text{gen}}} \right].$$

1574 After carrying out the lifetime reweighting procedure, the targeted p.d.f of the particle's
 1575 new mean lifetime τ^{target} is given by

$$p'(t) = \frac{1}{\tau^{\text{target}}} \cdot \exp \left[-\frac{t}{\tau^{\text{target}}} \right].$$

1576 Thus, an event containing a particle with individual proper lifetime can be reweighted
1577 with the following weight

$$w = \frac{p'(t)}{p(t)} = \frac{\tau^{\text{gen}}}{\tau^{\text{target}}} \cdot \exp \left[\frac{t}{\tau^{\text{gen}}} - \frac{t}{\tau^{\text{target}}} \right].$$

1578 For more than one non-stable particle, the event weight is calculated by multiplying the
1579 weights of the single reweighting procedures.

1580 **B.2 Event yields for simulated samples and data**

Table B.1: Event yields after each selection step for various simulated background samples.

| Selection | $W + \text{jets}$ | $t\bar{t} + \text{jets}$ | $Z \rightarrow \ell\bar{\ell}$ | Multijet |
|--|-------------------|--------------------------|--------------------------------|----------------------|
| After skim | $9.16 \cdot 10^7$ | $1.04 \cdot 10^6$ | $2.21 \cdot 10^7$ | $1.38 \cdot 10^{11}$ |
| Trigger | $4.31 \cdot 10^6$ | $1.15 \cdot 10^5$ | $4.23 \cdot 10^3$ | $4.32 \cdot 10^6$ |
| $p_T^{\text{1st jet}} > 110 \text{ GeV}$ | $2.47 \cdot 10^6$ | $7.17 \cdot 10^4$ | $2.60 \cdot 10^3$ | $2.75 \cdot 10^6$ |
| $\cancel{E}_T > 100 \text{ GeV}$ | $1.89 \cdot 10^6$ | $5.31 \cdot 10^4$ | $6.26 \cdot 10^2$ | $9.63 \cdot 10^5$ |
| $\Delta\phi_{\max}(\text{jet}_i, \text{jet}_j) < 2.7$ | $1.11 \cdot 10^6$ | $6.81 \cdot 10^3$ | $1.32 \cdot 10^2$ | $2.01 \cdot 10^4$ |
| $\Delta\phi_{\max}(\text{jet}_i, \cancel{E}_T) > 0.5$ | $1.11 \cdot 10^6$ | $6.76 \cdot 10^3$ | $1.32 \cdot 10^2$ | $9.55 \cdot 10^3$ |
| ≥ 1 track in the event with: | $1.10 \cdot 10^6$ | $6.75 \cdot 10^3$ | $1.32 \cdot 10^2$ | $9.55 \cdot 10^3$ |
| high-purity | $1.10 \cdot 10^6$ | $6.74 \cdot 10^3$ | $1.32 \cdot 10^2$ | $9.55 \cdot 10^3$ |
| $N_{\text{miss}}^{\text{middle}} = 0$ | $1.09 \cdot 10^6$ | $6.72 \cdot 10^3$ | $1.32 \cdot 10^2$ | $9.55 \cdot 10^3$ |
| $N_{\text{miss}}^{\text{inner}} = 0$ | $1.07 \cdot 10^6$ | $6.70 \cdot 10^3$ | $1.32 \cdot 10^2$ | $9.55 \cdot 10^3$ |
| $ d0 < 0.02 \text{ cm}$ | $1.07 \cdot 10^6$ | $6.64 \cdot 10^3$ | $1.32 \cdot 10^2$ | $9.55 \cdot 10^3$ |
| $ dz < 0.5 \text{ cm}$ | $1.07 \cdot 10^6$ | $6.63 \cdot 10^3$ | $1.32 \cdot 10^2$ | $9.55 \cdot 10^3$ |
| $ \eta < 2.1$ | $1.03 \cdot 10^6$ | $6.58 \cdot 10^3$ | $1.32 \cdot 10^2$ | $9.55 \cdot 10^3$ |
| $p_T > 20 \text{ GeV}$ | $8.14 \cdot 10^5$ | $5.63 \cdot 10^3$ | $1.32 \cdot 10^2$ | $5.48 \cdot 10^3$ |
| No μ within $\Delta R < 0.15$ | $7.15 \cdot 10^5$ | $4.52 \cdot 10^3$ | $1.32 \cdot 10^2$ | $5.48 \cdot 10^3$ |
| No e within $\Delta R < 0.15$ | $6.69 \cdot 10^5$ | $3.67 \cdot 10^3$ | $7.86 \cdot 10^1$ | $5.48 \cdot 10^3$ |
| No τ within $\Delta R < 0.15$ | $6.62 \cdot 10^5$ | $3.61 \cdot 10^3$ | $7.86 \cdot 10^1$ | $5.47 \cdot 10^3$ |
| No jet within $\Delta R < 0.5$ | $1.18 \cdot 10^3$ | $1.44 \cdot 10^1$ | $1.09 \cdot 10^1$ | $0.00 \cdot 10^0$ |
| Not within $\Delta R < 0.05$ of a dead/noisy ECAL cell | $7.25 \cdot 10^2$ | $8.02 \cdot 10^0$ | $0.00 \cdot 10^0$ | $0.00 \cdot 10^0$ |
| Not within an ECAL intermodule gap | $7.15 \cdot 10^2$ | $8.02 \cdot 10^0$ | $0.00 \cdot 10^0$ | $0.00 \cdot 10^0$ |
| Not within $1.42 < \eta < 1.65$ | $5.89 \cdot 10^2$ | $6.53 \cdot 10^0$ | $0.00 \cdot 10^0$ | $0.00 \cdot 10^0$ |
| Not within $\Delta R < 0.25$ to a bad CSC | $5.02 \cdot 10^2$ | $5.88 \cdot 10^0$ | $0.00 \cdot 10^0$ | $0.00 \cdot 10^0$ |
| $\sum_{\Delta R < 0.3} p_T^{\text{trk}} / p_T^{\text{cand}} - 1 < 0.1$ | $4.46 \cdot 10^2$ | $4.78 \cdot 10^0$ | $0.00 \cdot 10^0$ | $0.00 \cdot 10^0$ |
| $E_{\text{calo}}^{\Delta R < 0.5} < 5 \text{ GeV}$ | $3.19 \cdot 10^1$ | $0.67 \cdot 10^0$ | $0.00 \cdot 10^0$ | $0.00 \cdot 10^0$ |
| $p_T > 30 \text{ GeV}$ | $3.19 \cdot 10^1$ | $0.67 \cdot 10^0$ | $0.00 \cdot 10^0$ | $0.00 \cdot 10^0$ |
| $I_{\text{as}} > 0.05$ | $1.68 \cdot 10^1$ | $0.16 \cdot 10^0$ | $0.00 \cdot 10^0$ | $0.00 \cdot 10^0$ |

Table B.2: Event yields after each selection step for various signal models.

| Selection | m=100 GeV $c\tau=10 \text{ cm}$ | m=100 GeV $c\tau=100 \text{ cm}$ | m=500 GeV $c\tau=10 \text{ cm}$ | m=500 GeV $c\tau=100 \text{ cm}$ |
|--|------------------------------------|-------------------------------------|------------------------------------|-------------------------------------|
| | | | | |
| Total | $3.41 \cdot 10^5$ | $3.41 \cdot 10^5$ | $3.46 \cdot 10^2$ | $3.46 \cdot 10^2$ |
| Trigger | $1.55 \cdot 10^4$ | $1.49 \cdot 10^4$ | $4.62 \cdot 10^1$ | $4.61 \cdot 10^1$ |
| $p_T^{1^{\text{st}} \text{ jet}} > 110 \text{ GeV}$ | $1.10 \cdot 10^4$ | $1.04 \cdot 10^4$ | $3.64 \cdot 10^1$ | $3.58 \cdot 10^1$ |
| $\cancel{E}_T > 100 \text{ GeV}$ | $1.09 \cdot 10^4$ | $9.82 \cdot 10^3$ | $3.63 \cdot 10^1$ | $3.56 \cdot 10^1$ |
| $\Delta\phi_{\max}(\text{jet}_i, \text{jet}_j) < 2.7$ | $7.90 \cdot 10^3$ | $7.03 \cdot 10^3$ | $2.76 \cdot 10^1$ | $2.71 \cdot 10^1$ |
| $\Delta\phi_{\max}(\text{jet}_i, \cancel{E}_T) > 0.5$ | $7.90 \cdot 10^3$ | $6.98 \cdot 10^3$ | $2.76 \cdot 10^1$ | $2.70 \cdot 10^1$ |
| ≥ 1 track in the event with: | $3.12 \cdot 10^3$ | $5.74 \cdot 10^3$ | $5.73 \cdot 10^0$ | $2.13 \cdot 10^1$ |
| high-purity | $2.90 \cdot 10^3$ | $5.66 \cdot 10^3$ | $5.24 \cdot 10^0$ | $2.08 \cdot 10^1$ |
| $N_{\text{miss}}^{\text{middle}} = 0$ | $2.86 \cdot 10^3$ | $5.46 \cdot 10^3$ | $5.23 \cdot 10^0$ | $2.02 \cdot 10^1$ |
| $N_{\text{miss}}^{\text{inner}} = 0$ | $2.85 \cdot 10^3$ | $5.41 \cdot 10^3$ | $5.22 \cdot 10^0$ | $2.01 \cdot 10^1$ |
| $ d0 < 0.02 \text{ cm}$ | $2.80 \cdot 10^3$ | $5.39 \cdot 10^3$ | $5.07 \cdot 10^0$ | $1.99 \cdot 10^1$ |
| $ dz < 0.5 \text{ cm}$ | $2.79 \cdot 10^3$ | $5.38 \cdot 10^3$ | $5.07 \cdot 10^0$ | $1.99 \cdot 10^1$ |
| $ \eta < 2.1$ | $2.63 \cdot 10^3$ | $4.98 \cdot 10^3$ | $5.01 \cdot 10^0$ | $1.91 \cdot 10^1$ |
| $p_T > 20 \text{ GeV}$ | $2.54 \cdot 10^3$ | $4.93 \cdot 10^3$ | $4.72 \cdot 10^0$ | $1.88 \cdot 10^1$ |
| No μ within $\Delta R < 0.15$ | $2.54 \cdot 10^3$ | $4.65 \cdot 10^3$ | $4.72 \cdot 10^0$ | $1.86 \cdot 10^1$ |
| No e within $\Delta R < 0.15$ | $2.54 \cdot 10^3$ | $4.65 \cdot 10^3$ | $4.72 \cdot 10^0$ | $1.86 \cdot 10^1$ |
| No τ within $\Delta R < 0.15$ | $2.54 \cdot 10^3$ | $4.64 \cdot 10^3$ | $4.72 \cdot 10^0$ | $1.86 \cdot 10^1$ |
| No jet within $\Delta R < 0.5$ | $2.53 \cdot 10^3$ | $4.60 \cdot 10^3$ | $4.63 \cdot 10^0$ | $1.82 \cdot 10^1$ |
| Not within $\Delta R < 0.05$ of a dead/noisy ECAL cell | $2.32 \cdot 10^3$ | $4.26 \cdot 10^3$ | $4.19 \cdot 10^0$ | $1.69 \cdot 10^1$ |
| Not within an ECAL intermodule gap | $2.30 \cdot 10^3$ | $4.23 \cdot 10^3$ | $4.16 \cdot 10^0$ | $1.67 \cdot 10^1$ |
| Not within $1.42 < \eta < 1.65$ | $2.09 \cdot 10^3$ | $3.88 \cdot 10^3$ | $3.94 \cdot 10^0$ | $1.56 \cdot 10^1$ |
| Not within $\Delta R < 0.25$ to a bad CSC | $1.98 \cdot 10^3$ | $3.67 \cdot 10^3$ | $3.82 \cdot 10^0$ | $1.50 \cdot 10^1$ |
| $\sum_{\Delta R < 0.3} p_T^{\text{trk}} / p_T^{\text{cand}} - 1 < 0.1$ | $1.96 \cdot 10^3$ | $3.64 \cdot 10^3$ | $3.78 \cdot 10^0$ | $1.49 \cdot 10^1$ |
| $E_{\text{calo}}^{\Delta R < 0.5} < 5 \text{ GeV}$ | $1.66 \cdot 10^3$ | $3.05 \cdot 10^3$ | $3.38 \cdot 10^0$ | $1.26 \cdot 10^1$ |
| $p_T > 30 \text{ GeV}$ | $1.53 \cdot 10^3$ | $2.98 \cdot 10^3$ | $2.94 \cdot 10^0$ | $1.23 \cdot 10^1$ |
| $I_{\text{as}} > 0.05$ | $8.18 \cdot 10^2$ | $1.47 \cdot 10^3$ | $2.52 \cdot 10^0$ | $1.07 \cdot 10^1$ |

Table B.3: Observed event yield after each selection step in data.

| Selection | MET dataset |
|--|-------------------|
| After skim | $1.07 \cdot 10^7$ |
| Trigger | $1.07 \cdot 10^7$ |
| $p_T^{1\text{st jet}} > 110 \text{ GeV}$ | $6.82 \cdot 10^6$ |
| $\cancel{E}_T > 100 \text{ GeV}$ | $3.94 \cdot 10^6$ |
| $\Delta\phi_{\max}(\text{jet}_i, \text{jet}_j) < 2.7$ | $1.39 \cdot 10^6$ |
| $\Delta\phi_{\max}(\text{jet}_{1,2}, \cancel{E}_T) > 0.5$ | $1.38 \cdot 10^6$ |
| ≥ 1 track in the event with: | |
| reconstructed trk | $1.37 \cdot 10^6$ |
| high-purity | $1.36 \cdot 10^6$ |
| $N_{\text{miss}}^{\text{middle}} = 0$ | $1.34 \cdot 10^6$ |
| $N_{\text{miss}}^{\text{inner}} = 0$ | $1.31 \cdot 10^6$ |
| $ d0 < 0.02 \text{ cm}$ | $1.30 \cdot 10^6$ |
| $ dz < 0.5 \text{ cm}$ | $1.30 \cdot 10^6$ |
| $ \eta < 2.1$ | $1.26 \cdot 10^6$ |
| $p_T > 20 \text{ GeV}$ | $9.51 \cdot 10^5$ |
| No μ within $\Delta R < 0.15$ | $8.40 \cdot 10^5$ |
| No e within $\Delta R < 0.15$ | $8.01 \cdot 10^5$ |
| No τ within $\Delta R < 0.15$ | $7.95 \cdot 10^5$ |
| No jet within $\Delta R < 0.5$ | $1.75 \cdot 10^3$ |
| Not within $\Delta R < 0.05$ of a dead/noisy ECAL cell | $9.11 \cdot 10^2$ |
| Not within an ECAL intermodule gap | $9.06 \cdot 10^2$ |
| Not within $1.42 < \eta < 1.65$ | $7.33 \cdot 10^2$ |
| Not within $\Delta R < 0.25$ to a bad CSC | $6.16 \cdot 10^2$ |
| $\sum_{\Delta R < 0.3} p_T^{\text{trk}} / p_T^{\text{cand}} - 1 < 0.1$ | $5.26 \cdot 10^2$ |
| $E_{\text{calo}}^{\Delta R < 0.5} < 5 \text{ GeV}$ | $1.19 \cdot 10^2$ |
| $p_T > 30 \text{ GeV}$ | $9.10 \cdot 10^1$ |
| $I_{\text{as}} > 0.05$ | $5.60 \cdot 10^1$ |

1581 B.3 Signal contamination in validation regions

1582 Signal contamination in the four validation regions from Section 1.6.3. The highest signal
 1583 contamination is visible for a lifetime of 100 cm for all signal masses. For higher lifetimes
 1584 the signal contamination is again reduced due to the muon veto selection requirement.
 1585 The most extreme values (from $c\tau = 100$ cm) of expected signal events and some other
 1586 selected signal models are shown in the following tables. The signal contamination is
 1587 rapidly falling towards lower lifetimes and higher masses.

Table B.4: Signal contamination in leptonic control region: $E_{\text{calo}}^{\Delta R < 0.5} > 10$ GeV and $N_{\text{hits}} > 6$. N_S is the number of expected signal events and ΔB is the statistical uncertainty on the background prediction.

| Signal model | N_S | $N_S/\Delta B$ | Excluded by [13] |
|--------------------------------|--------|----------------|------------------|
| mass=100 GeV, $c\tau = 100$ cm | 211.93 | 8.06 | yes |
| mass=100 GeV, $c\tau = 10$ cm | 27.83 | 1.06 | yes |
| mass=100 GeV, $c\tau = 5$ cm | 7.39 | 0.28 | yes |
| mass=100 GeV, $c\tau = 1$ cm | 0 | 0 | no |
| mass=300 GeV, $c\tau = 100$ cm | 6.97 | 0.26 | yes |
| mass=300 GeV, $c\tau = 10$ cm | 0.33 | 0.01 | yes |
| mass=300 GeV, $c\tau = 5$ cm | 0.0 | 0.0 | no |
| mass=500 GeV, $c\tau = 100$ cm | 0.72 | 0.03 | yes |
| mass=500 GeV, $c\tau = 10$ cm | 0.00 | 0.00 | no |

Table B.5: Signal contamination in leptonic control region: $E_{\text{calo}}^{\Delta R < 0.5} > 10 \text{ GeV}$, $N_{\text{hits}} > 6$ and $I_{\text{as}} > 0.2$. N_S is the number of expected signal events and ΔB is the statistical uncertainty on the background prediction.

| Signal model | N_S | $N_S/\Delta B$ | Excluded by [13] |
|--|-------|----------------|------------------|
| mass=100 GeV, $c\tau = 100 \text{ cm}$ | 24.11 | 48.21 | yes |
| mass=100 GeV, $c\tau = 10 \text{ cm}$ | 0.00 | 0.00 | yes |
| mass=300 GeV, $c\tau = 100 \text{ cm}$ | 2.03 | 4.06 | yes |
| mass=300 GeV, $c\tau = 10 \text{ cm}$ | 0.03 | 0.07 | yes |
| mass=300 GeV, $c\tau = 5 \text{ cm}$ | 0.0 | 0.0 | no |
| mass=500 GeV, $c\tau = 100 \text{ cm}$ | 0.38 | 0.75 | yes |
| mass=500 GeV, $c\tau = 10 \text{ cm}$ | 0.00 | 0.00 | no |

Table B.6: Signal contamination in fake+lepton control region: $E_{\text{calo}}^{\Delta R < 0.5} > 10 \text{ GeV}$. N_S is the number of expected signal events and ΔB is the statistical uncertainty on the background prediction.

| Signal model | N_S | $N_S/\Delta B$ | Excluded by [13] |
|--|--------|----------------|------------------|
| mass=100 GeV, $c\tau = 100 \text{ cm}$ | 257.33 | 7.69 | yes |
| mass=100 GeV, $c\tau = 10 \text{ cm}$ | 116.21 | 3.47 | yes |
| mass=100 GeV, $c\tau = 5 \text{ cm}$ | 48.07 | 1.44 | yes |
| mass=100 GeV, $c\tau = 1 \text{ cm}$ | 1.26 | 0.04 | no |
| mass=300 GeV, $c\tau = 100 \text{ cm}$ | 9.35 | 0.28 | yes |
| mass=300 GeV, $c\tau = 10 \text{ cm}$ | 2.20 | 0.07 | yes |
| mass=300 GeV, $c\tau = 5 \text{ cm}$ | 0.85 | 0.03 | no |
| mass=500 GeV, $c\tau = 100 \text{ cm}$ | 1.10 | 0.03 | yes |
| mass=500 GeV, $c\tau = 10 \text{ cm}$ | 0.15 | 0.00 | no |

Table B.7: Signal contamination in fake+lepton control region: $E_{\text{calo}}^{\Delta R < 0.5} > 10 \text{ GeV}$, and $I_{\text{as}} > 0.2$. N_S is the number of expected signal events and ΔB is the statistical uncertainty on the background prediction.

| Signal model | N_S | $N_S/\Delta B$ | Excluded by [13] |
|--|-------|----------------|------------------|
| mass=100 GeV, $c\tau = 100 \text{ cm}$ | 36.40 | 12.47 | yes |
| mass=100 GeV, $c\tau = 10 \text{ cm}$ | 5.22 | 1.79 | yes |
| mass=100 GeV, $c\tau = 5 \text{ cm}$ | 1.76 | 0.60 | yes |
| mass=300 GeV, $c\tau = 100 \text{ cm}$ | 3.20 | 1.10 | yes |
| mass=300 GeV, $c\tau = 10 \text{ cm}$ | 0.58 | 0.20 | yes |
| mass=300 GeV, $c\tau = 5 \text{ cm}$ | 0.12 | 0.04 | no |
| mass=500 GeV, $c\tau = 100 \text{ cm}$ | 0.63 | 0.22 | yes |
| mass=500 GeV, $c\tau = 10 \text{ cm}$ | 0.07 | 0.02 | no |

1588 B.4 Validation tests of the background estimation methods

Table B.8: Validation tests of the background estimation methods in the calorimeter isolation control region $E_{\text{calo}}^{\Delta R < 0.5} > 10 \text{ GeV}$ for two different p_T selection requirements: $p_T > 40 \text{ GeV}$ (left) and $p_T > 60 \text{ GeV}$ (right). Only statistical uncertainties are included.

| | Predicted Yield | Data Yield | | Predicted Yield | Data Yield |
|-----------|---------------------------|------------|-----------|--------------------------|------------|
| Total bkg | $85.56^{+16.64}_{-11.14}$ | 94 | Total bkg | $35.83^{+12.02}_{-6.33}$ | 53 |
| Electrons | $15.69^{+11.92}_{-6.72}$ | | Electrons | $0.00^{+9.14}_{-0.00}$ | |
| Muons | $5.67^{+7.74}_{-3.55}$ | | Muons | $3.65^{+4.98}_{-2.28}$ | |
| Taus | $35.78^{+5.09}_{-4.18}$ | | Taus | $13.22^{+1.88}_{-1.55}$ | |
| Fakes | $28.42^{+6.99}_{-6.99}$ | | Fakes | $18.97^{+5.70}_{-5.70}$ | |

Table B.9: Validation tests of the background estimation methods in the calorimeter isolation control region $E_{\text{calo}}^{\Delta R < 0.5} > 10 \text{ GeV}$ with an additional I_{as} selection of $I_{\text{as}} > 0.2$ for two different p_{T} selection requirements: $p_{\text{T}} > 40 \text{ GeV}$ (left) and $p_{\text{T}} > 60 \text{ GeV}$ (right). Only statistical uncertainties are included.

| | Predicted Yield | Data Yield | | Predicted Yield | Data Yield |
|-----------|------------------------|------------|-----------|------------------------|------------|
| Total bkg | $4.94^{+1.49}_{-1.47}$ | 8 | Total bkg | $2.35^{+0.99}_{-0.97}$ | 3 |
| Electrons | $0.20^{+0.17}_{-0.10}$ | | Electrons | $0.00^{+0.11}_{-0.00}$ | |
| Muons | $0.00^{+0.22}_{-0.00}$ | | Muons | $0.00^{+0.14}_{-0.00}$ | |
| Taus | $0.48^{+0.15}_{-0.11}$ | | Taus | $0.18^{+0.06}_{-0.04}$ | |
| Fakes | $4.26^{+1.46}_{-1.46}$ | | Fakes | $2.17^{+0.97}_{-0.97}$ | |

Table B.10: Validation tests of the background estimation methods in the calorimeter isolation control region $E_{\text{calo}}^{\Delta R < 0.5} > 10 \text{ GeV}$ with an additional I_{as} selection of $I_{\text{as}} > 0.4$ for two different p_{T} selection requirements: $p_{\text{T}} > 40 \text{ GeV}$ (left) and $p_{\text{T}} > 60 \text{ GeV}$ (right). Only statistical uncertainties are included.

| | Predicted Yield | Data Yield | | Predicted Yield | Data Yield |
|-----------|------------------------|------------|-----------|------------------------|------------|
| Total bkg | $2.07^{+0.91}_{-0.88}$ | 2 | Total bkg | $1.11^{+0.64}_{-0.62}$ | 1 |
| Electrons | $0.00^{+0.05}_{-0.00}$ | | Electrons | $0.00^{+0.00}_{-0.00}$ | |
| Muons | $0.00^{+0.22}_{-0.00}$ | | Muons | $0.00^{+0.14}_{-0.00}$ | |
| Taus | $0.08^{+0.09}_{-0.04}$ | | Taus | $0.03^{+0.03}_{-0.02}$ | |
| Fakes | $1.99^{+0.87}_{-0.87}$ | | Fakes | $1.08^{+0.62}_{-0.62}$ | |

1589 The underprediction in the control regions with $I_{\text{as}} > 0.2$ is caused by the prediction
 1590 of the leptonic I_{as} shape from simulation. This leads to a bias as the I_{as} distribution in
 1591 simulation is softer than in data. However, this bias is taken into account as systematic
 1592 uncertainty (see Section 1.6.4.4).

1593 B.5 Selection requirements of the “tag-and-probe” samples

Table B.11: Event selection cuts for the muon “tag-and-probe” samples (T&P signal region sample and T&P lepton veto inverted control region sample) that are used to estimate the uncertainty on the muon scale factor ρ_{MC}^{μ} .

| | |
|---------------------------|---|
| Muon selection | $p_{\text{T}} > 25 \text{ GeV}$ $ \eta < 2.4$ $\sum_{\Delta R < 0.4} p_{\text{T}}^{\text{PF particle}} / p_{\text{T}}(\mu) < 0.12$ $\left. \frac{\chi^2}{ndof} \right _{\text{global track}} < 10$ $ d0 < 0.2 \text{ cm}$ $ dz < 0.5 \text{ cm}$ $\geq 1 \text{ hit in the muon detector}$ $\geq 2 \text{ hits in different muon detector planes}$ $\geq 1 \text{ hit in the pixel detector}$ $\geq 6 \text{ hits in the tracker system}$ |
| Candidate track selection | Good quality selection Kinematic selection Lepton/jet veto (μ veto inverted for the “tag-and-probe” control region) Isolation selection $N_{\text{hits}} > 5$ |
| Event-based selection | Muon and candidate track opposite in charge $80 \text{ GeV} < M_{\text{inv}}(\mu, \text{can. trk}) < 100 \text{ GeV}$ |

Table B.12: Event selection cuts for the tau “tag-and-probe” samples (T&P signal region sample and T&P lepton veto inverted control region sample) that are used to estimate the uncertainty on the tau scale factor ρ_{MC}^{τ} .

| | |
|---|---|
| Muon selection that is compatible with a $\tau \rightarrow \mu\nu\nu$ decay | $p_T > 25 \text{ GeV}$ |
| | $ \eta < 2.4$ |
| | $\sum_{\Delta R < 0.4} p_T^{\text{PF particle}} / p_T(\mu) < 0.12$ |
| | $\frac{\chi^2}{ndof} \Big _{\text{global track}} < 10$ |
| | $ d0 < 0.2 \text{ cm}$ |
| | $ dz < 0.5 \text{ cm}$ |
| | ≥ 1 hit in the muon detector |
| | ≥ 2 hits in different muon detector planes |
| | ≥ 1 hit in the pixel detector |
| | ≥ 6 hits in the tracker system |
| Candidate track selection | Good quality selection |
| | Kinematic selection |
| | Lepton/jet veto (τ veto inverted for the “tag-and-probe” control region) |
| | $\sum_{\Delta R < 0.3} p_T^{\text{trk}} / p_T^{\text{cand}} - 1 < 0.1$ |
| | $N_{\text{hits}} > 5$ |
| Event-based selection | Muon and candidate track opposite in charge |
| | $40 \text{ GeV} < M_{\text{inv}}(\mu, \text{cand. trk}) < 75 \text{ GeV}$ |
| | $m_T(\mu, \cancel{E}_T) < 40 \text{ GeV}$ |

Table B.13: Event selection cuts for the electron “tag-and-probe” samples (T&P signal region sample and T&P lepton veto inverted control region sample) that are used to estimate the uncertainty on the electron scale factor ρ_{MC}^e .

| | |
|---------------------------|---|
| Electron selection | $p_T > 25 \text{ GeV}$ |
| | $ \eta < 2.5$ |
| | $\sum_{\Delta R < 0.4} p_T^{\text{PF particle}} / p_T(e) < 0.15$ |
| | pass conversion veto |
| | no missing tracker hits |
| | good MVA electron as defined in [45] |
| Candidate track selection | Good quality selection |
| | Kinematic selection |
| | Lepton/jet veto (e veto inverted for the “tag-and-probe” control region) |
| | $\sum_{\Delta R < 0.3} p_T^{\text{trk}} / p_T^{\text{cand}} - 1 < 0.1$ |
| | $N_{\text{hits}} > 5$ |
| Event-based selection | Electron and candidate track opposite in charge $80 \text{ GeV} < M_{\text{inv}}(e, \text{cand. trk}) < 100 \text{ GeV}$ |

1594 B.6 Optimisation results with the number of missing outer hits

1595 Also an optimisation in the number of missing outer hits is performed. No significant im-
 1596 provement is visible in the search sensitivity for different selection requirements of $N_{\text{lost}}^{\text{outer}}$,
 see Fig. B.1. This is caused by the fact, that the main background, the fake background,

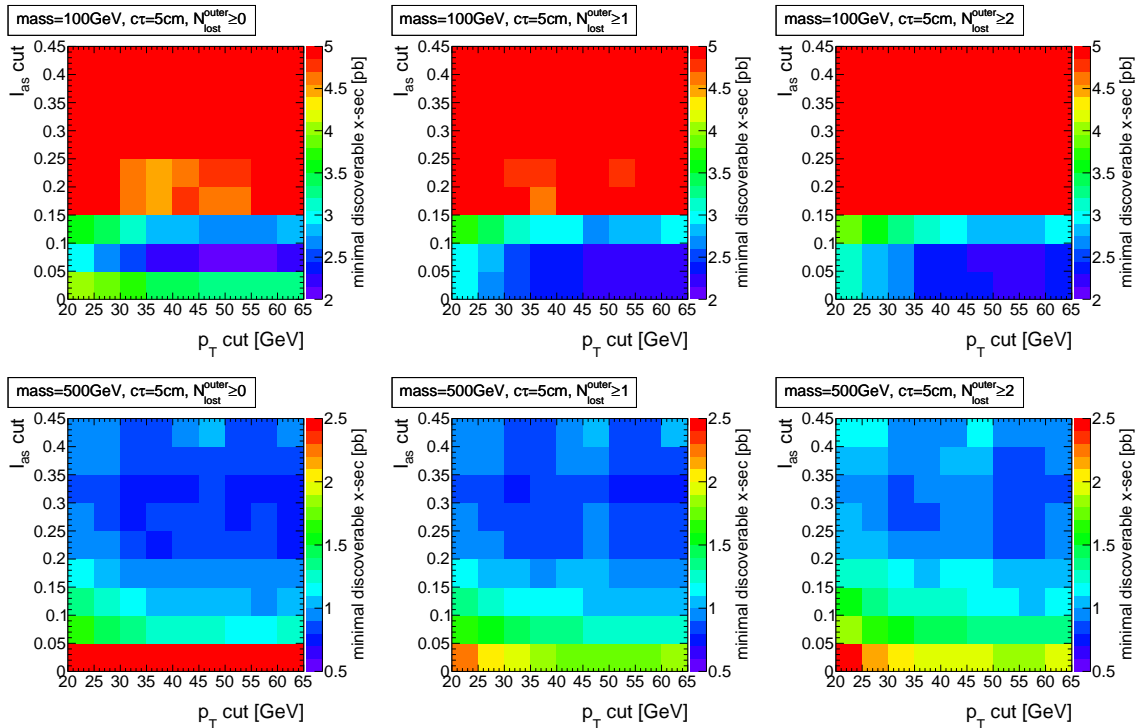


Figure B.1: Minimum possible cross section that can be discovered with 5σ significance in the $I_{\text{as}} - p_{\text{T}}$ plane for two different signal models with a chargino lifetime of 5 cm and a mass of 100 GeV (top) and 500 GeV (bottom). The requirement on the number of missing outer hits is varied between $N_{\text{lost}}^{\text{outer}} > 0$ (left), $N_{\text{lost}}^{\text{outer}} > 1$ (middle) and $N_{\text{lost}}^{\text{outer}} > 2$ (right). A difference in the sensitivity can be spotted when looking at the lowest value of the minimal discoverable cross section that occurs. No sizable discrimination improvement is visible for a tighter selection in $N_{\text{lost}}^{\text{outer}}$.

1597
 1598 also shows missing outer hits. A comparison between the number of missing outer hits for
 1599 the fake background and two signal models is shown in Fig. B.2.

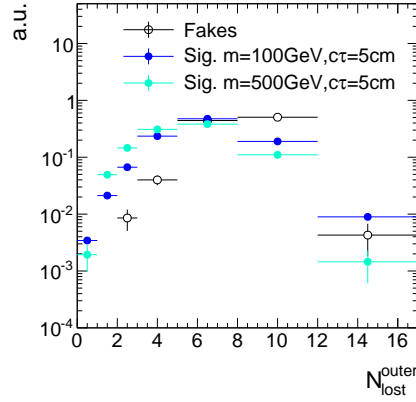


Figure B.2: Normalised distribution of the number of missing outer hits for fake tracks and two different signal models.

1600 B.7 Underlying distributions for the qualitative search sensitivity 1601 optimisation

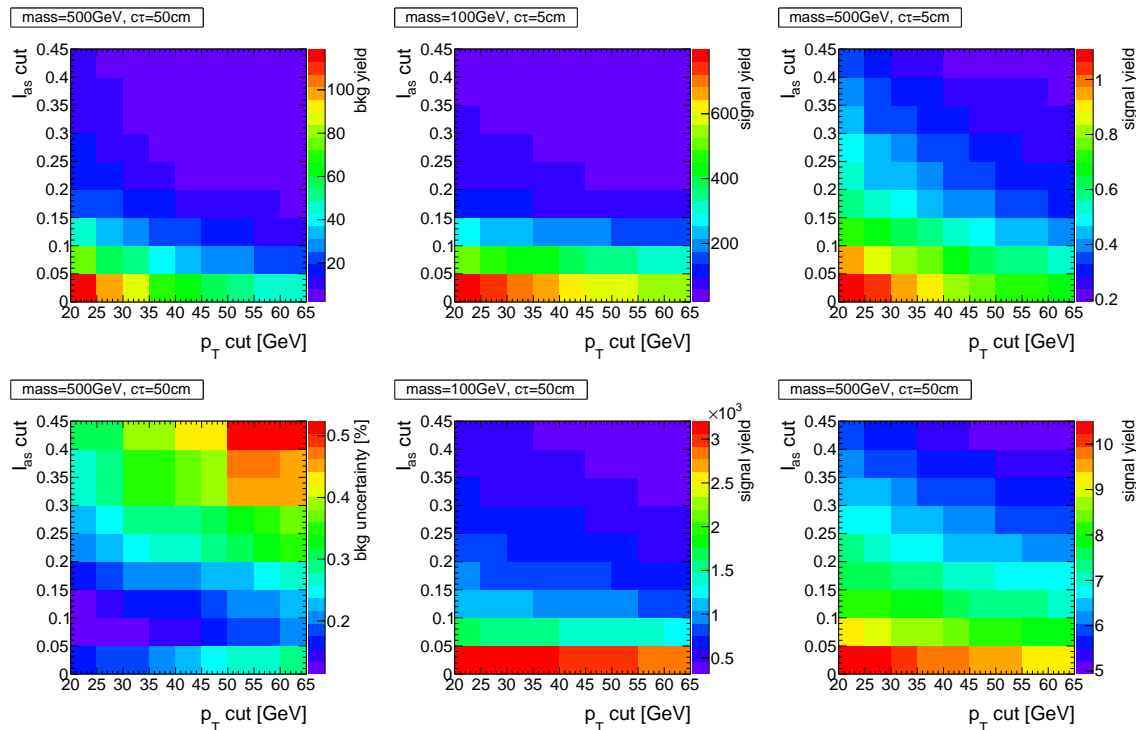


Figure B.3: Background yield, background uncertainty and signal yield for different p_T and I_{as} selection requirements and four different signal models.

¹⁶⁰² B.8 Trigger emulation

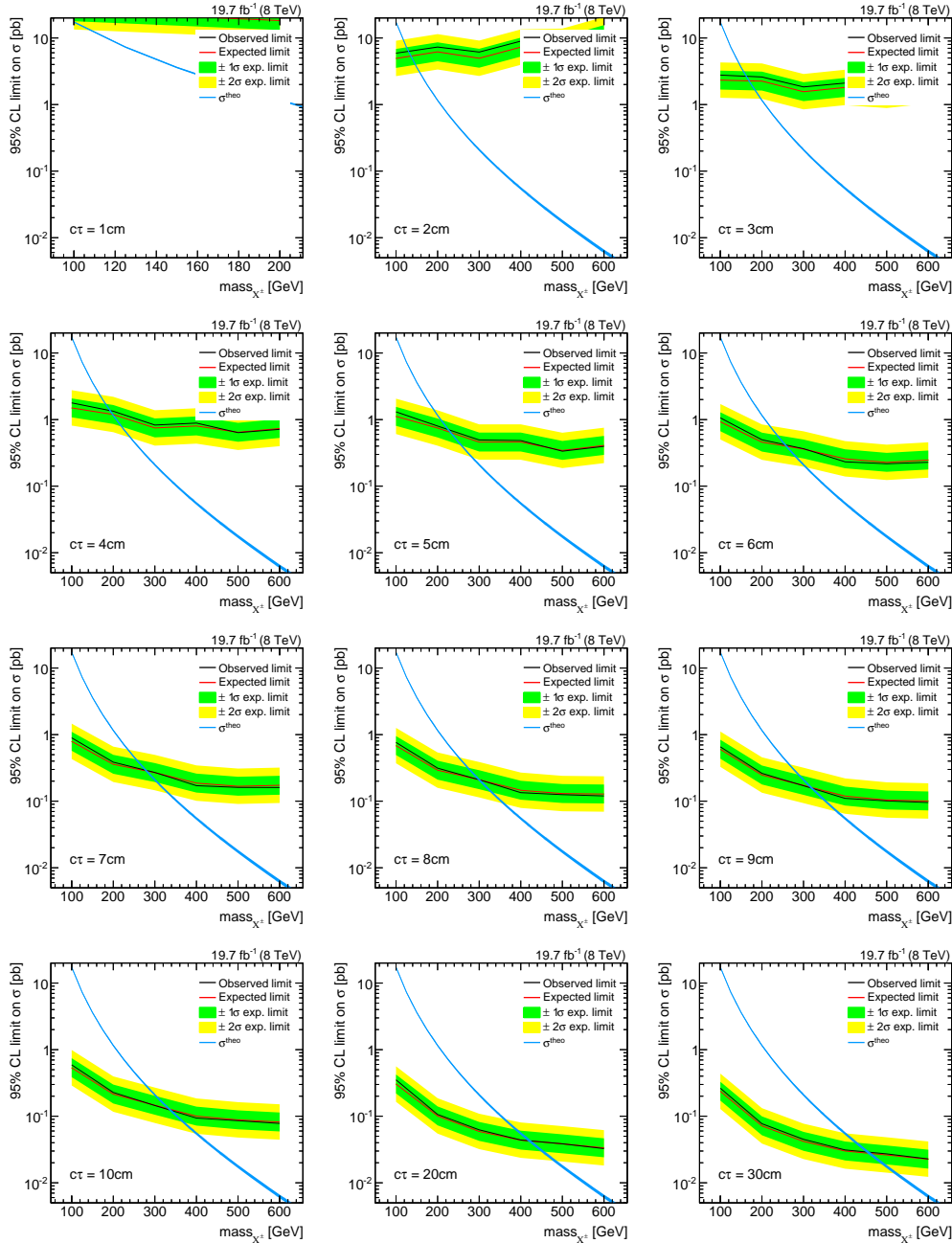
¹⁶⁰³ As the HLT_{MonoCentral}PFJet80_PFMETnoMu105_NHEF0p95 trigger is not available in
¹⁶⁰⁴ the simulated signal samples, this trigger is emulated in these samples. Since HLT trigger
¹⁶⁰⁵ information is stored in the samples, it is possible to rebuild the trigger afterwards.

¹⁶⁰⁶ The following requirements must be fulfilled in order to consider the trigger firing [39,40]:

- ¹⁶⁰⁷ • p_T of hltL1sL1ETM40 > 40 GeV
- ¹⁶⁰⁸ • p_T of hltCentralJet65L1FastJet > 65 GeV
- ¹⁶⁰⁹ • p_T of hltMET65 > 65 GeV
- ¹⁶¹⁰ • p_T of hltCentralPFJet80 > 80 GeV
- ¹⁶¹¹ • p_T of hltPFMETWOM95 > 105 GeV

¹⁶¹² As a cross check, also the HLT_{MonoCentral}PFJet80_PFMETnoMu95_NHEF0p95 is re-
¹⁶¹³ build with the looser selection of p_T of hltPFMETWOM95 > 95 GeV. The correct imple-
¹⁶¹⁴ mentation could be verified with this test.

¹⁶¹⁵ B.9 Exclusion limits for all simulated lifetimes

Figure B.4: 95% CL exclusion limits for signal models with $c\tau = 1 - 30 \text{ cm}$.

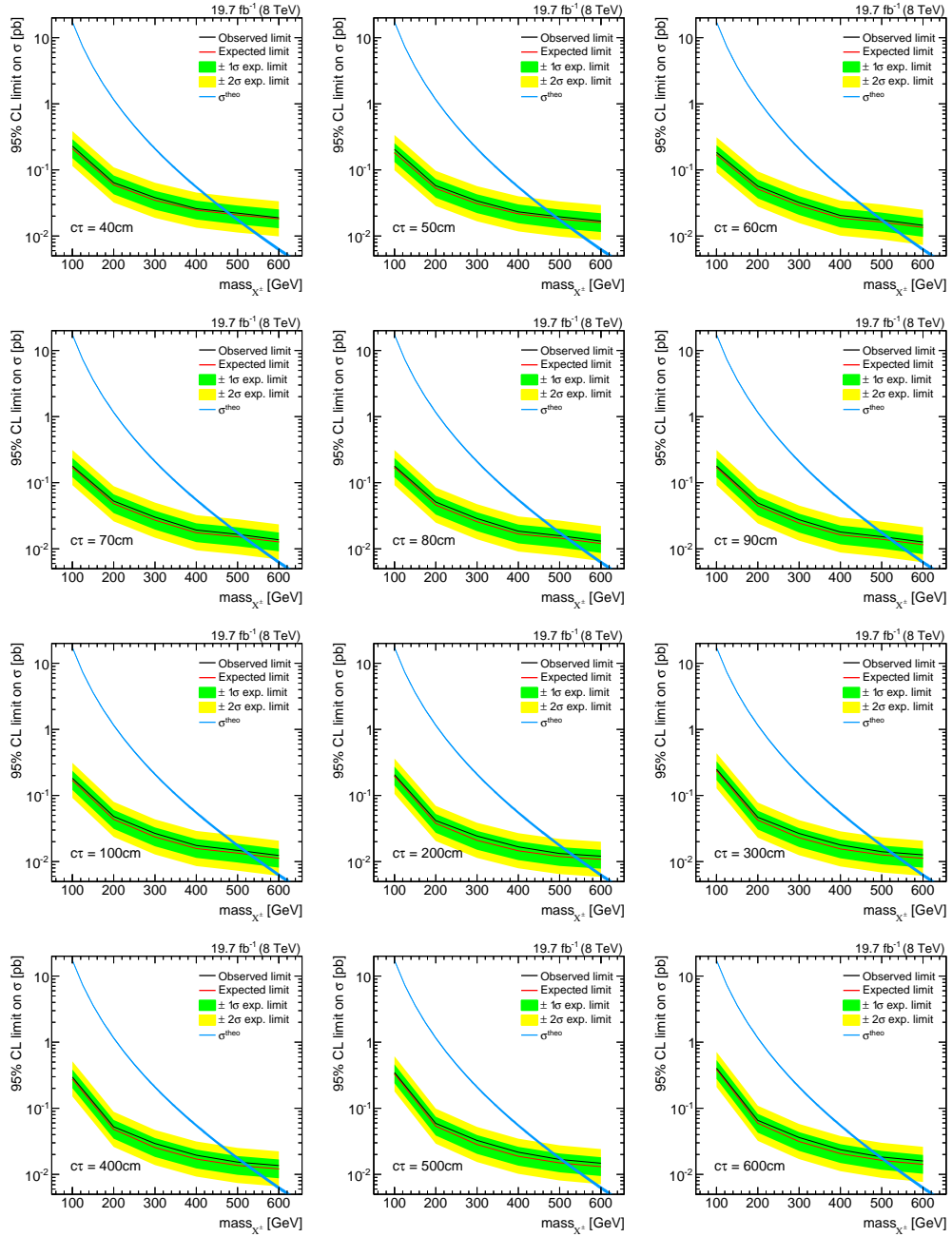
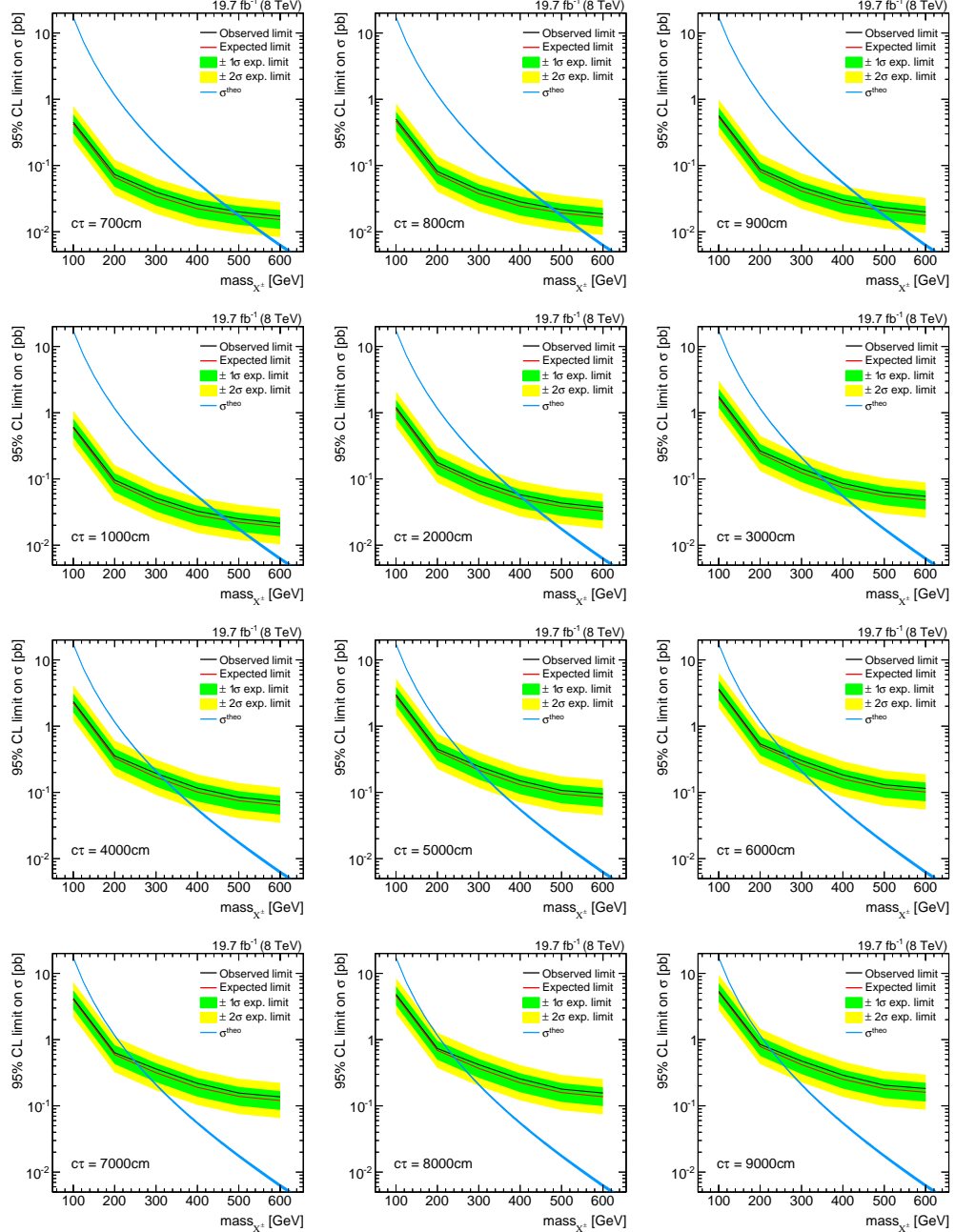


Figure B.5: 95% CL exclusion limits for signal models with $c\tau = 40 - 600$ cm.

Figure B.6: 95% CL exclusion limits for signal models with $c\tau = 700 - 9000$ cm.

1616 Bibliography

- 1617 [1] CDF, D0 Collaboration, T. Adams, “SUSY Searches at the Tevatron”, in *Hadron*
1618 *collider physics. Proceedings, 19th Symposium, HCP2008, Galena, USA, May 27-31,*
1619 *2008.* 2008. arXiv:0808.0728.
- 1620 [2] ALEPH, DELPHI, L3 and OPAL Collaborations, “Joint SUSY Working Group”.
1621 <http://lepsusy.web.cern.ch/lepsusy>. LEPSUSYWG (June 2004).
- 1622 [3] CMS Collaboration, “Search for new physics in the multijet and missing transverse
1623 momentum final state in proton-proton collisions at $\sqrt{s} = 8$ TeV”, *JHEP* **06** (2014)
1624 055, arXiv:1402.4770. doi:10.1007/JHEP06(2014)055.
- 1625 [4] CMS Collaboration, “Searches for Supersymmetry using the M_{T2} Variable in
1626 Hadronic Events Produced in pp Collisions at 8 TeV”, *JHEP* **05** (2015) 078,
1627 arXiv:1502.04358. doi:10.1007/JHEP05(2015)078.
- 1628 [5] ATLAS Collaboration, “Search for squarks and gluinos with the ATLAS detector in
1629 final states with jets and missing transverse momentum using $\sqrt{s} = 8$ TeV
1630 proton–proton collision data”, *JHEP* **09** (2014) 176, arXiv:1405.7875.
1631 doi:10.1007/JHEP09(2014)176.
- 1632 [6] M. Ibe, S. Matsumoto, S. Shirai et al., “Wino Dark Matter in light of the AMS-02
1633 2015 Data”, *Phys. Rev.* **D91** (2015), no. 11, 111701, arXiv:1504.05554.
1634 doi:10.1103/PhysRevD.91.111701.
- 1635 [7] J. Hisano, S. Matsumoto, M. M. Nojiri et al., “Direct detection of the Wino and
1636 Higgsino-like neutralino dark matters at one-loop level”, *Phys. Rev.* **D71** (2005)
1637 015007, arXiv:hep-ph/0407168. doi:10.1103/PhysRevD.71.015007.
- 1638 [8] T. Moroi and L. Randall, “Wino cold dark matter from anomaly mediated SUSY
1639 breaking”, *Nucl. Phys.* **B570** (2000) 455–472, arXiv:hep-ph/9906527.
1640 doi:10.1016/S0550-3213(99)00748-8.
- 1641 [9] T. Moroi, M. Nagai, and M. Takimoto, “Non-Thermal Production of Wino Dark
1642 Matter via the Decay of Long-Lived Particles”, *JHEP* **07** (2013) 066,
1643 arXiv:1303.0948. doi:10.1007/JHEP07(2013)066.

- 1644 [10] G. F. Giudice, M. A. Luty, H. Murayama et al., “Gaugino mass without singlets”,
 1645 *JHEP* **12** (1998) 027, [arXiv:hep-ph/9810442](#).
 1646 [doi:10.1088/1126-6708/1998/12/027](#).
- 1647 [11] L. Randall and R. Sundrum, “Out of this world supersymmetry breaking”, *Nucl.*
 1648 *Phys.* **B557** (1999) 79–118, [arXiv:hep-th/9810155](#).
 1649 [doi:10.1016/S0550-3213\(99\)00359-4](#).
- 1650 [12] A. Anandakrishnan, L. M. Carpenter, and S. Raby, “Degenerate gaugino mass
 1651 region and mono-boson collider signatures”, *Phys. Rev.* **D90** (2014), no. 5, 055004,
 1652 [arXiv:1407.1833](#). [doi:10.1103/PhysRevD.90.055004](#).
- 1653 [13] CMS Collaboration, “Search for disappearing tracks in proton-proton collisions at
 1654 $\sqrt{s} = 8$ TeV”, *JHEP* **01** (2015) 096, [arXiv:1411.6006](#).
 1655 [doi:10.1007/JHEP01\(2015\)096](#).
- 1656 [14] CMS Collaboration, “Searches for long-lived charged particles in pp collisions at
 1657 $\sqrt{s}=7$ and 8 TeV”, *JHEP* **07** (2013) 122, [arXiv:1305.0491](#).
 1658 [doi:10.1007/JHEP07\(2013\)122](#).
- 1659 [15] CMS Collaboration, “Phenomenological MSSM interpretation of the CMS 2011
 1660 5fb-1 results”, *CMS Physics Analysis Summary CMS-PAS-SUS-12-030* (2013).
- 1661 [16] CMS Collaboration, “Reinterpreting the results of the search for long-lived charged
 1662 particles in the pMSSM and other BSM scenarios”, *CMS Physics Analysis*
 1663 *Summary CMS-PAS-EXO-13-006* (2014).
- 1664 [17] CMS Collaboration, “Search for disappearing tracks in proton-proton collisions at
 1665 $\sqrt{s} = 8$ TeV”, *Public CMS Wiki* (2015).
 1666 <https://twiki.cern.ch/twiki/bin/view/CMS/PhysicsResultsEXO12034>, Topic
 1667 revision: r9.
- 1668 [18] CMS Collaboration, “Search for heavy long-lived charged particles in pp collisions at
 1669 $\sqrt{s} = 7$ TeV”, *Phys. Lett.* **B713** (2012) 408–433, [arXiv:1205.0272](#).
 1670 [doi:10.1016/j.physletb.2012.06.023](#).
- 1671 [19] CMS Collaboration, “Description and performance of track and primary-vertex
 1672 reconstruction with the CMS tracker”, *JINST* **9** (2014), no. 10, P10009,
 1673 [arXiv:1405.6569](#). [doi:10.1088/1748-0221/9/10/P10009](#).
- 1674 [20] H. Bethe, “Theory of the Passage of Fast Corpuscular Rays Through Matter”,
 1675 *Annalen Phys.* **5** (1930) 325–400. [Annalen Phys.397,325(1930)].
 1676 [doi:10.1002/andp.19303970303](#).

- 1677 [21] “National Institute of Standards and Technology”.
1678 <http://physics.nist.gov/cgi-bin/Star/compos.pl?mode=text&matno=014>.
1679 Accessed: 2015-10-21.
- 1680 [22] Particle Data Group Collaboration, “Review of Particle Physics”, *Chin. Phys. C* **38**
1681 (2014) 090001. doi:10.1088/1674-1137/38/9/090001.
- 1682 [23] L. Landau, “On the energy loss of fast particles by ionization”, *J. Phys.(USSR)* **8**
1683 (1944) 201–205.
- 1684 [24] H. Bichsel, “Straggling in Thin Silicon Detectors”, *Rev. Mod. Phys.* **60** (1988)
1685 663–699. doi:10.1103/RevModPhys.60.663.
- 1686 [25] L. Quertenmont, “Search for Heavy Stable Charged Particles with the CMS
1687 detector at the LHC”. PhD thesis, Louvain, U., 2010.
1688 <https://inspirehep.net/record/1088192/files/openfile.pdf>.
- 1689 [26] D. Kotlinski. personal communication.
- 1690 [27] T. W. Anderson, “On the Distribution of the Two-Sample Cramr-von Mises
1691 Criterion”, *The Annals of Mathematical Statistics* **33** (1962), no. 3, pp. 1148–1159.
- 1692 [28] F. James, “Statistical methods in experimental physics”. 2006.
- 1693 [29] CMS Collaboration, “Tracking and Vertexing Results from First Collisions”, *CMS
1694 Physics Analysis Summary CMS-PAS-TRK-10-001* (2010).
- 1695 [30] CMS Collaboration, “Data Formats and Data Tiers”, *Public CMS Wiki*.
1696 <https://twiki.cern.ch/twiki/bin/view/CMSPublic/WorkBookDataFormats>, Topic
1697 revision: r30.
- 1698 [31] J. Alwall, R. Frederix, S. Frixione et al., “The automated computation of tree-level
1699 and next-to-leading order differential cross sections, and their matching to parton
1700 shower simulations”, *JHEP* **07** (2014) 079, arXiv:1405.0301.
1701 doi:10.1007/JHEP07(2014)079.
- 1702 [32] T. Sjostrand, S. Mrenna, and P. Z. Skands, “PYTHIA 6.4 Physics and Manual”,
1703 *JHEP* **05** (2006) 026, arXiv:hep-ph/0603175.
1704 doi:10.1088/1126-6708/2006/05/026.
- 1705 [33] GEANT4 Collaboration, “GEANT4: A Simulation toolkit”, *Nucl. Instrum. Meth.*
1706 **A506** (2003) 250–303. doi:10.1016/S0168-9002(03)01368-8.
- 1707 [34] J. Allison et al., “Geant4 developments and applications”, *IEEE Trans. Nucl. Sci.*
1708 **53** (2006) 270. doi:10.1109/TNS.2006.869826.

- 1709 [35] R. Gavin et al., “FEWZ 3.1: A User’s Guide”.
 1710 http://www.hep.anl.gov/fpetriello/FEWZManual_3.1.pdf. Accessed:
 1711 2015-10-27.
- 1712 [36] M. Czakon, P. Fiedler, and A. Mitov, “Total Top-Quark Pair-Production Cross
 1713 Section at Hadron Colliders Through $O(\frac{4}{S})$ ”, *Phys. Rev. Lett.* **110** (2013) 252004,
 1714 [arXiv:1303.6254](https://arxiv.org/abs/1303.6254). doi:10.1103/PhysRevLett.110.252004.
- 1715 [37] B. Fuks, M. Klasen, D. R. Lamprea et al., “Gaugino production in proton-proton
 1716 collisions at a center-of-mass energy of 8 TeV”, *JHEP* **1210** (2012) 081,
 1717 [arXiv:1207.2159](https://arxiv.org/abs/1207.2159). doi:10.1007/JHEP10(2012)081.
- 1718 [38] B. Fuks, M. Klasen, D. R. Lamprea et al., “Precision predictions for electroweak
 1719 superpartner production at hadron colliders with Resummino”, *Eur.Phys.J.* **C73**
 1720 (2013) 2480, [arXiv:1304.0790](https://arxiv.org/abs/1304.0790). doi:10.1140/epjc/s10052-013-2480-0.
- 1721 [39] J. D. Brinson, “A search for disappearing tracks in proton-proton collisions at $\sqrt{s} =$
 1722 8 TeV”. PhD thesis, Ohio State U.
 1723 <https://inspirehep.net/record/1381347/files/CERN-THESIS-2015-030.pdf>.
- 1724 [40] J. Brinson, C. Hill, and W. Wulsin, “Search for disappearing tracks”, *CMS Analysis
 Note CMS-AN-12-400* (2014). Internal documentation.
- 1726 [41] CMS Collaboration, “Tracking and Primary Vertex Results in First 7 TeV
 1727 Collisions”, *CMS Physics Analysis Summary CMS-PAS-TRK-10-005* (2010).
- 1728 [42] A. Bhatti et. al., “Search for New Physics in the Monojet final state at CMS”, *CMS
 Analysis Note CMS-AN-12-421* (2012). Internal documentation.
- 1730 [43] CMS Collaboration, “Search for dark matter, extra dimensions, and unparticles in
 1731 monojet events in protonproton collisions at $\sqrt{s} = 8$ TeV”, *Eur. Phys. J.* **C75**
 1732 (2015), no. 5, 235, [arXiv:1408.3583](https://arxiv.org/abs/1408.3583). doi:10.1140/epjc/s10052-015-3451-4.
- 1733 [44] CMS Collaboration, “Studies of Tracker Material”, *CMS Physics Analysis Summary
 CMS-PAS-TRK-10-003* (2010).
- 1735 [45] CMS Collaboration, “Measurement of Higgs boson production and properties in the
 1736 WW decay channel with leptonic final states”, *JHEP* **01** (2014) 096,
 1737 [arXiv:1312.1129](https://arxiv.org/abs/1312.1129). doi:10.1007/JHEP01(2014)096.
- 1738 [46] CMS Collaboration, “Performance of Electron Reconstruction and Selection with
 1739 the CMS Detector in Proton-Proton Collisions at $s = 8$ TeV”, *JINST* **10** (2015),
 1740 no. 06, P06005, [arXiv:1502.02701](https://arxiv.org/abs/1502.02701). doi:10.1088/1748-0221/10/06/P06005.

- 1741 [47] CMS Collaboration, “Performance of CMS muon reconstruction in pp collision
1742 events at $\sqrt{s} = 7$ TeV”, *JINST* **7** (2012) P10002, [arXiv:1206.4071](https://arxiv.org/abs/1206.4071).
1743 doi:[10.1088/1748-0221/7/10/P10002](https://doi.org/10.1088/1748-0221/7/10/P10002).
- 1744 [48] CMS Collaboration, “Performance of tau-lepton reconstruction and identification in
1745 CMS”, *JINST* **7** (2012) P01001, [arXiv:1109.6034](https://arxiv.org/abs/1109.6034).
1746 doi:[10.1088/1748-0221/7/01/P01001](https://doi.org/10.1088/1748-0221/7/01/P01001).
- 1747 [49] J. Neyman *Phil. Trans. Royal Soc. London, Series A* **236** (1937) 333–80. Reprinted
1748 in *A Selection of Early Statistical Papers on J. Neyman* (University of California
1749 Press, Berkeley, 1967).
- 1750 [50] CMS Collaboration, “CMS Luminosity Based on Pixel Cluster Counting - Summer
1751 2013 Update”, *CMS Physics Analysis Summary CMS-PAS-LUM-13-001* (2013).
- 1752 [51] D. Barge et. al., “Hadronic Recoil Studies of Heavy Boosted Systems”, *CMS*
1753 *Analysis Note CMS-AN-13-059* (2013). Internal documentation.
- 1754 [52] CMS Collaboration, “Jet Energy Scale and Resolution in the CMS Experiment”,
1755 *CMS Physics Analysis Summary CMS-PAS-JME-13-004* (2015).
- 1756 [53] K. Goebel, “Probing supersymmetry based on precise jet measurements at the CMS
1757 experiment”. PhD thesis, U. Hamburg, Dept. Phys., 2015.
1758 <http://www-library.desy.de/cgi-bin/showprep.pl?thesis15-003>.
- 1759 [54] J. Pumplin, D. R. Stump, J. Huston et al., “New generation of parton distributions
1760 with uncertainties from global QCD analysis”, *JHEP* **07** (2002) 012,
1761 [arXiv:hep-ph/0201195](https://arxiv.org/abs/hep-ph/0201195). doi:[10.1088/1126-6708/2002/07/012](https://doi.org/10.1088/1126-6708/2002/07/012).
- 1762 [55] M. Botje et al., “The PDF4LHC Working Group Interim Recommendations”,
1763 [arXiv:1101.0538](https://arxiv.org/abs/1101.0538).
- 1764 [56] A. Vicini, “Practical implementation of the PDF4LHC recipe”.
1765 http://www.hep.ucl.ac.uk/pdf4lhc/PDF4LHC_practical_guide.pdf. Accessed:
1766 2015-11-27.
- 1767 [57] CMS Collaboration, “Pileup Reweighting Utilities”, *Internal CMS Wiki* (2012).
1768 <https://twiki.cern.ch/twiki/bin/viewauth/CMS/PileupMCReweightingUtilities>,
1769 Topic revision: r29.
- 1770 [58] CMS Collaboration, “Estimating Systematic Errors Due to Pileup Modeling”,
1771 *Internal CMS Wiki* (2013).
1772 <https://twiki.cern.ch/twiki/bin/view/CMS/PileupSystematicErrors>, Topic revision:
1773 r11.

- 1774 [59] L. Quertenmont at al., “Searches for Heavy Stable Charged Particles with
1775 Combined 2011 and 2012 Datasets”, *CMS Analysis Note CMS-AN-12-293* (2013).
1776 Internal documentation.
- 1777 [60] J. Ott, “Search for Resonant Top Quark Pair Production in the Muon+Jets
1778 Channel with the CMS Detector”. PhD thesis, Hamburg U., 2013.
1779 https://inspirehep.net/record/1296889/files/TS2013_046.pdf.
- 1780 [61] T. Junk, “Confidence level computation for combining searches with small
1781 statistics”, *Nucl. Instrum. Meth. A***434** (1999) 435–443, [arXiv:hep-ex/9902006](https://arxiv.org/abs/hep-ex/9902006).
1782 doi:10.1016/S0168-9002(99)00498-2.
- 1783 [62] A. L. Read, “Modified frequentist analysis of search results (The CL(s) method)”,
1784 in *Workshop on confidence limits, CERN, Geneva, Switzerland, 17-18 Jan 2000: Proceedings*. 2000. <http://cds.cern.ch/record/451614>.
- 1786 [63] A. L. Read, “Presentation of search results: The CL(s) technique”, *J. Phys. G***28**
1787 (2002) 2693–2704. [,11(2002)]. doi:10.1088/0954-3899/28/10/313.
- 1788 [64] CMS and ATLAS Collaborations, “Procedure for the LHC Higgs boson search
1789 combination in summer 2011”, *Technical Report* (2011). CMS-NOTE-2011-005,
1790 ATL-PHYS-PUB-2011-011.
- 1791 [65] CMS Collaboration, “Documentation of the RooStats-based statistics tools for
1792 Higgs PAG”, *Internal CMS Wiki* (2015).
1793 <https://twiki.cern.ch/twiki/bin/viewauth/CMS/SWGuideHiggsAnalysisCombinedLimit>,
1794 Topic rev: r124.
- 1795 [66] C. H. Chen, M. Drees, and J. F. Gunion, “Addendum/erratum for ’searching for
1796 invisible and almost invisible particles at e+ e- colliders’ [hep-ph/9512230] and ’a
1797 nonstandard string/SUSY scenario and its phenomenological implications’
1798 [hep-ph/9607421]”, [arXiv:hep-ph/9902309](https://arxiv.org/abs/hep-ph/9902309).